Commissioning of EndCap RPCs and the Study of χ_c States with CMS Detector at $\sqrt{s} = 7\ TeV$

by

Muhammad Ahmad

SUBMITTED IN PARTIAL FULFILLMENT OF THE
REQUIREMENTS FOR THE DEGREE OF
DOCTOR OF PHILOSOPHY
AT
QUAID-I-AZAM UNIVERSITY
ISLAMABAD, PAKISTAN
MAY 2014

CERTIFICATE

The undersigned hereby certify that the research work presented in this thesis titled **"Commissioning of EndCap RPCs and the Study of χ_c States with CMS Detector at $\sqrt{s}$ = 7 TeV"** by **Muhammad Ahmad** is carried out under my supervision in partial fulfillment of the requirements for the degree of **Doctor of Philosophy**.

Supervisor:

Prof. Hafeez R. Hoorani
Director Research
National Center For Physics
Quaid-i-Azam University Campus
Islamabad, Pakistan

Submitted Through:

Prof. Arshad Majid Mirza
Chairman
Department of Physics
Quaid-i-Azam University
Islamabad, Pakistan

Dedicated to Jamila, Abdullah, Omar and Azam

Abstract

Resistive plate chambers (RPC) are fast gaseous detectors that provide a dedicated muon trigger system both in the barrel and in the endcap regions of CMS. Commissioning of RPC means to ensure that all the services (e.g. HV, LV, gas, cooling, sensors for temperature & humidity and readout system) needed to operate the chambers are working properly. EndCap RPCs are assembled in Pakistan and are commissioned by Pakistani team during 2008-09.

The prompt production of χ_c quarkonia is studied in proton-proton collisions at $\sqrt{s} = 7$ TeV, using data collected by CMS in 2011 corresponding to an integrated luminosity of 4.62 fb^{-1} . The χ_c mesons are reconstructed through their radiative decays to J/ψ and photon with $J/\psi \rightarrow \mu^+\mu^-$. The photons are reconstructed through their conversion in electron-positron pairs in the tracking detector which gives a mass resolution sufficient for resolving χ_{cj} states. The ratio of the prompt production cross sections of χ_{c1} and χ_{c2} states, $\sigma(\chi_{c2})/\sigma(\chi_{c1})$ has been determined as a function of the J/ψ transverse momentum between 7 and 25 GeV/c.

Acknowledgement

I am grateful to my supervisor, Prof. Hafeez Hoorani for his great support and encouraging behavior during my PhD. I am really thankful to my professor as he arranged for me the unique opportunity to work at the world's largest particle physics laboratory, CERN. I am also very much thankful to DG CERN who funded my one year stay at CERN for doing physics analysis. Without this financial support this work would not have been possible.

I would like to thanks Stefano Argiro at CERN, who helped me a lot in learning the tools for quarkonium study at CMS. I am also grateful for his guidance. I would also like to say thanks to B-Physics group members Carlos Lourenco, Hermine Woehri, Domenico Giordano and Valentin Knunz. They have always given useful comments and helped in different places for my work. I would like to say special thanks to Ilina V. Akin, who is also involved in the same study. She has been very helpful fellow. I always appreciate her friendly and helpful attitude.

Then I would like to say thanks to my family members who have been patient to bear my hardships during my research. I would specially like to mention about my grandfather(Late) and grandmother(Late). My grandfather started to motivate people of our poor village for better education. His life is great inspiration for me. And my grandmother whom I really miss. I would also pay special thanks to my father, who has encouraged and supported us for higher studies and my mother who provided me with moral and emotional support. Then my brothers Asif and Zia who have financially supported me at different levels of my education, my sisters for their love and care and my all nephew and niece specially Marfoa and Noor.

I would also like to say thanks to my friends whom I have laughed and gone through sad moments of my life. I would like to thanks my group fellows Taimoor, Irfan bhi, Wajid, Shoaib, Saleh, Mehar, Shoaib for their fruitful discussions during this study. I also like to thank my friends DG, Jazi, Ishtiaq, Khattar, Paracha, Chandio, Mooda, Jamil, Jamal, Joya, Athar, Jam, Azam and Farooq for their nice company.

Muhammad Ahmad

Table of Contents

Abstract **iv**

Acknowledgement **v**

Table of Contents **vi**

List of Tables **ix**

List of Figures **xi**

1 Introduction **1**
1.1 Standard Model . . . 1
1.1.1 Elementary Particles . . . 1
1.1.2 Interaction of Particles and Forces . . . 3
1.1.3 Quantum Electrodynamics . . . 4
1.1.4 Quantum Chromodynamics . . . 5
1.2 Introduction to Quarkonium . . . 8
1.2.1 Quarkonium Potential . . . 9
1.2.2 Relativistic Corrections . . . 10
1.2.3 Electric Dipole Transitions . . . 11
1.3 Charmonium and Lattice QCD . . . 11
1.3.1 Charmonium versus Bottomonium . . . 12
1.4 Production of Quarkonium States . . . 13
1.4.1 Color Evaporation Model . . . 13
1.4.2 Color Singlet Model . . . 14
1.4.3 NRQCD Model . . . 15
1.4.4 k_T Factorization . . . 16
1.5 Summary of Charmonium Measurements . . . 16

2 The Compact Muon Solenoid(CMS) Experiment **19**
2.1 Large Hadron Collider(LHC) at CERN . . . 19
2.1.1 Main Goals of LHC . . . 20
2.1.2 Machine parameters . . . 21
2.1.3 Luminosity and Run 2011 . . . 21
2.2 Compact Muon Solenoid (CMS) . . . 23
2.2.1 CMS Coordinates . . . 24
2.2.2 Detector Requirement . . . 25

2.2.3 Superconducting Magnet . . . 26
2.2.4 Tracking system . . . 27
2.2.5 Electromagnetic Calorimeter (ECAL) . . . 31
2.2.6 Hadronic Calorimeter (HCAL) . . . 32
2.2.7 Muon Chambers . . . 33
2.2.8 CMS Trigger System . . . 37

3 Commissioning of Endcap RPCs 39
3.1 Resistive Plate Chambers . . . 40
3.1.1 Geometry Of Endcap RPCs . . . 41
3.1.2 Modes of Operation . . . 42
3.1.3 RPC Performance Parameters . . . 43
3.2 Commissioning of Forward RPCs . . . 44
3.2.1 High Voltage System: HV . . . 45
3.2.2 HV Distribution Box . . . 50
3.2.3 Testing . . . 51
3.2.4 Low Voltage System . . . 53
3.2.5 Threshold Scanned Connectivity Test . . . 54
3.2.6 Gas System . . . 55
3.2.7 Cooling System . . . 56
3.2.8 The Detector Control System (DCS) . . . 56
3.3 Problems and solutions from commissioning . . . 57
3.4 Efficiency of Endcap RPCs . . . 58

4 Reconstruction and Selection of χ_c Candidate 59
4.1 Introduction . . . 59
4.2 Data Samples . . . 61
4.3 Triggers for χ_c analysis . . . 61
4.4 Reconstruction of Muons . . . 62
4.4.1 Standalone Muons . . . 63
4.4.2 Tracker Muons . . . 63
4.4.3 Global Muons . . . 64
4.5 Dimuon (J/ψ) Candidates . . . 66
4.6 Converted Photon . . . 66
4.6.1 Electron Positron Pair . . . 67
4.6.2 Reconstruction of Converted Photon . . . 67
4.6.3 π^0 Rejection . . . 70
4.6.4 Conversion Radius . . . 71
4.7 χ_c Selection . . . 71
4.7.1 Extraction of Prompt Component . . . 73

5 Cross Section ratio measurement of χ_{c1} and χ_{c2} 75
5.1 Analysis Procedure . . . 75
5.1.1 Fitting Procedure . . . 77
5.1.2 Number of χ_c from data . . . 78
5.1.3 Study of Kinematic Variables from Data . . . 79

5.2 Study of Acceptance and Efficiency 84
5.2.1 MC Sample Generation 84
5.2.2 Decay Angular Distribution 86
5.2.3 Detector Simulation, Reconstruction and Selection of MC Sample 87
5.2.4 Ratio of Efficiencies of χ_{c1} and χ_{c2} 88
5.2.5 Study of Kinematic Variables from MC 88
5.2.6 Reconstruction Efficiency of J/ψ 93
5.2.7 Reconstruction Efficiency of Photons 93
5.3 Consistency Checks in the Measurement of $\varepsilon_1/\varepsilon_2$ 95
5.3.1 Reweighing Procedure 95
5.3.2 Effect of $p_T(\gamma)$ on Efficiency 96
5.3.3 Effect of π^0 Rejection 96
5.4 Systematic Uncertainties 96
5.4.1 Uncertainty from the mass fit and χ_{c1} and χ_{c2} counting . . . 97
5.4.2 Uncertainty in the ratio of efficiencies 98
5.4.3 Choice of Input $p_T(\chi_c)$ Spectrum 98
5.4.4 Pileup 100
5.4.5 χ_c Polarization 102
5.5 Results 104
5.6 Comparison with Theory 107

Conclusion **112**

Bibliography **114**

A Fits to Pythia Monte Carlo particle gun **120**

B Uncertainties from the signal model **127**

List of Tables

1.1 List of elementry particles and their properties 2
1.2 Four fundamental forces of the nature and their relative strength . . 3
1.3 Charmonium states, their quantum numbers and mass 12
1.4 Branching ratios of $c\bar{c}$ states from PDG [49] 18

2.1 Technical aspects of LHC 21
2.2 General Parameters of Superconducting Magnet 27

3.1 Dimensions of RPC installed in Ring2 and Ring3. 42
3.2 Hardware used in High Voltage System 45
3.3 Hardware used in Low Voltage System. 52
3.4 Scheme for YE+1-X4 far side. 53

4.1 Official CMS Data samples used for the analysis. 61
4.2 HLT trigger paths used in this analysis 63
4.3 Track selection criteria for Muons. 65
4.4 Muons selection cuts 65
4.5 J/ψ selection cuts 66
4.6 Track parameters for converted photons 68
4.7 Selection cuts for converted photons 70
4.8 Summary of the cuts used to select χ_c candidates 74

5.1 Values of Mass, Width and Branching fraction 77
5.2 Parameters of the double-sided crystal ball function 78
5.3 Numbers of χ_{c1} and χ_{c2} events extracted from the maximum likelihood fit, and the ratio of the two values. Uncertainties are statistical only 83
5.4 Ratio of efficiencies $\varepsilon_1/\varepsilon_2$ measured with $PYTHIA$ particle gun. Errors are statistical only. 89
5.5 The values of $N_{\chi_{c2}}$ / $N_{\chi_{c1}}$ without π^0 rejection 97
5.6 The values of $\varepsilon_1/\varepsilon_2$ without π^0 rejection 97
5.7 Relative systematic uncertainties on R_p for different ranges of J/ψ transverse momentum from different sources and the total uncertainty 99
5.8 The values of $\varepsilon_1/\varepsilon_2$ for different choices of input $p_T(\chi_c)$spectrum . . 99

5.9 Pileup 102
5.10 The efficiency ratio $\varepsilon_1/\varepsilon_2$ for different polarization scenarios in which the χ_{c1} is either unpolarized or has helicity $m_{\chi_c 1} = 0, \pm 1$ and the $m_{\chi_c 2}$ is either unpolarized or has helicity $m_{\chi_c 1} = 0, \pm 2$ in the helicity frame, relative to the unpolarized case 104
5.11 The values of $\varepsilon_1/\varepsilon_2$ for different polarization scenarios in the Collins-Soper frame, relative to the unpolarized case 106
5.12 The results of our measurement of $\frac{\mathscr{B}(\chi_{c2})\sigma(\chi_{c2})}{\mathscr{B}(\chi_{c1})\sigma(\chi_{c1})}$ for the various values of $p_T^{J/\psi}$. The first error is statistical, the second is systematic. Two separate columns report the uncertainty deriving from the extreme polarization scenarios in the *Collins-Soper frame*, and the *Helicity frame* 110
5.13 The results of our measurement of $\frac{\sigma(\chi_{c2})}{\sigma(\chi_{c1})}$ for the various values of $p_T^{J/\psi}$. The first error is statistical, the second is systematic. Two separate columns report the uncertainty derived from the extreme polarization scenarios in the *Collins-Soper frame*, and the *Helicity frame* 111
5.14 Measurements of $\mathscr{B}(\chi_{c2})\sigma(\chi_{c2})/\mathscr{B}(\chi_{c1})\sigma(\chi_{c1})$ for the given $p_T(J/\psi)$ ranges after extrapolating the measurement to the kinematic region $p_T(\gamma) > 0$ and assuming unpolarized χ_c production. The first uncertainty is statistical and the second is systematic. The last column reports the largest variations due changes in the assumed χ_c polarizations 111

B.1 Ratio of $N_{\chi_{c2}}/N_{\chi_{c1}}$ for different signal parameters varied within their uncertainties.. 128

List of Figures

1.1 Energy spectrum of Charmonium states 10
1.2 Result of CDF 17
1.3 Result of LHCb measurement of cross section ratio of χ_{c2} and χ_{c1} . 18

2.1 Layout diagram of Large Hadron Collider at CERN (LHC) 22
2.2 Integrated luminosity plot for 2011 data, delivered by LHC and collected by CMS [32]. 23
2.3 The schematic diagram of Compact Muon Solenoid (CMS) at LHC 24
2.4 A cross sectional view of CMS Detector showing layers of sub-detectors and path of detectable particles 25
2.5 Superconducting solenoidal magnet of CMS 26
2.6 CMS pixel and silicon tracker: Different geometrical layers 27
2.7 CMS tracker: cross sectional view 29
2.8 The material budget in units of radiation length as a function of pseudorapidity for different sub detectors (left) and functional contributions (right) [20] 31
2.9 Layout of electromagnetic calorimeter (ECAL) of CMS 33
2.10 Schematic layout of Hadronic calorimeter (HCAL) of CMS 34
2.11 Geometrical layout of Muon chambers of CMS, showing RPCs , CSCs and DTs 35
2.12 A unit cell of drift tube chamber 36
2.13 Level-1 Trigger structure of CMS 38

3.1 A complete Disk of endcap RPCs of CMS. RPC are installed in Ring2 and Ring3 where Ring1 is empty. 40
3.2 View of a quadrant of CMS in rz-plane where MB and ME are the barrel and endcap Muon system layout. 41
3.3 Geometry of a Resistive Plate Chamber where, R_0 is radius from beam line (low eta), and R_i is the radius from beam line (high eta). 42
3.4 Block diagram of HV system 46
3.5 (Top) Main Frame Power Supply, (Bottom) Easy Crate 47
3.6 High Voltage patch pannel for endcap RPCs. 48
3.7 Patch panel at the edge of chamber. 48
3.8 Pair of chambers connected to one channel of HV modules. 49

3.9 HV distribution box 50
3.10 HV distribution box test results 51
3.11 Efficiency plot for Endcap RPCs for period 2010 and 2011 58

4.1 Di-muon mass distribution obtained from overlapping several trigger paths 62
4.2 Invariant Mass of $\mu^+\mu^-$ 67
4.3 Positive and a negative distance of minimum approach d_m between two ideal track circles 69
4.4 Left: invariant mass distribution for pairs of converted photons. Right: invariant mass distribution of a converted photon with a calorimetric (Particle Flow) photon. 70
4.5 x-y distribution in the pixel detector region (above) Conversion Radius (below) 72
4.6 Pseudo-proper decay length for separation of prompt and non-prompt component of J/ψ 74

5.1 The distribution of the variable Q = $m_{\mu\mu\gamma}$ - $m_{\mu\mu}$ + $m_{J/\psi}$ for χ_c candidates with $p_T(J/\psi)$ in [7.0 - 9.0] GeV/c (top) and in [9.0 - 11.0] GeV/c (bottom) 80
5.2 The distribution of the variable Q = $m_{\mu\mu\gamma}$ - $m_{\mu\mu}$ + $m_{J/\psi}$ for χ_c candidates with $p_T(J/\psi)$ in [11.0 - 13.0] GeV/c (top) and in [13.0 - 16.0] GeV/c (bottom) 81
5.3 The distribution of the variable Q = $m_{\mu\mu\gamma}$ - $m_{\mu\mu}$ + $m_{J/\psi}$ for χ_c candidates with $p_T(J/\psi)$ in [16.0 - 20.0] GeV/c (top) and in [20.0 - 25.0] GeV/c (bottom) 82
5.4 Kinematic distribution from data for p_T of χ_c (top) and rapidity of χ_c (bottom) 83
5.5 Kinematic distribution from data for p_T of J/ψ (top) and rapidity of J/ψ (bottom) 84
5.6 Kinematic distribution from data for p_T of γ (top) and pseudorapidity of γ (bottom) 84
5.7 The measured p_T spectrum of ψ'. The red line is fitted with Equation 5.10 used as input distributeion for the PYTHIA particle gun . 86
5.8 Production of χ_c in pp collisions and its decay to $J/\psi + \gamma$. 87
5.9 p_T distribution of generated (left) and reconstructed (right) χ_c MC events. 89
5.10 p_T distribution of generated (left) and reconstructed (right) γ MC events. 90
5.11 p_T distribution of generated (left) and reconstructed (right) J/ψ MC events. 90

5.12 $p_T(J/\psi)$ vs $p_T(\chi_c)$ with mean distributions superimposed for χ_{c1} (top) and χ_{c2} (bottom) generated with Pythia Monte Carlo particle gun with flat p_T input spectrum for χ_c. The slopes of the mean distributions are 0.875 and 0.879 respectively 91
5.13 $p_T(\gamma)$ vs $p_T(J/\psi)$ with mean distributions superimposed for χ_{c1} (top) and χ_{c2} (bottom) generated with Pythia MC particle gun with flat p_T input spectrum for χ_c. The slopes of the mean distributions are 0.128 and 0.142 respectively. 92
5.14 Ratio of reconstruction efficiencies for J/ψ coming from χ_{c1} and χ_{c2} 93
5.15 Kinematic distribution from data for p_T of γ (top) and pseudorapidity of γ (bottom) 95
5.16 pileup 101
5.17 Ratio of the χ_{c2} to χ_{c1} production cross sections (circles) and ratio of the cross sections times the branching fractions to J/ψ γ (squares) as a function of the J/ψ transverse momentum with the hypothesis of unpolarized production. The error bars correspond to the statistical uncertainties and the green band corresponds to the systematic uncertainties. For the cross section ratios, the 5.6% uncertainty from the branching fractions is not included. 105
5.18 Comparison of the measured $\mathscr{B}(\chi_{c2})\sigma(\chi_{c2})/\mathscr{B}(\chi_{c1})\sigma(\chi_{c1})$ values with theoretical predictions from the k_T-factorization calculations (solid red lines). The error bars and bands show the experimental statistical and systematic uncertainties, respectively. The measurements use an acceptance correction assuming zero helicity for the χ_c , as predicted by the k_T-factorization model 108
5.19 Comparison of the measured $\mathscr{B}(\chi_{c2})\sigma(\chi_{c2})/\mathscr{B}(\chi_{c1})\sigma(\chi_{c1})$ values with theoretical predictions from the NRQCD calculations (solid red lines). The measurements are corrected to match the kinematic range used in the NRQCD calculation and assume the χ_c are produced unpolarized. The measurements assuming two different extreme polarization scenarios are shown by the long-dashed and short-dashed lines in the plot. The 1-standard-deviation uncertainties in the NRQCD prediction, originating from uncertainties in the color-octet matrix elements, are displayed as the dotted lines 109

A.1 Double-sided Crystal Ball fits to particle gun Monte Carlo for χ_{c1} candidates for $p_T(J/\psi)$ in [7.0-9.0] GeV/c (top) and [9.0-11.0] GeV/c (bottom). 121
A.2 Double-sided Crystal Ball fits to particle gun Monte Carlo for χ_{c1} candidates for $p_T(J/\psi)$ in [11.0-13.0] GeV/c (top) and [13.0-16.0] GeV/c (bottom). 122

A.3 Double-sided Crystal Ball fits to particle gun Monte Carlo for χ_{c1} candidates for $p_T(J/\psi)$ in [16.0-20.0] GeV/c (top) and [20.0-25.0] GeV/c (bottom). 123
A.4 Double-sided Crystal Ball fits to particle gun Monte Carlo for χ_{c2} candidates for $p_T(J/\psi)$ in [7.0-9.0] GeV/c (top) and [9.0-11.0] GeV/c (bottom). 124
A.5 Double-sided Crystal Ball fits to particle gun Monte Carlo for χ_{c2} candidates for $p_T(J/\psi)$ in [11.0-13.0] GeV/c (top) and [13.0-16.0] GeV/c (bottom). 125
A.6 Double-sided Crystal Ball fits to particle gun Monte Carlo for χ_{c2} candidates for $p_T(J/\psi)$ in [16.0-20.0] GeV/c (top) and [20.0-25.0] GeV/c (bottom). 126

Chapter 1

Introduction

1.1 Standard Model

The universe around us is full of diverse physical and non-physical objects both seen and unseen by naked eye. Man is curious animal and he has been asking questions and seeking answers throughout the course of history starting from Aristotle and Socrates; are all the bewildering variety of objects seen in nature, made up of some elementary particles? If so how many elementary particles there are and how do they coalesce to form all the physical objects seen around us. Particle Physics is a basic science that deals with answering these questions that mankind has been asking for at least the last 5000 years. It is only in the last four decades that we have seen a reasonable progress towards understanding ourselves and the world around us. Information of basic particles and their interactions has been combined in the form of the Standard Model of Particle physics. Elementary particles are classified into two major groups by their spin, the fermions with spin 1/2 and the bosons with spin 1.

1.1.1 Elementary Particles

Fermions

The fermions are the fundamental particles with half-integral spin and they obey the Pauli Exclusion Principle. There are two types of elementary fermions: quarks and leptons (see Table 1.1).

Leptons: Leptons are fundamental particles with half-integral spin that does not feel the strong nuclear force. There are three known types or flavors of leptons: the electron, the muon, and the tau. Each flavor is represented by a pair of particles called a weak doublet, one of which is a massive charged particle (like the electron) and the other is a nearly massless neutral particle called neutrino (such as the electron neutrino). Neutrinos feel only weak force. The charged leptons have two possible spin states, while only one helicity is observed for the neutrinos (all neutrinos are left-handed, and all antineutrinos are right-handed).

Quarks: Quarks are elementary particles with half-integral spin but they are the

FERMIONS					
Leptons spin (1/2)			Quarks spin (1/2)		
Falvor	Mass GeV/c^2	Charge	Flavor	Mass GeV/c^2	Charge
Electron neutrino (ν_e)	(0-0.13)$\times 10^{-9}$	0	down (d)	0.002	-1/3
Electron (e)	0.000511	-1	up (u)	0.005	2/3
Muon neutrino (ν_μ)	(0.009-0.13)$\times 10^{-9}$	0	strange (s)	0.1	-1/3
Muon (μ)	0.106	-1	charm (c)	1.3	2/3
Tau neutrino (ν_τ)	(0.04-0.14)$\times 10^{-9}$	0	bottom (b)	4.2	-1/3
Tau (τ)	1.777	-1	top (t)	173	2/3

Table 1.1: List of elementry particles and their properties

only one that interact through all four of the fundamental forces. Quarks come in six types or flavors and are named down (d), up (u), strange (s), charm (c), bottom (b) and top (t). Antiparticles of quarks are called antiquarks. Quarks are not found as independent entities in nature. They are always found as combination of quark antiquark ($q\bar{q}$) pair states called mesons or groups of three quarks (qqq) called baryons. These combinations of quarks either a meson or baryon is called a hadron. Three same flavored quarks with half-integral spin in a baryon lead to a contradiction with the Pauli Exclusion Principle and the Fermi-Dirac statistics for systems composed of identical fermions. The Pauli Exclusion Principle states

that in the baryon (qqq) state, the three valence quarks can only be formed in the antisymmetric final state. To satisfy this requirement physicist came up with the idea of an internal quantum number called "color". The color of each quark in a baryon is such that it makes the combination qqq an antisymmetric state. There are three different types of color named after three basic colors red (r), blue (b) and green (g). The mesons and baryons are color neutral or color singlet.

Force Carriers

They are also called Mediator Particles. Fermions interact with each other with mediator particles. The mediators are spin 1 vector bosons. These are photon, gluon, W^+, W^- and Z^0 boson. The photon (γ) is responsible for electromagnetic interaction, W^+, W^- and Z^0 bosons take part in weak interaction and gluons (g) are responsible for strong interaction. The photon and gluon are massless and charge-less particles however the mass of W^+, W^- is 80.39 GeV/c^2 and Z^0 has a mass of 91.188 GeV/c^2 as shown in the Table 1.2.

Force	Gauge Boson	Mass	Charge	Range(m)	Relative Strength
Strong	8 gluons	0	0	10^{-15}	10^{38}
Electromagnetic	Photon	0	0	infinite	10^{36}
Weak	W, Z bosons	80, 91GeV	$\pm 1, 0$	10^{-18}	10^{25}
Gravitational	Graviton	0	0	infinite	1

Table 1.2: Four fundamental forces of the nature and their relative strength

1.1.2 Interaction of Particles and Forces

There are four fundamental forces as shown in Table 1.2. Except gravity all forces can be described in Standard model. These forces are responsible for interaction between particles. Mathematical description of these forces involve gauge theories [1].

Gauge Theories: Particles and their interactions are described by gauge theories, a special class of quantum theories which are invariant under Lorentz transformation. The invariance principle implies the existence of interactions that are mediated by gauge bosons. Gauge theories involve two kinds of particles, ones

that carry charge and others that mediate interaction called gauge bosons. The particles that carry charge are the fundamental fermions and non-abelian gauge boson, whereas the particles mediating interactions consists solely of gauge bosons, both abelian and non-abelian. The abelian gauge bosons do not interact with each other while the non-abelian gauge bosons interact with each other.

To date, three of the observed forces of nature have been successfully described in terms of gauge symmetries. According to Noether's theorem there is an invariant observable for each symmetry of the system as translational symmetry means that momentum of system is conserved. The forces can be described in terms of unitary groups of different dimensions. Physicist describe combinations of gauge groups as $\mathrm{SU}(3)_C \times SU(2)_L \times U(1)_Y$. There are ($\mathrm{N}^2$- 1) gauge bosons in the gauge theory described by the groups SU(N). The group $\mathrm{SU}(3)_C$ describes strong interaction known as quantum-chromodynamics (QCD). The gauge field of this theory is gluon which is massless. The group $\mathrm{SU}(3)_C$ has 8 generators as predicted by the theory. The group SU(2) describes the weak interactions. It has three generators which correspond to W^+, W^- and Z_0. This theory describes the interaction of only left handed particles. For left handed particle the spin and momentum are anti-parallel.

1.1.3 Quantum Electrodynamics

The theory describing the electrodynamic interaction is quantum electrodynamics (QED). It is constructed by applying the principle of local gauge invariance to the free Dirac Lagrangian. The corresponding operator U=e ^{iH} belongs to abelian group $\mathrm{U}(1)_Y$, where the gauge H is just a real number. To construct the locally invariant Lagrangian, it is necessary to introduce a vector field, A_μ which contains the gauge freedom necessary to absorb changes in the Lagrangian produced by the local gauge transformation. The desired symmetry is achieved only if the vector field is considered to be long-ranged and massless. The resulting QED interaction Lagrangian can be written as:

$$L_{QED} = (e\overline{\psi}\gamma^\mu\psi)A_\mu \tag{1.1}$$

where e is the electric charge , γ are the Dirac matrices related to the spin of fermions and the quantity in parentheses represents the fermion current. The resulting field equations are precisely those predicted by classical electrodynamics. Here, the fermions are quanta of the Dirac fields $\overline{\psi}$, and photons are quanta of electrodynamic field A_μ.

1.1.4 Quantum Chromodynamics

Quantum Chromodynamics is based on the gauge group SU(3), the Special Unitary group in 3(complex) dimensions. In the context of QCD, we represent this group as a set of unitary 3×3 matrices with determinant one. This is called the adjoint representation and can be used to represent gluons in color space. Since there are 9 linearly independent unitary complex matrices, one of which has determinant 1, there are a total of 8 independent directions in the adjoint color space, i.e., the gluons are octets. In QCD, these matrices can operate both on each other (gluon self interactions) and on a set of complex 3-vectors (the fundamental representation), the latter of which represent quarks in color space. The fundamental representation has one linearly independent basis vector per degree of SU(3), and hence the quarks are triplets. The Lagrangian of QCD is:

$$\mathscr{L}_{QCD} = \bar{\psi}_q^i \left(i(\gamma^\mu)(D_\mu)_{ij} - m_q \psi_q^j - m_q \bar{\psi}_q^i \psi_{qi} - \frac{1}{4} F_{\mu\nu}^a F^{a\mu\nu} \right) \tag{1.2}$$

where ψ_q^i denotes a quark field with color index i, $\psi_q = (\psi_{qR}, \psi_{qG}, \psi_{qB})^T, \gamma^\mu$ is a Dirac matrix that expresses the vector nature of the strong interaction, with μ being a Lorentz vector index, m_q allows for the possibility of non-zero quark masses (induced by the standard Higgs mechanism or similar), $F_{\mu\nu}^a$ is the gluon field strength tensor for a gluon with color index a (in the adjoint representation, i.e., a $\in$ [1,...., 8]), and D_μ is the covariant derivative in QCD,

$$((D_\mu)_{ij}) = \delta_{ij}\partial_\mu - i g_s t_{ij}^a A_\mu^a \tag{1.3}$$

with g_s the strong coupling (related to α_s by $g_s^2 = 4\pi s$), A_μ^a the gluon field with (adjoint-representation) color index a, and t_{ij}^a proportional to the hermitian and

traceless Gell-Mann matrices of SU(3),

$$\lambda^1 = \begin{pmatrix} 0 & 1 & 0 \\ 1 & 0 & 0 \\ 0 & 0 & 0 \end{pmatrix}, \lambda^2 = \begin{pmatrix} 0 & i & 0 \\ i & 0 & 0 \\ 0 & 0 & 0 \end{pmatrix}, \lambda^3 = \begin{pmatrix} 1 & 0 & 0 \\ 0 & -1 & 0 \\ 0 & 0 & 0 \end{pmatrix}, \lambda^4 = \begin{pmatrix} 0 & 0 & 1 \\ 0 & 0 & 0 \\ 1 & 0 & 0 \end{pmatrix} \tag{1.4}$$

$$\lambda^5 = \begin{pmatrix} 0 & 0 & i \\ 0 & 0 & 0 \\ i & 0 & 0 \end{pmatrix}, \lambda^6 = \begin{pmatrix} 0 & 0 & 0 \\ 0 & 0 & 1 \\ 0 & 1 & 0 \end{pmatrix}, \lambda^7 = \begin{pmatrix} 0 & 0 & 0 \\ 0 & 0 & -i \\ 0 & i & 0 \end{pmatrix}, \lambda^8 = \begin{pmatrix} \frac{1}{\sqrt{3}} & 1 & 0 \\ 0 & \frac{1}{\sqrt{3}} & 0 \\ 0 & 0 & \frac{2}{\sqrt{3}} \end{pmatrix} \tag{1.5}$$

These generators are just the SU(3) analogs of the Pauli matrices in SU(2). By convention, the constant of proportionality is normally taken to be

$$t^a_{ij} = \frac{1}{2}\lambda^a_{ij} \tag{1.6}$$

This choice in turn determines the normalization of the coupling g_s, via equation 1.3, and fixes the values of the SU(3) Casimirs and structure constants.

$$G^a_{\mu\nu} = \partial_\mu G^a_\nu - \partial_\nu G^a_\mu - g f^{abc} G^b_\mu G^c_\nu \tag{1.7}$$

where f^{abc} are the structure constants of SU(3).

An important theoretical notion concerning the final term of the above Lagrangian is the Wilson loop variable. This loop variable plays a most-important role in discretized forms of the QCD (known as lattice QCD), and more generally, it distinguishes confined and de-confined states of a gauge theory. QCD enjoys two peculiar properties i.e Confinement and Asymptotic freedom

Confinement: The force between quarks does not reduce as they are separated. Because of this, it would take an infinite amount of energy to separate two quarks; they are forever bound into hadrons such as the proton and the neutron. Although analytically unproven, confinement is widely believed to be true because it explains the consistent failure of free quark searches, and it is easy to demonstrate in lattice QCD.

At large distance the gluon self-coupling shows effects in the $Q\bar{Q}$ interaction. As quarks are pulled apart and the distance between the quarks (let's denote it by "r") increases the attractive force between the quarks increases as well. The force between the quarks forms imaginative field lines like an electric dipole. The

number of field lines depends on the quark colors. At large distances these lines starts to compress into a tube known as "color flux tube". Inter-quark distance increases, as the cross-sectional area of the tube does not change and the number of field lines stay constant. Hence the energy of the system will increase with internal distance of quarks. The energy per unit distance or the field strength in the tube also stays constant. The potential in the tube can be found using Gauss' Law, $\nabla^2 V = 0$ resulting $V(r) = \kappa r$ where κ is a constant. The $Q\bar{Q}$ potential arises from many gluons (or the color flux tube) or an effective scalar exchange as opposed to the Coulombic interaction which is due to exchange of a vector particle.

When the "tube" stretches out, it is less favorable to separate the original pair than to create a new $Q\bar{Q}$ from the vacuum to form two mesons. The fact that individual free quarks cannot be observed is known as "color confinement". A hadron system is formed from a lot of energy transferred from a quark pair or gluon to many quarks moving away from each other. This hadron system is called a hadron jet. In a jet, the quarks become light hadrons by fragmentation. This process continues until all the energy has dissipated.

Asymptotic freedom: At higher energies, the quarks and gluons interact very weakly. This prediction of QCD was first discovered in the early 1970s by David Politzer, Frank Wilczek and David Gross. At very small distances (or higher energies) the quarks behave like free particle. This is known as *asymptotic freedom*. In contrast, the QED behavior is different at higher energies. The QED coupling constant has numerical value of 1/137. This is derived from the electron charge at a large distance. The electron can emit and reabsorb virtual photons creating e^+e^- pairs. These pairs polarize in the direction of the field of the charge. Due to these pairs a shielding effect is produced. When the distance to the charge is reduced, this effect is reduced until there is no energy because of pairs coming from virtual photons. This behavior can be described by a running coupling constant i.e an α_{em} which depends on the momentum transferred q^2. The coupling strength increases with increasing q^2. In QCD the quark pairs are produced in a similar way shielding the "bare quark". But the gluons can also make a gluon

pair as the filed is non-Abelian. This gluon self-coupling effectively gives an *anti*-shielding effect as it "spreads out" the color charge. Thus the quark color increases with q^2. The QCD running coupling constant, $\alpha_s(q^2)$, has the form, $\alpha_s(q^2) = \alpha_s(q_0^2)/(1+B\alpha_s(q_0^2)\ln(q^2/q_0^2))$ where $B = (33-2f)/12\pi$, f is the number of quark flavors and q_0 is of order 100MeV. For $f \leqq 16$, $\alpha_s(q^2)$ decreases with increasing q^2. At asymptotically large q^2, (or small r), $\alpha_s(q^2) \to 0$ which means the quarks behave as free particles.

1.2 Introduction to Quarkonium

Quarkonium is bound state of a heavy quark and anti-quark $Q\bar{Q}$. The system behaves very similar to positronium. The state J/ψ was discovered in 1974 [2] and it was interpreted within QCD as charm-anticharm bound state. Later excited charmonium states, χ_{c0}, χ_{c1}, χ_{c2} and $\psi(2S)$ were discovered. Masses of all these states could be described by a model where they were assumed to be $c\bar{c}$ bound states. Their interaction was modeled by a non-relativistic potential. A heavier version of hadrons family was discovered in 1977, called bottomonium system [3]. This family was suggested to be bound states of 5th quark, termed as bottom or beauty (b). The potential which described charmonium also predicted masses of $b\bar{b}$ states. This implied that the strong interactions did not depend on the flavor of quarks. The light quarks have masses very close together. The flavor independence and almost same masses of the light quarks (u,d,s) were used to develop model based on SU(3)-flavor symmetry. Light hadrons are highly relativistic systems as they are combination of many different quarks in bound state while charmonium are assumed to be pure $c\bar{c}$ (similarly bottomonium as pure $b\bar{b}$) states and non-relativistic. So for strong interaction, the heavy quarkonia give better testing grounds due to their non-relativistic nature. The bound state ($t\bar{t}$) of 6th quark top (denoted by t and discovered in 1995) does not exist. The top quark decays weakly before it can interact strongly with itself or other quarks.

The study of quarkonium has received much attention from both a theoretical and an experimental point of view. The interest for these particles is twofold: on one side the availability of an overwhelming quantity of data on production

and decay rates measured in several different conditions, on the other side, the possibility of using the quarkonium system as a unique test ground for proving both the perturbative and non-perturbative aspects of the Quantum Chromodynamics (QCD).

1.2.1 Quarkonium Potential

In the quark model all mesons are bound states of two-quarks, $q_1\bar{q}_2$. These bound states can be studied similar to the hydrogen atom and positronium. Light quarks (u, d, s) states behave relativistically, so we can not apply Schrodinger equation to study them. Heavy-quarks can be studied based on non-relativistic assumptions. Interaction energy (E) of quarkonium system is substantial fraction of the total that we are disposed to regard the various energy levels as representing different particles, with the given masses:

$$M = m_1 + m_2 + E/c^2 \tag{1.8}$$

In the hydrogen atom the only considerable force is electromagnetic, but for the case of quarkonium the quarks are bound by the strong force. It is a challenge to find a potential that can describe quarks behavior. Quarks behave free at short distances but they show confinement at large distances. This is exhibited by two different terms for quarkonium potential; one for short distance and other for large distance. The short-distance behavior is dominated by one-gluon exchange in QCD, just as it is dominated by one-photon in QED. Since the gluon and photon are both massless spin-1 particles, the interactions are, on this approximation, identical. At short range, therefore, we expect a Coulomb-like potential, V $\sim$ $\frac{1}{r}$, and a fine structure that is qualitatively similar to that of positronium. On the other hand, at large distances we have to account for quark confinement: the potential must increase without limit. The precise functional form of V(r) at large r is rather speculative; some authors favor a harmonic oscillator potential, V $\sim$ r^2, others a logarithmic dependence, V $\sim \ln r$, still others a linear potential, V $\sim$ r, corresponding to a constant force. The fact is , any of these can match the data reasonably well, because they do not differ substantially over the rather narrow range of distances for which we have the sensitive probes [1].

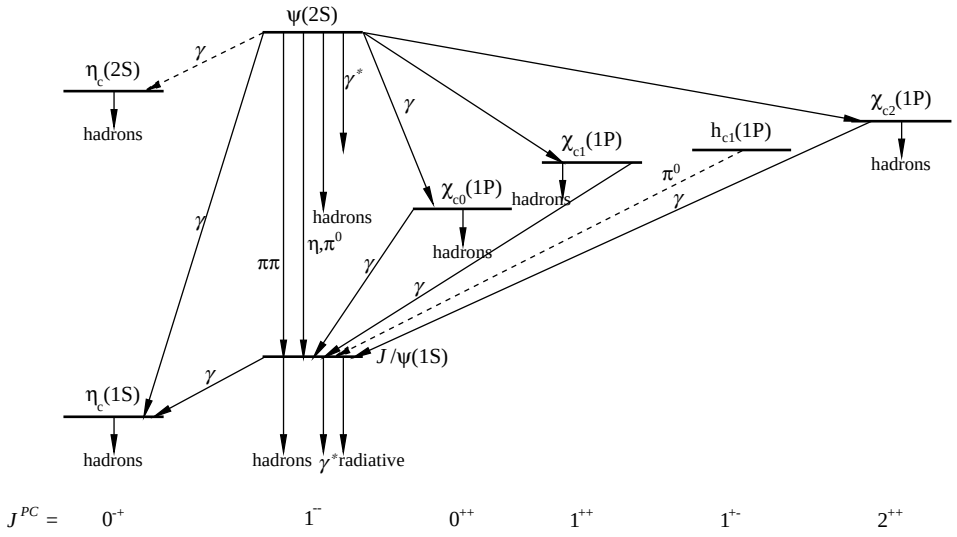

Figure 1.1: Energy spectrum of Charmonium states

The potential model is expressed in the form:

$$V(r) = -\frac{4}{3}\frac{\alpha_s(r)}{r} + \kappa r, \tag{1.9}$$

which means at large r interaction gives linear confinement; where κ is a force constant with a value in the range 0.14-0.18 GeV^2, $\alpha_s(r)$ is the QCD running coupling constant and $\frac{4}{3}$ is the appropriate color factor. At small r interaction is Coulombic . The parameters of equation can be determined experimentally. The charmonium spectrum is shown in Figure 1.1.

1.2.2 Relativistic Corrections

As for a positronium system or the hydrogen atom, relativistic effects for a $Q\bar{Q}$ system can be obtained by spin-spin, spin-orbit and tensor interactions as well as spin-independent corrections. Due to two components of strong potential, the Coulomb part (short range) and the string tension (long range) part, the interactions have different form than those for the positronium or hydrogen atom. The additional energy splittings, due to the relativistic corrections in atomic physics are of order α^2 times the original spin-independent energy level splittings, with $\alpha = 1/137$.

1.2.3 Electric Dipole Transitions

Provided that strong potential is known we can calculate the electric dipole (E1) transition rates for the bound states of heavy quarks following the techniques developed for atomic transitions. To the first order in e, the interaction Hamiltonian is $H_I = -(e_Q/\mu_c)\vec{A}\cdot\vec{p}$, where e_Q is electric charge of the quark , μ denotes the reduced mass of $Q\bar{Q}$, $\vec{A}$ is the electromagnetic vector potential and $\vec{p}$ is the momentum operator. The leading term in the multipole expansion of $\vec{A}$ is the electric dipole contribution. Using Fermi's Golden rule for transitions leads to:

$$\Gamma_{E1} = \frac{4}{3}\alpha e_Q^2 C_{fi}\delta_{S_i S_f} E_\gamma^3 |\langle n_f L_f|r|n_i L_i\rangle|^2, \tag{1.10}$$

where

- $$C_{fi} = max(L_i, L_f)(2J_f+1)\left\{ \begin{array}{ccc} L_f & J_f & S \\ J_i & L_i & 1 \end{array} \right\}^2,$$
- α is the coupling of electromagnetic force
- e_Q is the quark charge, $+2e/3$ for up type quarks and $-1e/3$ for down type quarks
- E_γ is energy of the photon
- J_f is the total angular momentum of the final $c\bar{c}$ (or $b\bar{b}$) state and $|\langle n_f L_f|r|n_i L_i\rangle|$ is the dipole matrix element which depends on the model. This matrix element is independent of J_i or J_f in the non-relativistic approximation.

1.3 Charmonium and Lattice QCD

Charmonium is special case of quarkonium when the quarks are charm quarks. In quark model, the charmonium system can be characterized by its total spin, $\mathbf{S} = \mathbf{S}_1 + \mathbf{S}_2$ (s = 0 or s = 1), the relative orbital angular momentum, L, and the total spin, $\mathbf{J} = \mathbf{L}+\mathbf{S}$. Following spectroscopic notation, charmonium bound states can be represented by notation, $n^{2s+1}L_J$, where n denotes the energy of orbit and L denotes relative angular momentum of quarks (L = 0 is labeled by the letter S,

L = 1 by P, L = 2 by D, etc). For a fermion-antifermion pair (such as $c\bar{c}$), the parity operator (P) and the charge conjugation operator (C) has eigenvalues as [4]: $P = (-1)^{L+1}$, $C = (-1)^{L+S}$. The states with long life times ($\Gamma < 20$ MeV) are summarized in Table 1.3. These states belong to lowest angular momentum L=0 and L=1 and lower mass range.

Lattice QCD is a non-perturbative tool for calculating the matrix elements of any operator and the hadronic spectrum within these hadronic states. It assumes that $Q\bar{Q}$ lives on a discrete lattice rather than in a continous space. It can also predict the dependence of α_s and the quark masses. These predictions can then be used to constrain phenomenological models and effective theories.

Meson Name	$n^{2S+1}L_J$	$I^G J^{PC}$	Mass (MeV)
η_c	1^1S_0	$0^+(J^{-+})$	2980.4 ± 1.2
J/ψ	1^3S_1	$0^-(J^{--})$	3096.916 ± 0.011
$\chi_{c0}(1P)$	1^3S_0	$0^+(J^{++})$	3414.76 ± 0.35
$\chi_{c1}(1P)$	1^3S_1	$0^+(J^{++})$	3510.66 ± 0.07
$\chi_{c2}(1P)$	1^3S_2	$0^+(J^{++})$	3556.20 ± 0.09
$\psi(2S)$	2^3S_1	$0^-(J^{--})$	3686.093 ± 0.034

Table 1.3: Charmonium states, their quantum numbers and mass

1.3.1 Charmonium versus Bottomonium

The strong force does not depend on flavor of quarks. This is obvious from the $c\bar{c}$ and $b\bar{b}$ mass spectra which has similar states for both systems. But there are important differences in $c\bar{c}$ and $b\bar{b}$ systems which are given below.

- For $b\bar{b}$ system $(v/c)^2 \approx 0.08$ which means it is nearly non-relativistic, while for $c\bar{c}$ system $(v/c)^2 \approx 0.24$ (where v = quark velocity and c = the speed of light). So a non-relativistic approximation should give better results for the $b\bar{b}$ system than for the $c\bar{c}$ system.

- The bound states of the $b\bar{b}$ have a smaller mean radius than that of $c\bar{c}$ as quarks are more deeply bound in the inter-quark potential for heavier quarks.

- The number of narrow ^3S states below the flavor threshold increases. This means more observable transitions between bound $b\bar{b}$ states than in the $c\bar{c}$

spectrum. The $c\bar{c}$ has only 2 of the $\psi(^3S)$ states below the flavor threshold.

1.4 Production of Quarkonium States

In high energy physics the production of heavy quarkonium states works as an important tool for the understanding of perturbative and non-perturbative QCD dynamics. There are different models for quarkonium production. Their details are given in the following sections.

1.4.1 Color Evaporation Model

This Color-Evaporation Model (CEM) was first time introduced in 1977 [5, 6]. It was revisited in 1996 by Halzen and Amundsonet al [7, 8]. In contrast to Color singlet Model (CSM), the heavy-quark pair produced by the perturbative interaction is not assumed to be in a color-singlet state. The assumption made in this model is that the color and the spin of the asymptotic $Q\bar{Q}$ state is randomized due to many soft interactions after it is produced. As a result the quantum numbers of this state can be different from the one which was produced initially or the two states are not correlated. CEM does not give any information of the quarkonium state polarization.

As a consequence, the production of a $^3S_1$ state by one gluon is possible. In the CSM it was not allowed due to color conservation. Cross section for charmonium directly depends on the rate of production of $c\bar{c}$ pair integrated over the mass range m_c to $2m_D$. If $2m_D$ is $D\bar{D}$ threshold and m_c is mass of charm quark then the total cross section to produce a charmonium is:

$$\sigma_{charmonium} = \frac{1}{9}\int_{2m_D}^{2m_c} dm \frac{d\sigma_{Q\bar{Q}}}{dm} \tag{1.11}$$

where $\frac{1}{9}$ is the statistical probability for the production of a color singlet state. The procedure to get the cross section for a definite charmonium state A can be obtain by the expression:

$$\sigma_A = \rho_A \sigma_{charmonium} \tag{1.12}$$

where ρ_A is constant and related to the decay width of the charmonium state. Considering production ratios for charmonium states within the simplest approach

for spin, we have $\sigma[\chi_{c0}] : \sigma[\chi_{c1}] : \sigma[\chi_{c2}] = 1 : 3 : 5$, deviations from the predicted ratio for χ_{c1} and χ_{c2} have been observed. CEM is unable to describe the variation of the production ratios for charmonium states, which is observed in experiments, as for CEM these numbers are strictly constant [9].

Despite simplicity of CEM and its phenomenological reasonable grounds, It is less reliable than the CSM. It is also important to mention that the invocation of re-interactions after the $Q\bar{Q}$ pair production contradicts factorization, which is required when the PDF are used.

1.4.2 Color Singlet Model

The color-singlet model (CSM) was suggested soon after the discovery of the J/ψ. In the CSM, charmonium states are considered as non-relativistic bound states of $c\bar{c}$. Where $c\bar{c}$ interact via a confining potential. The J/ψ is a color-singlet, $^3S_1$ state of $c\bar{c}$ system. The dominant production mechanism of a heavy quarkonium is assumed to be the one in which it is produced at short distances in a color-singlet $Q\bar{Q}$ state with quantum numbers matching the quarkonium state. Furthermore the angular momentum quantum number of $Q\bar{Q}$ should be same as that of the given quarkonium state.

To understand the color-singlet model, the production of charmonium can be divided in two steps. In the first step pair of $c\bar{c}$ is produced. In the second step $c\bar{c}$ pair binds into a charmonium state. The relative momentum of $c\bar{c}$ pair must be small compared to m_c in $c\bar{c}$ rest frame if we want significant probability for binding. If this is not the case then c and $\bar{c}$ will quickly fly away, forming D and $\bar{D}$ mesons. It also assumes that a $c\bar{c}$ pair produced in a color-octet state will not bind to form charmonium according to color-singlet model. At some level this assumption must break down as a color octet $c\bar{c}$ pair can make a transition to a color-singlet state by radiating a soft gluon (non-perturbatively). Quarkonium production in CSM has been studied for years. Differential cross-sections at leading order in CSM were calculated a decade ago [11, 12, 13, 14]. A few total cross section formulae have been evaluated at next-to-leading order as well [14].

In 1995 the most dramatic failure of the color-singlet model came by CDF collaboration. They calculated the production cross sections for charmonium states at the Tevatron $p\bar{p}$ collider. At large transverse momentum, the cross sections for the direct production of J/ψ and $\psi(2s)$ were 30 times larger than the predictions of the color-singlet model. This dramatic discrepancy marked the final demise of the color-singlet model [10].

1.4.3 NRQCD Model

In order to get more realistic understanding and description of the charmonium production, which is not obtained from the CEM and CSM, a new model was suggested by Braaten, Bodwin and Lepage. This model is named as NRQCD (Non-Relativistic QCD) . The factorization scheme was modified in this model from the earlier model. This allowed a mediating bound state with quantum numbers different than those of the real charmonium state. The NRQCD is an Effective Field Theory (EFT) that uses the renormalization ideas as well as fully exploits the properties of the local quantum field theories. The EFT describes the phenomena in a limited range. The limit on the theory is set by an intrinsic energy scale Λ. The charmonium system is almost non-relativistic. There are several energy scales which can be separated by the velocity v of the heavy quark in the $c\bar{c}$ center-of-mass system: $m \gg mv \gg mv^2$. The first two scales have good separation. This separation distinguishes the heavy quark creation process which can be studied in the perturbative QCD from all other processes of the order $m_c v$. The wave-function of charmonium state is almost local in comparison with the size of charmonium, at the scale of charm quark mass m_c. NRQCD model cannot be claimed as a precise model for charmonium production, even though there are many successes of NRQCD model but still there are some uncertainties which are given below:

- In most cases, expansion in NRQCD converges very slowly
- there can be uncertainty from higher order correction in α_s as large as 100%.
- the non-perturbative matrix elements calculations are still difficult to perform either using experiments or lattice calculations,

- large errors can come from uncertainty in the mass of charmonium if production rates depend on a high power of the charmonium mass.

Despite all these problems the NRQCD model is still the most comprehensive of the models described here. The CEM accounts for the color octet processes but it makes additional restrictions. The CSM can be obtained from NRQCD by removing the color octet contributions. In order to avoid the failures of the model (absence of polarization and equal ratios of quarkonium cross sections), CEM is limited to apply only to cross sections that are summed over the spin states of quarkonium and in the case when the total hadronic energy is sufficiently large.

1.4.4 k_T Factorization

The k_T factorization method [15, 16] starts from Color-Singlet quarkonium production model and it incorporates the initial state radiation through parton distribution functions which include the transverse momenta, k_T , additionally to the longitudinal momentum fraction x, of the incident partons. A nice comparison between conventional approach which assumes that all particles involved in the calculation of parton level cross sections have only longitudinal components of their momenta. The k_T factorization approach can be found at [17].

1.5 Summary of Charmonium Measurements

The ratio χ_{c2}/χ_{c1} has already been measured previously in several experiments. Measurements of hadronic χ_j production have been made in a variety of beam types and energies by observing the decay process $\chi_j \to J/\psi\ \gamma$. These measurements have been performed with small ranges of transverse momentum and rapidity. With the current measurement, we improve the sensitivity to theoretical models by extending the $J/\psi\ p_T$ spectrum beyond the spectra measured by CDF and LHCb. The branching ratios of $c\bar{c}$ states are summarized in Table 1.4.

CDF experiment measured the the ratio $R_p = \sigma_{\chi_2}\ \mathrm{Br}(\chi_{c2} \to J/\psi\ \gamma)\ /\ \sigma_{\chi_1}\ \mathrm{Br}(\chi_{c1} \to J/\psi\ \gamma)$, in 1.1 fb^{-1} of pp collision at $\sqrt{s} = 1.96$ TeV. The measurement covers the kinematic range $p_T\ (J/\psi) > 4.0$ GeV/c, $\eta < 1.0$, and $p_T(\gamma) > 1.0$ GeV/c. For events due to prompt processes, we find $R_p = 0.395 \pm 0.016 \pm$

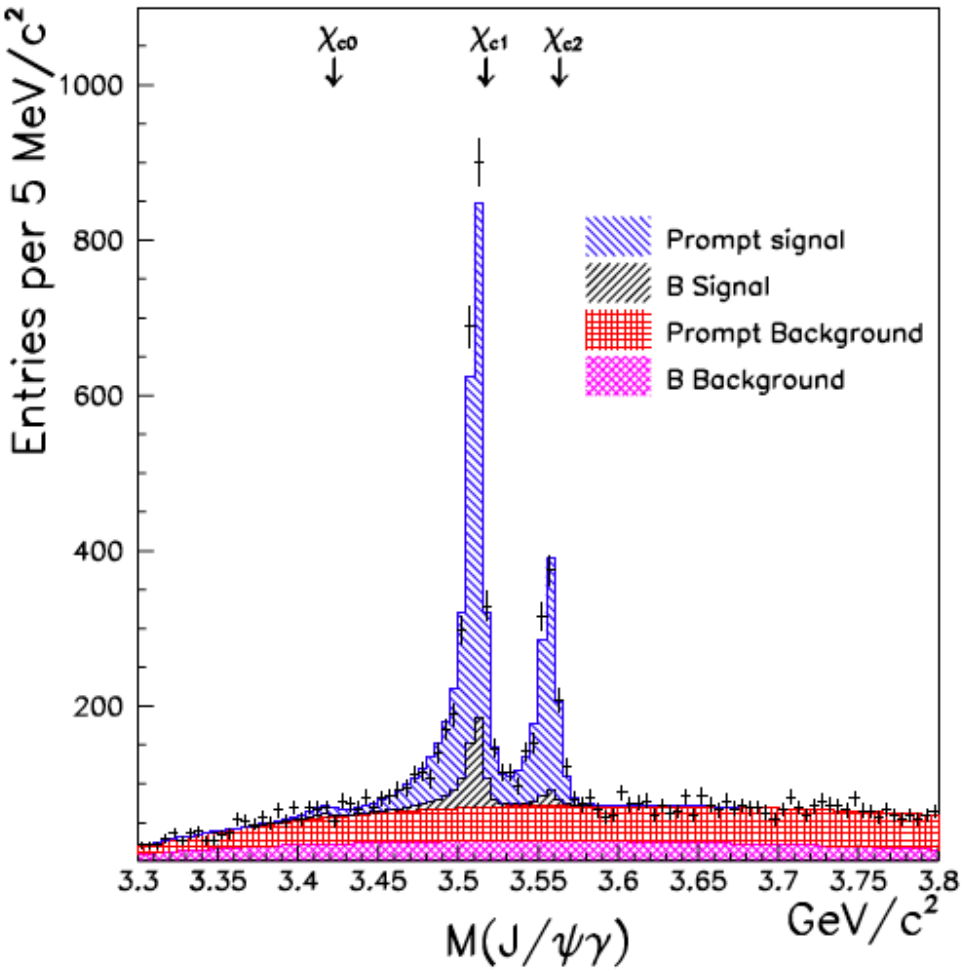

Figure 1.2: Result of CDF

(stat) $\pm$ 0.015(syst). The $J/\psi\gamma$ mass distribution (points) with the projection of the likelihood fit overlaid on the data. The masses of the χ_c mesons and the contributions of the signal and background components are indicated in Figure 1.2

LHCb also measured the ratio χ_{c2}/χ_{c1} in bins of 2 GeV/c $< p_T(J/\psi) <$ 15 GeV/c [18]. The LHCb results are shown with solid black circles in the rapidity range $2.0 < y(J/\psi) < 4.5$ using 36 pb^{-1} of LHC data at $\sqrt{s} = 7$ TeV. These results are based on the assumption that the χ_c is produced unpolarized. Figure 1.3 shows the resuls of LHCb and also the comparison with CDF results and the NRQCD model. The ChiGen generator describes the shape of the distribution reasonably well, although the data lie consistently above the model prediction. This could be explained by important higher order perturbative corrections and/or sizeable

Particle	Mass[MeV/c^2]	Width[MeV/c^2]	Br($c\bar{c} \rightarrow \mu^+\mu-$)
J/ψ	3096.92 $\pm$ 0.01	0.093 $\pm$ 0.002	5.93 $\pm$ 0.06
χ_{c0}	3414.75 $\pm$ 0.31	10.5 $\pm$ 0.8	1.16 $\pm$ 0.08
χ_{c1}	3510.66 $\pm$ 0.07	0.88 $\pm$ 0.05	34.4 $\pm$ 1.5
χ_{c2}	3556.20 $\pm$ 0.09	1.95 $\pm$ .13	19.5 $\pm$ 0.8

Table 1.4: Branching ratios of $c\bar{c}$ states from PDG [49]

colour-octet terms not included in the calculation. The results are in agreement with the NLO NRQCD model for $p_T(J/\psi) > 8$ GeV/c.

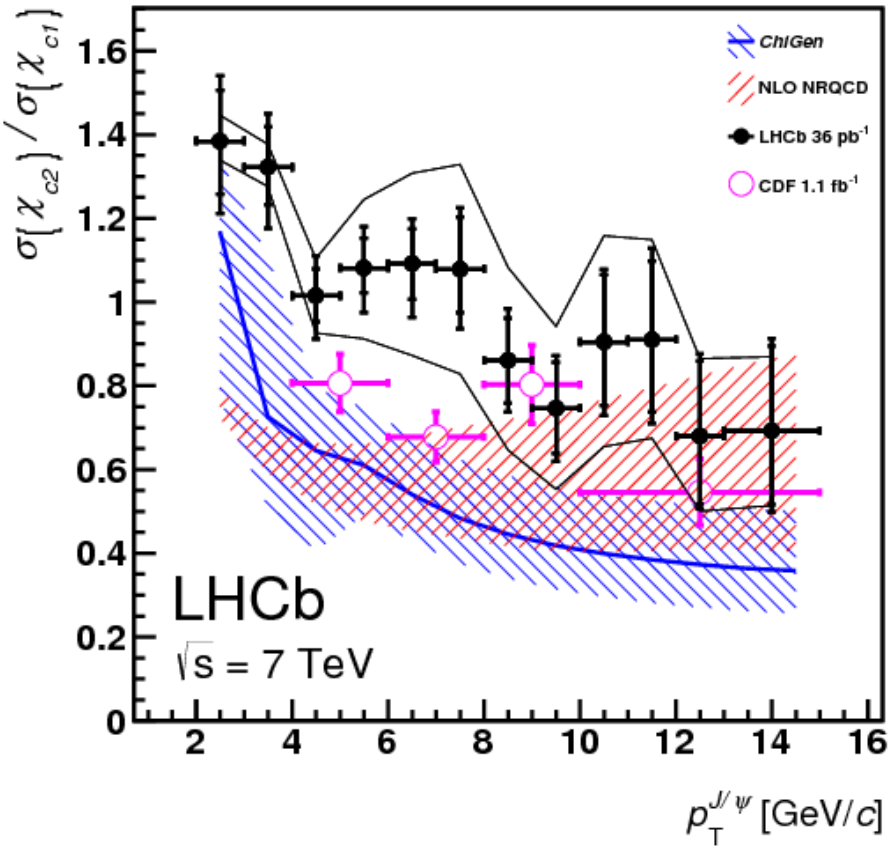

Figure 1.3: Result of LHCb measurement of cross section ratio of χ_{c2} and χ_{c1}

Chapter 2

The Compact Muon Solenoid(CMS) Experiment

The new frontiers of particle physics are the searches for extremely elusive particles, which are produced in processes with very low cross sections, the femto barn being the natural unit. With current technologies, leptonic colliders are not able to reach the high energies needed for these searches, which can presently be achieved only with hadron colliders. Despite the production of a lot of low energy particles resulting in a not clean environment, a proton-proton collider if compared to a leptonic interaction, offers the possibility to span over a wider energy spectrum that can be explored simultaneously and permits to reach higher production rates. These are the motivations for the CERN to build a huge proton-proton (pp) collider named as Large Hadron Collider (LHC).

2.1 Large Hadron Collider(LHC) at CERN

The superconducting magnet of the Large Hadron Collider (LHC) has two-rings to accommodate protons moving in opposite direction inside. It can accelerate and collide proton and lead nuclei. The LHC ring is installed in the already existing tunnel at CERN laboratories in Geneva, Switzerland. The LHC tunnel is 26.7 km in circumference. The LHC tunnel is build 100 m underground across the French-Swiss border. The main physics goal are the search of Higgs boson, testing of the standard Model of particle physics and new physics beyond the standard Model at the energy scale of 1 TeV. The LHC is designed for both proton-proton and

heavy ion collisions with a center of mass energy of 14 TeV for pp collision and 5.5 TeV for heavy ion collision with a luminosity of $10^{34} cm^{-2} s^{-1}$ and $10^{28} cm^{-2} s^{-1}$ respectively [19].

There are four major experiments (see Figure 2.1) built along the path of LHC tunnel to observe the collisions. Two of them, CMS [20] and ATLAS [21], are the general-purpose detectors. The main goals of these two collaborations is the exploration of the limits of the Standard Model, searches of Standard Model and Supersymmetric Higgs bosons, supersymmetric partners of the Standard Model particles and high precision physics of t and b quarks. The other two experiments are LHCb [22] and ALICE [23]. The LHCb experiment is dedicated for the b-physics studies, where the heavy ion collisions are principally studied at specialized ALICE experiment, with CMS and ATLAS also having a heavy ion programs.

2.1.1 Main Goals of LHC

Our current understanding of the universe leave us with many unsolved questions. The main goals of LHC are to answer these questions, some of them are following:

- Why elementary particles have mass and why their masses are different. The Higgs mechanism could be one of the answer to this question. The Higgs field has at least one new particle associated with it, the Higgs boson. The LHC has discovered Higgs in July 2012 but its properties are still needed to be understood in detail.

- Why all the visible matter in the Universe counts for only 4% of the total mass. A supersymmetric model (SUSY) can be a possible answer. SUSY predicts that for each known particle there is a supersymmetric partner. For each boson there is fermion partner and vice versa. If SUSY is right, then supersymmetric particles should be found at the LHC.

- Why there is more matter in our universe than antimatter. Both must have been produced in the same amounts at the time of the Big Bang. LHC could provide an answer to this mysterious problem.

2.1.2 Machine parameters

Initially protons are accelerated and brought up to 50MeV by a linear accelerator LINAC. A Booster then raise the beam energy up to 1.4 GeV injecting proton beams into the old circular accelerator PS (Proton Synchrotron). The 25 GeV energy beams extracted from PS then injected to a bigger circular accelerator SPS (Super Proton Synchrotron), which finally introduce 450 GeV proton beams into the LHC ring, where they are accelerated to their nominal energy of 7 TeV. The tunnel of LHC is a 26.659 km circumference, composed of 8 curvilinear sections (2.840 km) and 8 rectilinear sections, where the beams are brought to collide. The Figure 2.1 shows the schematic view of the CERN accelerator complex and some technical parameters of LHC machine are summarized in Table 2.1.

Circumference (km)	26.7
Number of Dipoles	1232
Length of Dipole (m)	14.3
Dipole Field Strength (Tesla)	8.4
Operating Temperature (K)	1.9
Current in dipole super conducting coils (A)	13000
Beam Intensity (A)	0.5
Beam Stored Energy (MJoules)	360
Magnet Stored Energy (MJoules) per sector	1100
Sector Powering Circuit	8

Table 2.1: Technical aspects of LHC

2.1.3 Luminosity and Run 2011

LHC has been running successfully achieving most of it's goals earlier than expected times. In 2010 it delivered 50 pb^{-1} of data at $\sqrt{s} = 7$ TeV. In 2011 it was able to provide 6 fb^{-1} at same energy to each of the general purpose detector i.e ATLAS and CMS. In 2012 the centre of mass energy was increased to 8 TeV and LHC delivered about 23 fb^{-1}.

The event rate at the LHC can be estimated using the relation.

$$\mathscr{N}_{event} = \mathscr{L}\sigma_{event} \tag{2.1}$$

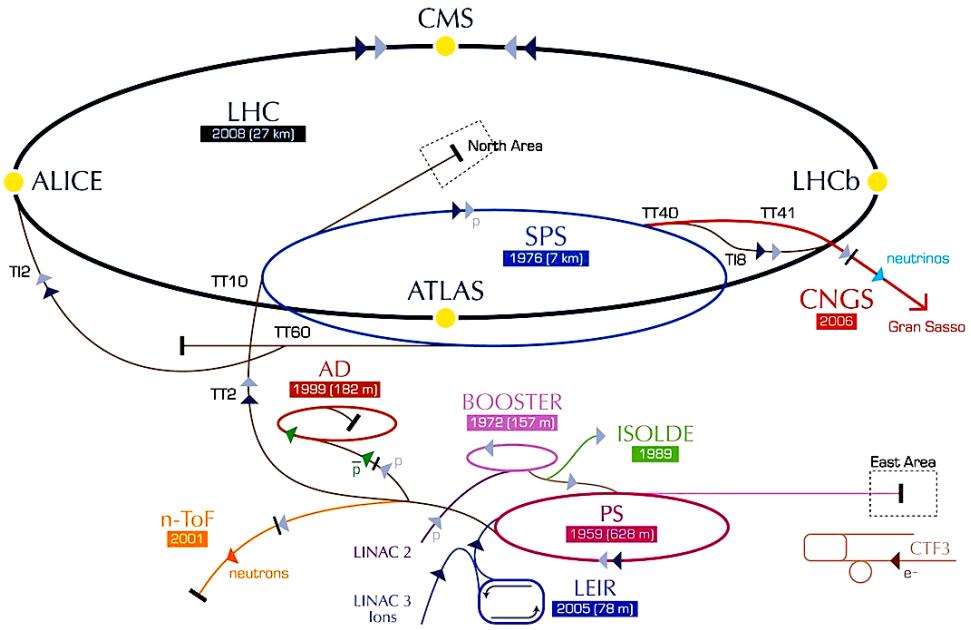

Figure 2.1: Layout diagram of Large Hadron Collider at CERN (LHC)

where σ_{event} is the cross section for the physics process under study and $\mathscr{L}$ is the machine luminosity, which depends only on the beam parameters. The luminosity of the LHC can be given by the expression [24].

$$\mathscr{L} = \frac{\gamma f k_B N_p^2 F}{4\pi\epsilon_n \beta^*} \tag{2.2}$$

where γ is the Lorentz factor, f is the revolution frequency, k_B is the number of bunches, N_p is the number of protons/bunch, ϵ_n is the normalized transverse emittance(with a design value of 3.75 μm), β^* is the betatron function at the IP, and F is the reduction factor due to the crossing angle. The designed energy of LHC for each proton beam is 7 TeV. The design luminosity $\mathscr{L} = 10^{34} cm^{-2} s^{-1}$ leads to around 1 billion proton-proton interactions per second. The LHC became operational in November 2009 and reached the maximum energy of 1.18 TeV per beam. In 2010 and 2011 LHC operated with energy of 3.5 TeV per beam. The physics data of integrated luminosity of 50 pb^{-1} and 6 fb^{-1} was delivered by the LHC in 2010 and 2011 respectively. The summary of 2011 luminosity plot is presented the Figure 2.2.

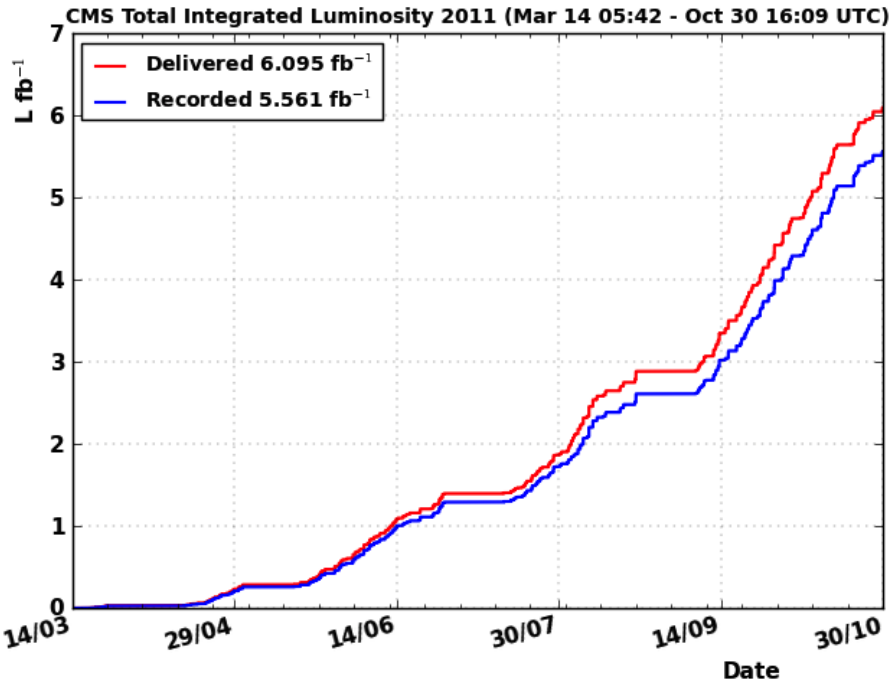

Figure 2.2: Integrated luminosity plot for 2011 data, delivered by LHC and collected by CMS [32].

2.2 Compact Muon Solenoid (CMS)

The Compact Muon Solenoid (CMS) is a multipurpose particle detector designed to study pp-collisions at the Large Hadron Collider at CERN; see Figure 2.3. The Compact Muon Solenoid experiment, CMS [25], is a general purpose detector which will operate at LHC. The main feature of CMS is the 4 T superconducting solenoid that permits a compact design of the detector with a strong magnetic field. The design priorities fulfilled by the CMS project are a redundant muon system, a high quality tracking system and a good electromagnetic calorimeter. CMS has an excellent muon system assisted by central tracking detector and solenoid produces a magnetic field twice large as used by ATLAS. This allows the accurate particle momentum measurement. The detector is made up of five wheels for the barrel part and 6 disks (three on each side) for endcap part. It is 21 m long, 15 m wide and 15 m high and weighs 12500 tons. A cross-sectional view of CMS can be seen in Figure 2.4.

The main goals of the experiment are precision study of standard model, explore physics at the TeV scale, discovery of the Higgs boson, search for physics

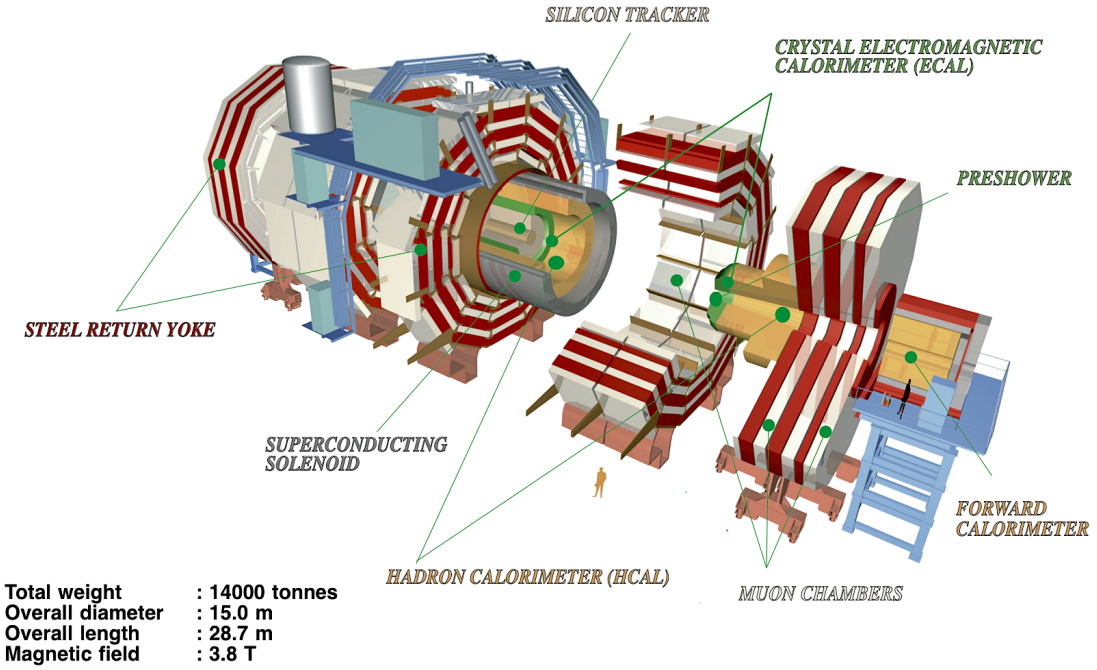

Figure 2.3: The schematic diagram of Compact Muon Solenoid (CMS) at LHC

beyond the standard model e.g extra dimensions , supersymmetry and study aspects of heavy ion collisions.

2.2.1 CMS Coordinates

The Compact Muon Solenoid (CMS) coordinate conventions are such that the interaction point which lies in the middle of barrel part where the two beams collides is referred as the centre of the CMS coordinate system. The positive x-axis is the direction of inward radius from CMS to the center of the LHC ring. The positive y-axis is vertically upward to the surface and the z-axis is along the direction of the beam pipe. The polar angle θ is measured in y-z plane form z -axis. The azimuthal angle ϕ is measured in the x-y plane from x-axis. There are some other kinematic parameters we will use in our analysis are pseudorapidity, rapidity, transverse momentum and transverse energy which are defined as following:

- **Rapidity**: $y = \frac{1}{2} \ln \frac{E+p_z}{E-p_z}$
- **Pseudorapidity**: $\eta = -\ln(tan(\theta/2))$
- **Transverse momentum**: $p_T = \sqrt{p_x^2 + p_y^2}$

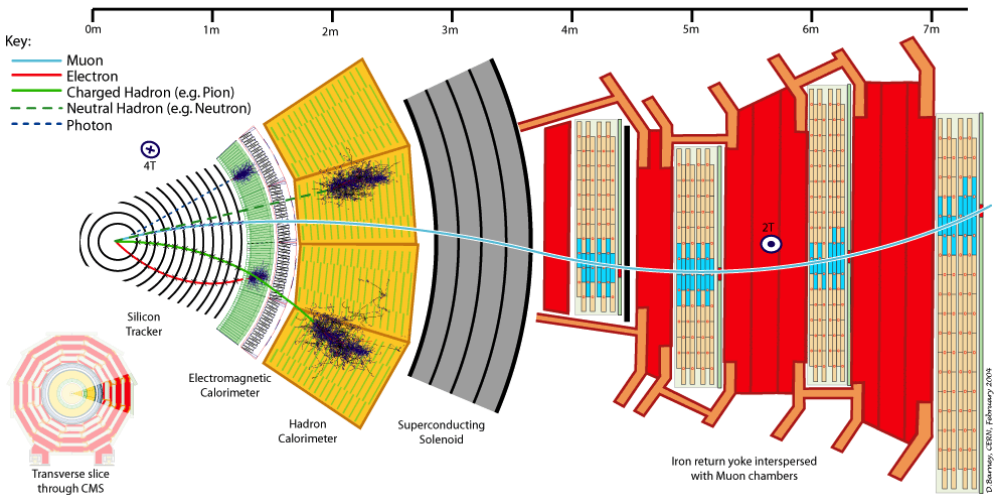

Figure 2.4: A cross sectional view of CMS Detector showing layers of sub-detectors and path of detectable particles

- **Transverse energy**: $E_T = Esin(\theta)$

2.2.2 Detector Requirement

To meet the goals of the LHC physics program, the detector requirement for CMS can be summarized as follow [20]:

- Ability to determine unambiguously the charge of muons with p $<$ 1 TeV, muon identification and momentum resolution over a wide range of momenta and angles and good dimuon mass resolution (1% at 100 GeV).

- Efficient triggering and offline tagging of top quark and b-jets, requiring pixel detectors close to the interaction region. Good charged-particle momentum resolution and reconstruction efficiency in the inner tracker.

- Good electromagnetic energy resolution, π^0 rejection, efficient photon and lepton isolation at high luminosities, good diphoton and dielectron mass resolution (1% at 100 GeV), wide geometric coverage.

- Good missing transverse energy and dijet mass resolution, which implies hadron calorimeters with fine lateral segmentation and a large hermetic geometric coverage.

2.2.3 Superconducting Magnet

The superconducting magnet is the central feature of the CMS detector. This is a solenoidal magnet, designed to produce magnetic field of 4 Tesla (see Figure 2.5). The diameter of cylindrical solenoidal magnet is 6 m which is 12.5 m long along beam pipe. Energy stored in this magnet at full current is 2.6 GJ [26]. The CMS experiment aims to produce the strongest magnetic field as a higher strength of field will bend paths of charge particles more. An accurate measurement of the momentum of charged particles at even high energies would be possible by combining the high precision position measurements in the tracker and muon detectors. A 220 ton cold mass is most prominent feature of the the 4-layer

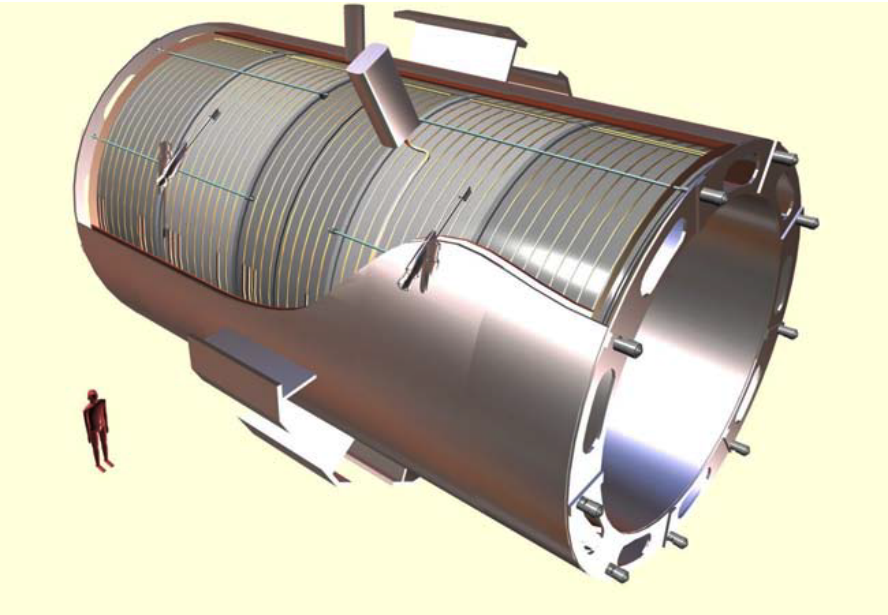

Figure 2.5: Superconducting solenoidal magnet of CMS

winding which is constructed with a stabilized reinforced NbTi conductor. To maximize the lifetime of the magnet the operating field was reduced to 3.8 T instead of the 4 T. The tracker and calorimeter detectors (ECAL and HCAL) are surrounded by the magnet coil while the muon detectors are interleaved with a 12 sided iron support. This iron structure works as return yokes for the magnetic field. These return yokes also acts as a filter. It allows only weakly interacting particles such as neutrinos and muons and to reach muon system. Some important parameters of superconducting magnet are summarized in Table 2.2:

Magnetic length (km)	12.5m
Total Ampere-turns	41.7 MA-turns
Inductance	14.2H
Stored energy	2.6 GJ
Nominal current	19.14 kA
Central magnetic induction	4 T
Cold bore diameter	6.3m

Table 2.2: General Parameters of Superconducting Magnet

2.2.4 Tracking system

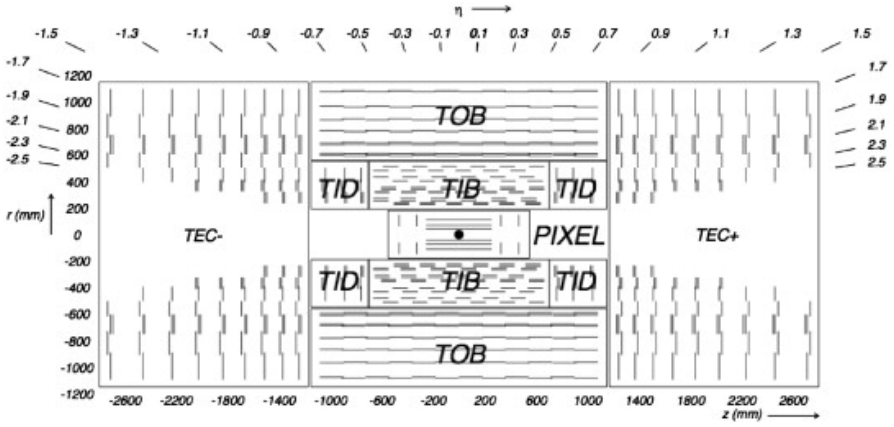

Figure 2.6: CMS pixel and silicon tracker: Different geometrical layers

CMS tracking system is used to give precise reconstruction of secondary vertices as well as an efficient and precise measurement of the paths of charged particles coming from the pp-collisions in LHC ring [27]. Schematic diagram of CMS tracker system is shown in Figure 2.6. The tracking system is around the interaction point with a diameter of 2.5 m and a length of 5.8 m in the form of a cylinder. A uniform magnetic field of 4 Tesla is produced by CMS solenoid over the full volume of the tracker.

There are two parts of CMS tracker:

- Pixel detector: It has three layers in the barrel region between beam pipe and a radius of 10.2 cm. It has two disks on each side forming forward/endcap pixel

- Silicon Strip tracker with 10 barrel detection layers extending outwards to a radius of 1.1 m and the endcap contains 3 (pixel) plus 9 (Silicon Strips Tracker) disks on each side. The pseudorapidity coverage of tracker extends to $\eta < 2.5$ after including endcaps. Thus endcaps increase the tracker acceptance.

This gives 13 layers for barrel part of tracker and 14 layers on each side of endcaps. The pixel part has 66 million pixel each of dimension 100 $\times$ 150 μm. The first four layers of silicon strip tracker which extends upto 55 cm in radius has strips of dimension 10 cm $\times$ 180 μm. The next six layers have strips of dimension 25 cm $\times$ 180 μm extending in radius to 1.1 m. There are 9.6 million channels in silicon strip tracker.

CMS tracking system is made to take the huge particle flux coming for LHC collisions. The CMS tracker consists of about 20000 silicon sensors with a total area of 210 m^2 having a diameter and length of about 2.4 m and 5.4 m respectively thus its acceptance is up to $\eta < 2.5$. Tracker is the first detector around beam pipe and interaction region so it will get highest flux of particles. Around 1000 charged particles can produce tracks for each bunch crossing at the radius of about 4 cm. So a tracker should be radiation hard in the inner most part. Tracking information at high level trigger is used to reduce the event rate from 40MHz to about 100Hz.

Pixels

The area of Pixel detector is about 1 m^2. The number of pixels in pixel detector are around 66 million while size of each pixel is around 100×150 μm^2. The pixel tracker has two parts:

- Barrel: It has three cylindrical layers of length of 53 cm around beam pipe at radii of 4.4 cm, 7.3 cm and 10.2 cm.

- Endcap: It consists of two disks on each side of the barrel at z = $\pm$32.5 cm and $\pm$46.5 cm. These disks complement the barrel part and increases the acceptance of detector. Furthermore there will be three space points with high precision for every charged particle with $\eta < 2.5$ detected in the tracker.

The schematic diagram of the CMS tracker detector is shown in Figure 2.7.

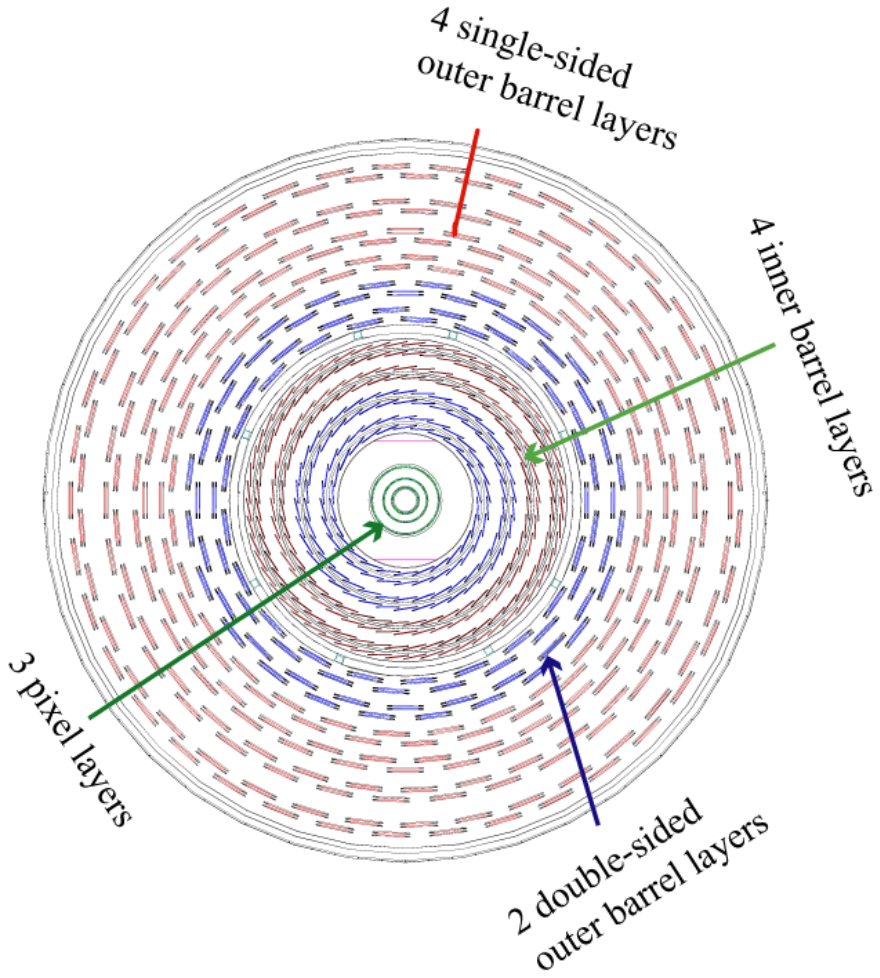

Figure 2.7: CMS tracker: cross sectional view

Silicon Strips Tracker

The Silicon Strip tracker lies in the radial region between 20 cm and 116 cm. This part of tracker has four parts.

- Tracker Inner Barrel (TIB): It has four concentric layers of cylindrical shape at different radii. Four TIB layers are plac ed in the detector with radius of 25.50 cm , 33.90 cm, 41.85 cm and 49.80 cm from the centre of detector respectively, with a length of 1.4 m along beam pipe with interaction region at the center. The first two layers have double-sided modules while the outer two layers have single-sided modules.

- Tracker Inner Disk (TID): The TID has three disks on both sides of barrel. There are three rings of modules on each disk.

- Tracker Outer Barrel (TOB): This part contains a single mechanical cylindrical structure supporting 688 module sub-assemblies (from a total of 5200 Silicon modules) called rods. Every rod gives support and cooling for 6 or 12 silicon detector modules, together with their interconnection and readout electronics. There are six layers of rods on TOB with average radii of 608 mm, 692 mm, 780 mm, 868 mm, 960 mm, and 1080 mm. The cylinder has a total length of 2360 mm and inner and outer radii of 555 mm and 1160 mm respectively such that it covers the TIB/TID sub-detector.

- Tracker endcap (TEC). The two endcaps has wedge shaped carbon fiber support plate called petals. These plates carries up to 28 modules arranged in 7 radial rings on each side. A total of 6400 modules are mounted on 288 petals to form 18 such disks for TEC+ and TEC-. The end-caps extend radially from 220 mm to 1135 mm and from $\pm$1240 mm to $\pm$2800 mm along the z-direction. Other than above seven disks there are 2 more disks on each side of endcap serving as front/back termination.

Meterial Budget in CMS Tracker

A high track reconstruction efficiency is of great importance for the reconstruction of charged particle tracks. In general, the reconstruction efficiency is not limited by the resolution of the tracker. The particles produced by the hadronic interactions at collision points, interact with the service materials (LV, HV, Cooling, Electronics) of tracker detector. The inefficiency is observed due to this service material. The service installations include on-detector electronics and cooling systems. Figure 2.8 shows the material budget in units of radiation length X_0, as a function of pseudorapidity for different tracker layers and service installations. At $\mid \eta \mid \approx 1.4$ there is an increase of the material budget because of cables and cooling pipes between the TIB and TOB, and the TID and TEC.

An efficient cooling is required if we use high power density for the electronics on detector. This is against our requirement of keeping the amount of material to the minimum in order to limit photon conversion, nuclear interactions, multiple scattering and bremsstrahlung. To achieve high track reconstruction efficiency in

high material density regions as well as in the whole tracker a special approach of iterative track reconstruction is used.

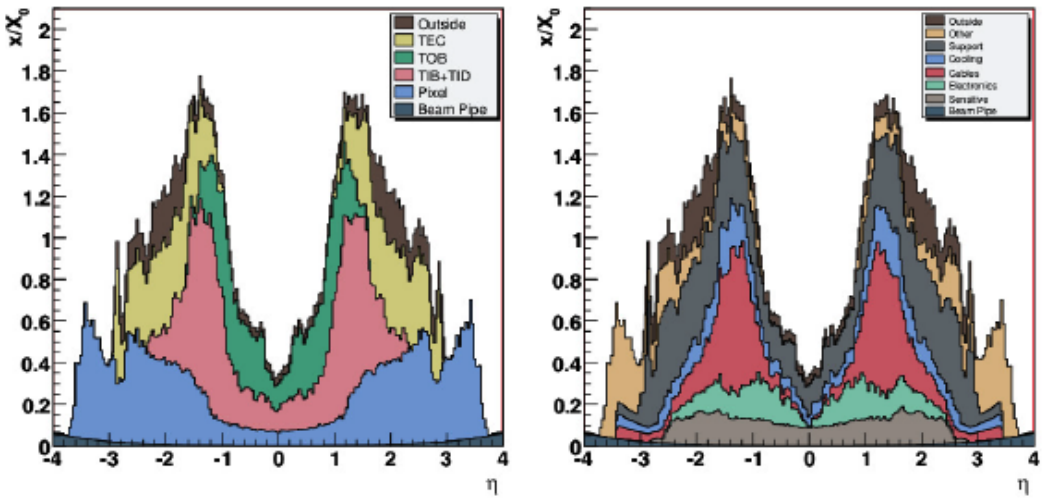

Figure 2.8: The material budget in units of radiation length as a function of pseudorapidity for different sub detectors (left) and functional contributions (right) [20]

2.2.5 Electromagnetic Calorimeter (ECAL)

The Electromagnetic Calorimeter used in the CMS is designed to have precise measurement of the electron, photon energy and direction [28]. ECAL is positioned outside the tracking system at the distance of 120 cm from the point of interaction. For a good energy resolution and fine granularity for spatial resolution lead tungstate ($PbWO_4$) crystals are used. These crystals are used due to its high density around 8.28 g/cm^3, small Moliere radius of 2.2 cm and short radiation length of 0.89 cm. The ECAL has two parts see Figure 2.9; one in the shape of cylinder along beam axis and the other in the form of endcap disk.

The ECAL barrel (EB) goes up to the pseudorapidity range $|\eta|<$ 1.48 with the 61200, total number of lead tungstate ($PbWO_4$) crystals. The crystal face toward the interaction point has the radial distance of 1.29 m from the collision center. They are called front faces. The avalanche photodiodes is used to collect the signal in the form of light in the barrel part.

The ECAL crystals are trapezoidal in shape. The cross-sectional area of rear

side of ECAL crystal is 26×26 mm^2 and front side of the crystal is 22×22 mm^2 or 0.0174×0.0174 in η-ϕ. The length of the crystal is 25.8 X_0 or 230 mm. In the barrel region total weight of crystals is 67.4 ton and its volume is approximately 8.14 m^3. The light produced in the crystals is gathered with silicon avalanche photodiodes. Around 80% of the light is emitted in the first 25 ns. In the endcap region the area of cross section is 28.62 × 28.62 mm^2 and the length of each crystal in the endcap region is 220 mm which corresponds to the radiation length of 24.7 X_0.

The endcaps ECAL (EE) cover the rapidity range $1.48 < |\eta| < 3.0$. The longitudinal distance between the endcap envelope and the interaction point is 315.4 cm. The endcap consists of identical shape crystals which are grouped in mechanical units. Each unit consists of 55 crystals called super crystals (CS). Each endcap is divided into 2 halves. Each half contains 3662 crystals. There are 138 standard super crystals and 18 special partial super crystals on the inner and outer circumference. At front the cross-sectional area of the crystals is 28.6 × 28.6 mm^2 and at rear face cross section is 30 × 30 mm^2. The crystal have a length of 220 mm (24.7) X_0. The energy resolution of ECAL is measured as:

$$\frac{\sigma_E}{E} = \frac{2.8\%}{\sqrt{E(GeV)}} \oplus \frac{0.128}{E(GeV)} \oplus 0.03\% \tag{2.3}$$

where E is the energy in GeV.

ECAL also has preshower detectors which is located in front of the endcap. Main purpose of CMS preshower is to reduce photons coming from neutral pions in the endcap by their identification in the forward region, $1.65 < |\eta| < 2.60$. Preshower is a sampling calorimeter which has two layers. The first layer have lead radiators which initiate electromagnetic showers from incoming e or γ. The second layer measures the energy deposited and the transverse shower profiles using its silicon strip sensors which are placed after each radiator.

2.2.6 Hadronic Calorimeter (HCAL)

The Electromagnetic calorimeter is surrounded by Hadron Calorimeter HCAL [29]. HCAL is used together with the electromagnetic one to measure the energy and direction of jets, the transverse energy E_T and the imbalance of transverse

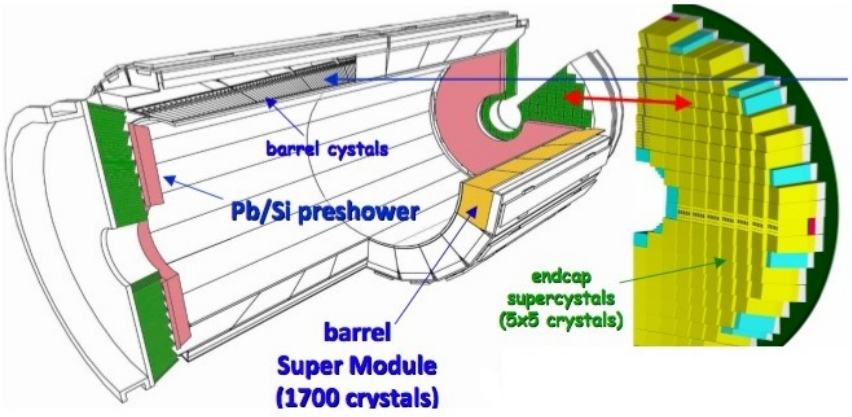

Figure 2.9: Layout of electromagnetic calorimeter (ECAL) of CMS

energy, or missing transverse energy, E_T^{miss}. To fulfill these requirements, it has to be thick enough to contain the whole hadron shower and have high hermeticity. Since it is placed inside the magnet, it can not be made with ferromagnetic materials. HCAL is a sampling calorimeter with 3.8 mm thick active layers of plastic scintillators alternated with 5.5 cm thick brass plate absorbers. The granularity $\Delta\eta \times \Delta\varphi$=0.087×0.087 is fine enough to allow an efficient di-jet separation. Brass plate absorbers are used in HCAL have density 8.53 gcm^{-3}, radiation length 1.49 cm and interaction length of 16.42 cm.

HCAL can be divided into four parts: barrel (HB), outer barred (HO), endcap (HE) and Hadron forward (HF), see Figure 2.10. The barrel part covers the η < 1.3, Hadron endcap covers the range from 1.3 <η< 3.0. The Hadron endcap receives high counting rates as compared to the barrel part. For eta less than 1.3 Hadron Outer barrel (HO) is used to cover this η ranges. The forward calorimeter (HF) covers the η region up to 5.2.

2.2.7 Muon Chambers

Muons are involved in the final state of many interesting physics processes. At designed LHC luminosity, they also come as background with very high rate. Muon detection can be used to reduce the size of background and improve resolution for interesting processes. The decay of the SM-Higgs to ZZ or $ZZ^{\star}$ is a well known example of final state with muons, where the Z can decay into 4 leptons. The

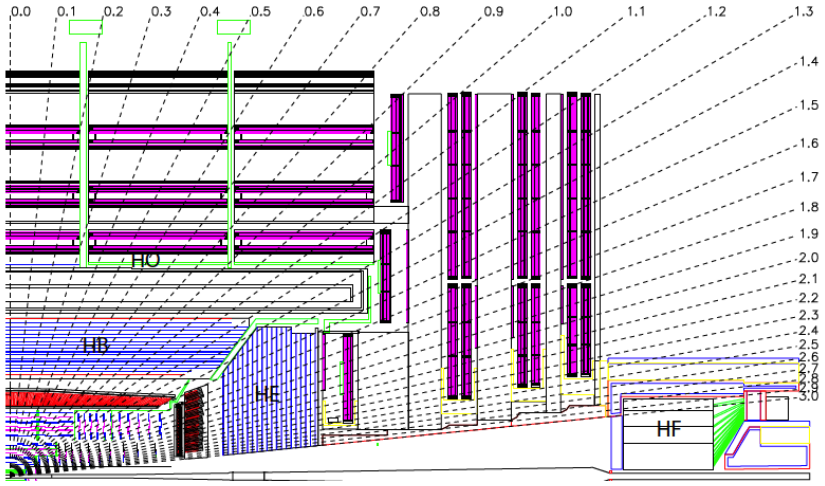

Figure 2.10: Schematic layout of Hadronic calorimeter (HCAL) of CMS

case when all four leptons are muon is called golden channel. Muon chambers has also significant importance in the study of new physics, top physics and b-physics, where muons are used as the final particles.

The CMS muon system is designed to reconstruct the momentum and charge of muons over the the entire kinematic range of the LHC [30]. It contains muons detectors as well as supporting material to hold these detectors. The supporting material also serve as guides for the magnetic field lines. The Muon system is developed to provide a fast identification, efficient reconstruction and triggering by muons. Three are three different type of detectors in the CMS muon system.

- Drift Tubes (DT): They are installed in the barrel region and are used to get position information.
- Cathode Strip Chambers (CSC): They are installed in the endcap region are used to get position information.
- Resistive Plate Chambers (RPC): They are installed in both barrel and endcap region and used to get the timing information.

DT, CSC and RPC are all gaseous detectors. A schematic diagram of muons system in Figure 2.11 showing RPCs , CSCs and DTs . Barrel regions is divided in five wheel and endcap in three disks.

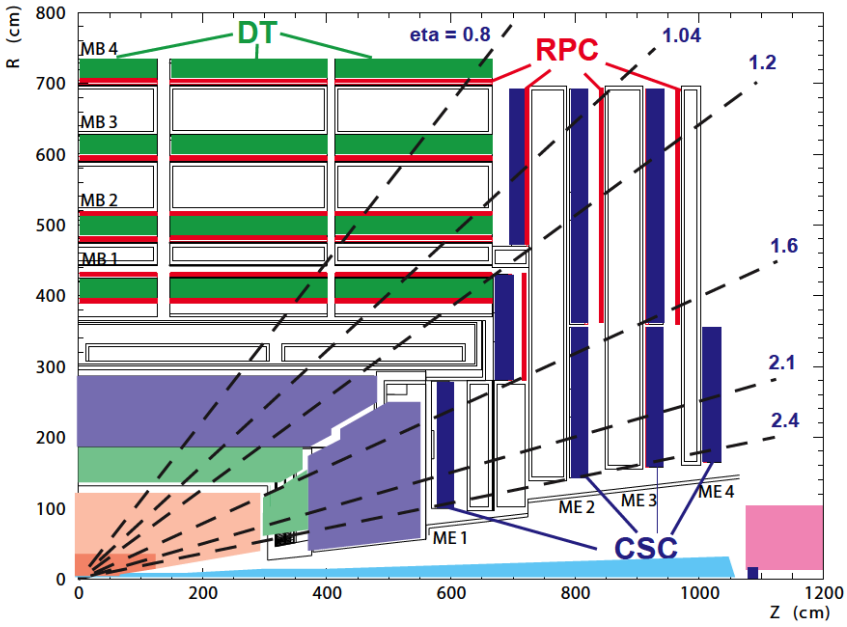

Figure 2.11: Geometrical layout of Muon chambers of CMS, showing RPCs , CSCs and DTs

Drift Tubes

The drift tubes in the barrel region has standard rectangular drift cell geometry. Here the neutron background is small, the muon rate is low. The magnetic field is uniform and parallel to the beam line. The drift tube (DT) chambers are used to measures muon positions in the barrel region in the pseudorapidity region $|\eta|$ < 1.2. The gas mixture used in the DT is 85% Ar + 15% CO_2.

The DT chambers are organized in 4 stations among the layers of the return yoke. The first 3 stations contain 12 chambers per wheel, which measure the r-ϕ and z coordinates of the muons. The chambers in the fourth station are 14 per wheel and they measure only the r-ϕ coordinate of the muons. In each of the 12 sectors of the yoke there are 4 muon chambers per wheel, labeled MB1, MB2, MB3 and MB4. In total, there are 250 DT chambers in the barrel. Figure 2.12 shows schematic diagram of drift lines in DT-cell. The voltages applied to the electrodes are +3.6 kV for wires, +1.8 kV for strips, and -1.2 kV for cathodes.

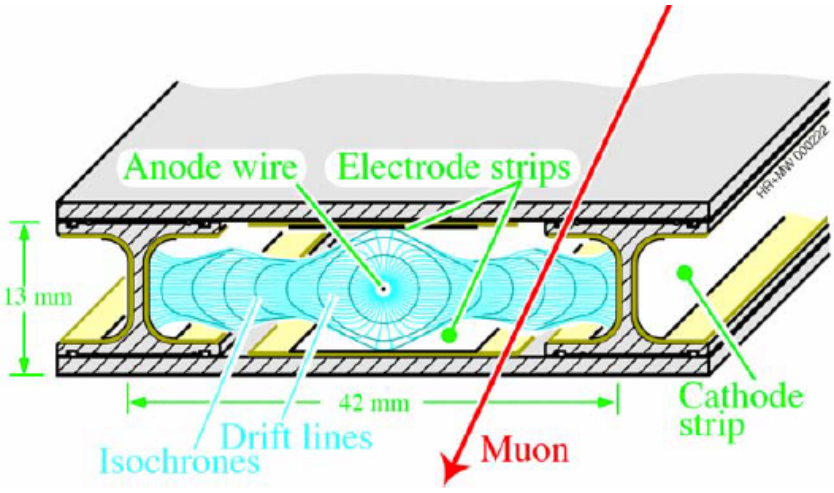

Figure 2.12: A unit cell of drift tube chamber

Cathode Strip Chambers

In the endcap regions of CMS, cathode strip chambers (CSC) are used due to the large and non-uniform magnetic field. The muon rates and background levels are high in this region. The CSCs can identify muons in the pseudorapidity range from 0.9 to 2.4 using its fast response time, radiation resistance and fine segmentation. In the pseudorapidity region $0.9 < |\eta| < 1.2$ endcap CSCs and the barrel drift tubes (DT) overlap each other, so in this region muons are detected by both detectors.

There are 468 cathode strip chambers (CSC) in the CMS endcap muon system. They are installed on four disk stations (ME) in each side. The CSCs geometry is that of a multiwire proportional chamber having seven cathode panels interleaved with six anode wire planes. The gas mixture used in CSCs contains 40% of Ar, 50% of CO_2 and 10% of CF_4. The operating point of 3.6 kV was chosen as nominal high voltage.

Resistive Plate Chambers

A typical RPC used in CMS experiment is double gap gaseous detector. Each gap of RPC consists of two parallel plates, which are made by high resistive material (with resistivity 10^9 - 10^{12} Ωcm). The thickness of each gass gap is 2 mm. The outer surfaces of the resistive material are coated with graphite paint to form the HV and ground electrodes. The readout is performed by means of copper strips

separated from the graphite coating by an insulating Polyethylene (PET) film [31]. The RPC chamber is operated in avalanche mode, whose design considerations have been proven successfully in several tests.

There are two parts like all other sub-detectors i.e barrel and endcap RPCs. The RPCs give an independent, fast, and highly-segmented trigger in the rapidity region of $\mid \eta \mid < 1.6$ of the muon which has a sharp p_T threshold. The RPCs are made in two layers of gas chambers to increase the efficiency. To make RPCs operation good at high flux they are used to operate in avalanche mode. There are 6 layers of RPCs sandwiched between muon support system and drift tubes, two in each of the first two stations, and one in each of the last two stations. Low p_T tracks would stop before reaching the outer two stations. The trigger algorithm to work for low p_T tracks due to the two layers on the first two stations. There are three RPCs disks on each side of the endcap such that there is one disk on each support system. The trigger is developed such that it reduces background and improves the time resolution for bunch crossing identification as well as it achieves a good p_T resolution. RPC's are discussed in chapter 3 in more detail.

2.2.8 CMS Trigger System

The LHC provides pp and PbPb-collisions at high interaction rates. The designed frequency for LHC bunches is 40 MHz which corresponds to an interval of 25 ns between two bunch crossings. Depending on luminosity, there can be more than one collision for every bunch crossing (For proton bunches at designed luminosity of $10^{34} cm^{-2} s^{-1}$ there can 20 collisions per bunch crossing.

To reduce the event rate different selection criteria is used at hardware level as well as at software level, known as triggers. The hardware trigger is known as Level-1 (L1) Trigger while software trigger is called High-Level Trigger (HLT). The L1 Trigger uses programmable electronics and custom designed to reduce the data while collisions are ongoing. The HLT, which is a selection criteria at software level, can be applied after data passing L1 trigger is stored in a filter farm having large number of commercial processors. Level-1 and HLT combines can reduce the event rate by a factor of 10^6.

The CMS trigger system is designed to deal with the high luminosity and interaction rates at the LHC. The trigger system has to reduce the 40 MHz event rate to a final rate of about 100 Hz, while maintaining a high efficiency for a broad variety of physics processes. This reduction level is done through three levels of triggering. The Level-1 (L1) reduces the rate to 100 kHz in the high luminosity regime and 50 kHz for the low luminosity phase. The L1 decision to pass the event to the next level of trigger must be taken in 3.2 μs.

The L1 trigger uses only a coarse granularity information from calorimeters and muon system because the decision must be taken in a time which is very short to read all the data from the whole detector, see Figure 2.13. The High Level Trigger (HLT) is designed to reduce the L1 output rate of 100 kHz to the output rate of 100 Hz. The HLT code performs the reconstruction and selection of physics objects using the full event data with the granularity and matching information from different sub-detectors. These objects are electrons, photons, muons, missing energy, hadronic jets. The selection or rejection of such objects allows to achieve the output rate of 100 Hz for events in the permanent storage medium.

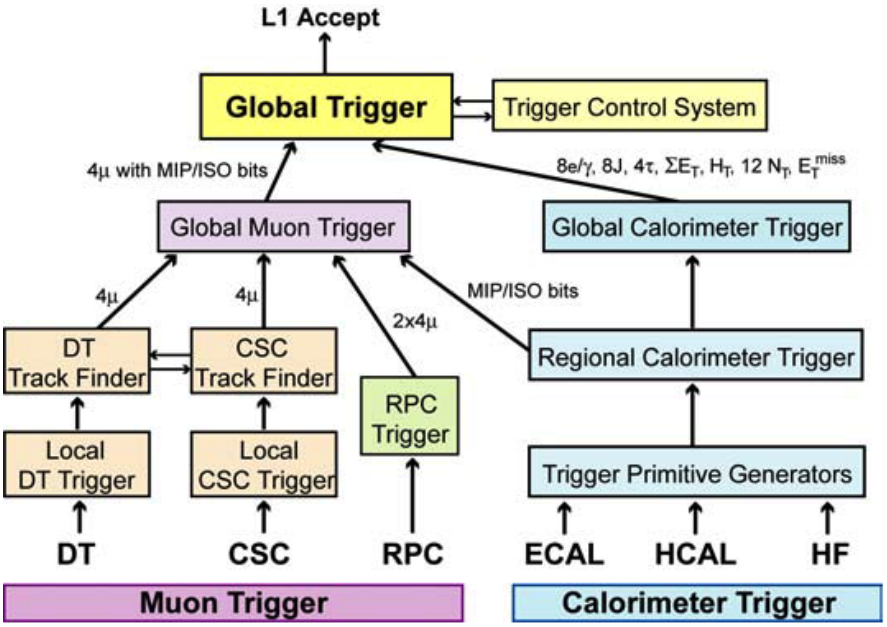

Figure 2.13: Level-1 Trigger structure of CMS

Chapter 3

Commissioning of Endcap RPCs

The main purpose of commissioning is to certify that the performance of our detector is still of the same level as during the production and test phases. It also means that all the services needed to operate the chambers are working properly. The performance of RPC detector is based on the parameters including occupancy, efficiency, cluster-size and dark current.

Commissioning of whole endcap RPCs was responsibility of Pakistani group. Commissioning was performed in the year 2008-09. RPC sub-systems tested for good performance during commissioning are Gas System, High Voltage System, Low Voltage System, Cooling system, Detector Readout System and Detector Control System(DCS).

RPCs are installed on CMS in barrel region as well as in endcap region. There are three disks of endcap RPCs on each side of CMS i.e RE±1, RE±2 and RE±3. Each disk constitute of three rings, the outer one is named as RE*/3, middle one is named RE*/2 while inner one is named RE*/1 and each ring contains 36 RPC. Each RPC can be represented by RE±D/R-N, where D and R represent the Disk number and Ring number respectively while N represent the number of RPC in each Disk. The size of RPCs increases from inner to outer rings, also known as layers. The chambers on RE*/2 and RE*/3 can be seen in Figure 3.1.

A major part of work required for assembling and commissioning of endcap RPCs has been done by Pakistan for CMS. The four complete disks RE±2 and RE±3 were assembled in Pakistan while same rings for disk RE±1 was assembled in China. The endcap RPCs disks RE±1, RE±2 and RE±3 are commissioned

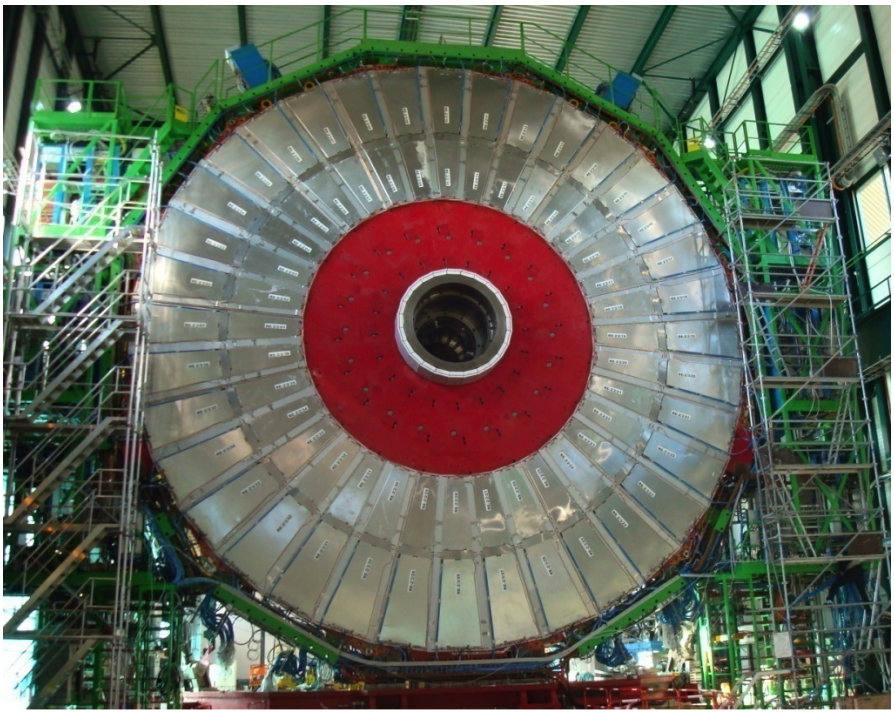

Figure 3.1: A complete Disk of endcap RPCs of CMS. RPC are installed in Ring2 and Ring3 where Ring1 is empty.

by the Pakistani team at CMS during 2008-09. The overall geometry, efficiency, working principal and various stages of the commissioning of the Resistive Plate Chambers are explained in different sections of this chapter.

3.1 Resistive Plate Chambers

The RPC consists of two parallel plates made out of bakelite with a bulk resistivity of $10^9 - 10^{10}\Omega$ cm, separated by a gas gap of 2 mm [33]. The whole structure is made gas tight. The outer surfaces of resistive material are coated with conductive graphite paint to form the high voltage and ground electrodes. The readout is performed by means of copper strips separated from the graphite coating by an insulating Polyethylene film. RPCs have an excellent time resolution which is crucial at Large Hadrons Collider (LHC) due to the beam crossing time of 25 ns. These are the dedicated chambers used for the first level muon trigger. The good performance of RPC is very essential in assigning the muon to the right bunch crossing. The event rate at LHC is expected to be extremely high due to the

large total pp cross section at $\sqrt{s} = 14$ TeV. The expected event rate is 40 MHz which is unmanageable, Level-1 (L1) trigger is applied to reduce this size to 100 KHz. This rate at the output of L1 is too high to be stored, therefore the high level trigger is applied and the final event rate is brought down to the 100 Hz. At L1 trigger the available time for the detector is 25 ns, which implies fast trigger system. Resistive Plate Chambers (RPCs) are good candidates for fast triggering, where the spatial resolution is not important but fast timing information is more important. The cross-sectional view of the CMS is shown in Figure 3.2.

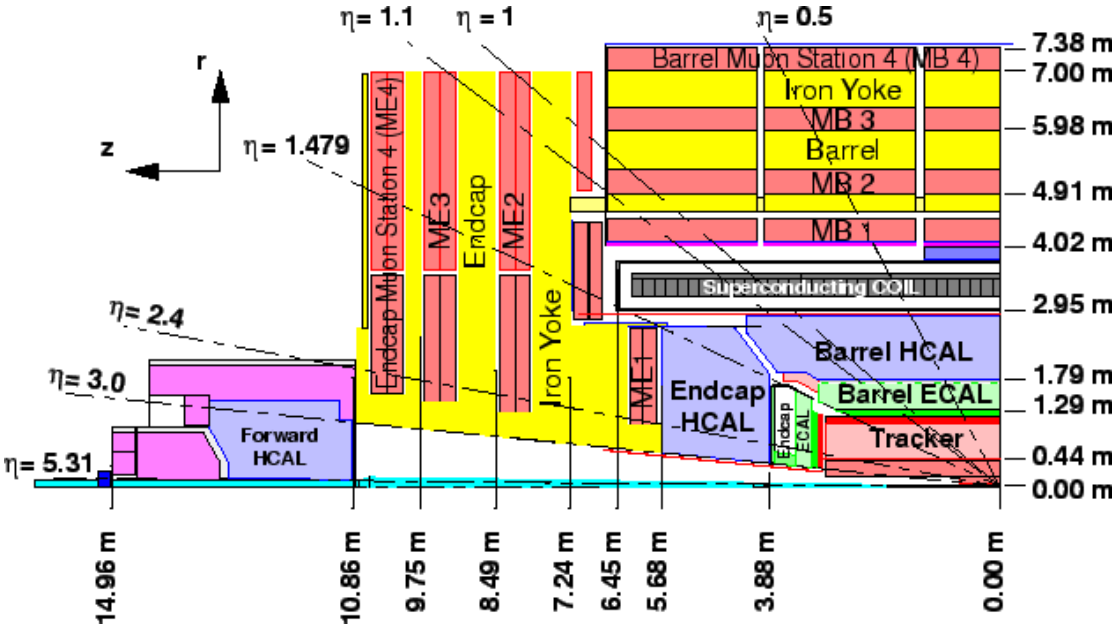

Figure 3.2: View of a quadrant of CMS in rz-plane where MB and ME are the barrel and endcap Muon system layout.

3.1.1 Geometry Of Endcap RPCs

The shape of the endcap RPC is trapezoidal and it covers 10 degrees in ϕ. The strips are also trapezoidal in shape. The endcap RPCs are double gap chambers with 96 readout strips running perpendicular to the beam line (in ϕ). Table 3.1 shows the geometrical details of RPCs and corresponding parameters are displayed in Figure 3.3.

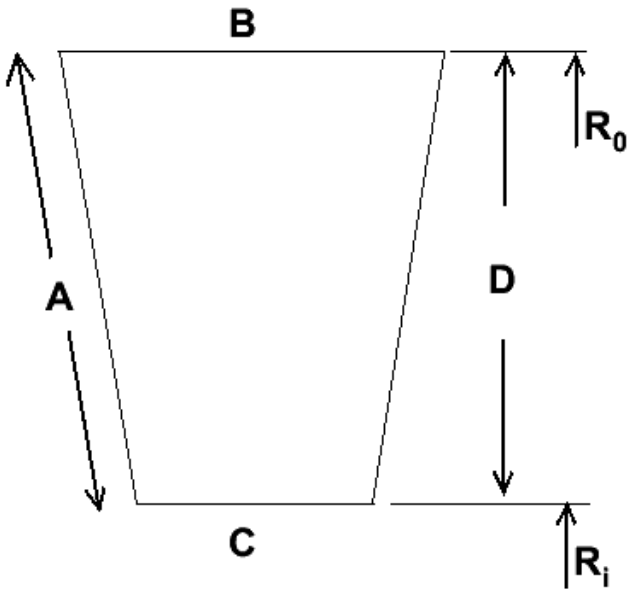

Figure 3.3: Geometry of a Resistive Plate Chamber where, R_0 is radius from beam line (low eta), and R_i is the radius from beam line (high eta).

Station	R_i	Chambers	A(mm)	B(mm)	C(mm)	D(mm)	Area(m^2)
RE 2/2	3299	72	1693	979	684	1687	1.403
RE 2/3	5001	72	1961	1323	981	1954	1.917
RE 3/2	3299	72	1693	979	684	1687	1.403
RE 3/3	5001	72	1961	1323	981	1954	1.917
Total	-	288	-	-	-	-	513.2

Table 3.1: Dimensions of RPC installed in Ring2 and Ring3.

3.1.2 Modes of Operation

The two modes of operation for RPCs are the streamer mode and the avalanche mode. In the streamer mode the electric field inside the gap is kept intense enough to generate the limited discharges localized near the crossing of ionizing particle. The resulting signal size is large but the rate capability obtained in such operational conditions is limited (100 Hz/cm^2) which is not adequate for LHC. For data taking in cosmic ray applications, RPCs were run in streamer mode, in which the resulting pulses were large enough that no amplification stage was required.

A significant improvement achieved by operating the detector in the so-called

avalanche mode. The electric field across the gap (and consequently the gas amplification) is reduced and a robust signal amplification is introduced at the front-end level. The substantial reduction of the charge produced in the gap led to high rate capability.

3.1.3 RPC Performance Parameters

Performance of RPC is determined from it's behavior which can be determined by different parameters. These parameters are occupancy, efficiency, cluster size, time resolution, dead time and rate capability. Their details are given below.

Occupancy: It gives region of RPC which can detect a muon or a region which is alive. This number depends on the number of strips in that region and efficiency of RPCs.

Efficiency: It is ratio of working strips to total strips in an RPC. For an ideal detector efficiency should be 100%. But in real life a good detector will have efficiency above 95%.

Efficiency plateau: When efficiency of RPC is measured vs voltage applied across gaps then the resulting curve behaves like an error function i.e it starts from low values, quickly increases to highest value and stays constant for a certain range of voltage. The part where efficiency is highest and constant is called the efficiency plateau.

Cluster sizer: It is number of consecutive strips which collect signal (charge) due to a muon passing through gaps. We can have a muon for which all charge is collected by one strip or if it passes through junction of two strips then charge is collected by two strips. Thus avalanche size at the end of 2mm gap should not be wider than two strips. Experimentally this value lies close to 2.

Dark current: It is a current which is detected in electronics when there is no voltage applied across gas gap. The sources of dark current could be leakage current, loose electronics etc.

Dead Time: It is period of time during which a detector can not detect a particle passing through it. The reason of dead time is a muon which has already ionized the gas molecules and lowered the voltage across gaps. We can not make dead

time zero as ionized gas takes some time to get neutral again.

Time Resolution: It is time during which signal is collected by RPC.

Rate Capability: It gives number of charged particles which can be detected in unit area in unit time. This number depends on the granularity of a detector as well as on its dead time and time resolution.

For best performance assembled RPC has to fulfill the following conditions before installation at the CMS detector:

- Cluster Size < 3.
- efficiency > 97 %
- Operation Efficiency plateau > 400 V.
- Time resolution < 3 ns.
- Dead time around 3 ns
- Rate Capability > 1 KHz/cm^2.

3.2 Commissioning of Forward RPCs

Commissioning is needed to make sure that all the systems are behaving as they did during testing i.e the whole chain of connections is done properly for HV cables, LV cables, Signal cables, Gas pipes, Cooling pipes and DCS-system. Commissioning is very important because each and every system from chamber to control room is tested and verified. Commissioning is required because transportation of system could damage or effect the detectors in part or as whole. Endcap RPCs were first transported to ISR testing area in CERN, Meyrin site and then to point 5 surface area where they were installed on endcap disks. Then the disks along with RPCs were lowered about 100m where final CMS detector resides.

Commissioning was performed for positive endcap as soon as hardware for low voltage (LV) and high voltage (HV) systems was received. All chambers were attached to the final gas system, LV system, HV system and signal readout. Gas was continuously flushed through the whole positive endcap. LV was turned on

for all except few chambers and the HV system was complete and has been tested for all chambers. Same procedure was repeated for negative side.

3.2.1 High Voltage System: HV

Operating voltage for RPCs is 9.2 kV. For commissioning all chambers were supplied a high voltage of 9.2 kV. The limit of dark current was set to 10 μA per chamber. The trip time was set to 10 sec. There are three RPC stations on each side of CMS namely RE+1, RE+2, RE+3, RE-1, RE-2 and RE-3. Each station has 72 RPCs installed. This comes to 432 chambers on six stations. HV was supplied to top and bottom gaps separately. So there were total of 864 channel which needed to be controlled with HV system. Hardware used for HV system is shown in Table 3.2. The names are listed by top down hierarchy. A distribution box was

No.	Model	Name	Quantity
1	SY1527	HV Mainframe	1
2	A3485N	3-phase AC/DCs Converter (MAO)	1
3	A1676N	Branch Controller	3
4	EASY 3000	Easy Crates	8
5	A34FU	Fan Units for Easy Crates	8
6	A3512N	High Voltage Modules	36
7	Home Made	HV Distribution Boxes	24

Table 3.2: Hardware used in High Voltage System

added after each easy crate to minimize the cost due to commercial products. Distribution box distributed one HV channel to four channel i.e two chambers. Thus reducing the expenditure due to HV Modules by a factor of four. Details of each commercial product can be found on company's web page [35]. Some necessary information is given in the HV layout.

HV Layout: The layout is shown in Figure 3.4. HV main frame can be accessed and controlled from CMS DCS. It controls branch controller which further control up to six Easy Crates. There are 16 slots available in the back of mainframe for HV modules/branch controller out of which first one is occupied by branch controller. Mainframe has hardware current protection and communication via

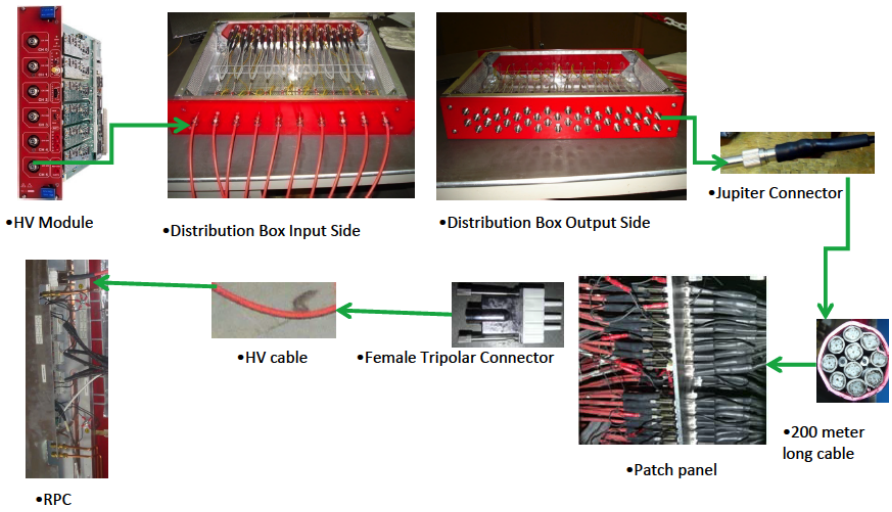

Figure 3.4: Block diagram of HV system

TCP/IP. Figure 3.5 shows a Mainframe Power Supply SY1527 and an Easy crate EASY 3000 respectively. Each Easy Crate has 21 slots and occupies six units of height in a standard rack. High Voltage Modules take three slots. In principle there can be seven High Voltage Modules or six Low Voltage Modules in each easy crate. The EASY 3000 is designed to operate in region of high magnetic field and radiations. It is powered up with the help of a two channel 400 V ac to 48 dc converter (A3485). The A3485 (or MAO) gives 2.5 KW, 48 Volts dual output with 50 A maximum output current. This MAO can be controlled remotely with the help of a branch controller A1676N. A separate branch controller was used for this as the one used to control EASY 3000 can not be utilized for this purpose. Proper cooling fan units were installed for MAO and for each easy crate.

Cables from HV modules are connected to HV distribution box (see details in Section 3.2.2). The output of distribution box is connected to umbilical cord which is about 100 m long and goes from service cavern to experimental cavern of CMS experiment. Umbilical cable is a bunch of 10 HV cables. In rack room, it's connected to distribution box while in experimental cavern it's connected to HV patch panel. Only 9 out of 10 cables are currently in use. The 10th cable is left as a spare. There are total of 28 umbilical cables for positive endcap, fourteen for near-side and fourteen for far-side. The position of these umbilical cables in the HV Rack is shown in Figure 3.6. In the experimental cavern these cables are

Figure 3.5: (Top) Main Frame Power Supply, (Bottom) Easy Crate

connected to a patch panel (PP). From patch panel there is another set of HV cables used which distribute HV to each gap on a chamber. There is a patch panel at the edge of each chamber (as shown in Figure 3.7) to distribute different services within a chamber. Pairs of chambers which are powered up by same channel from HV module are shown in Figure 3.8.

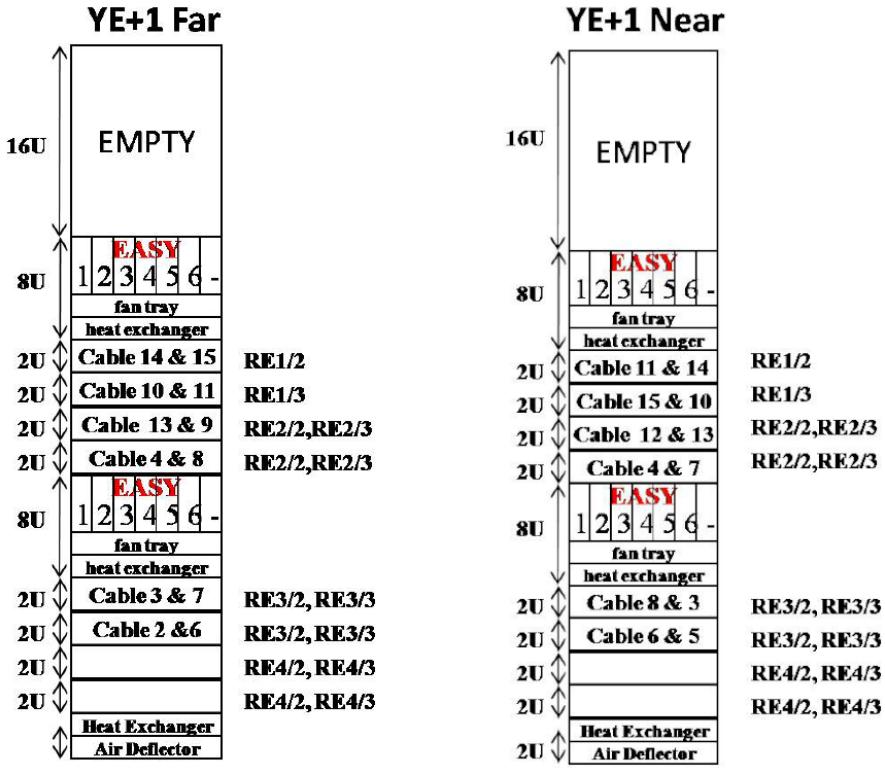

Figure 3.6: High Voltage patch pannel for endcap RPCs.

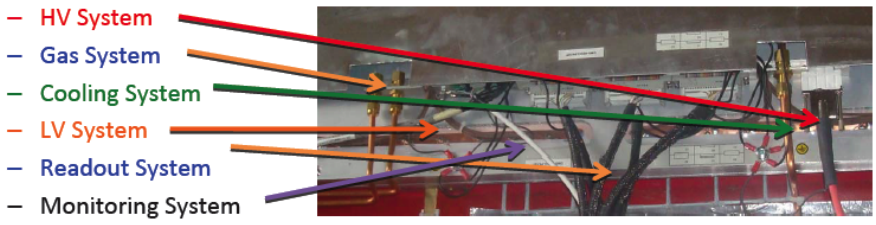

Figure 3.7: Patch panel at the edge of chamber.

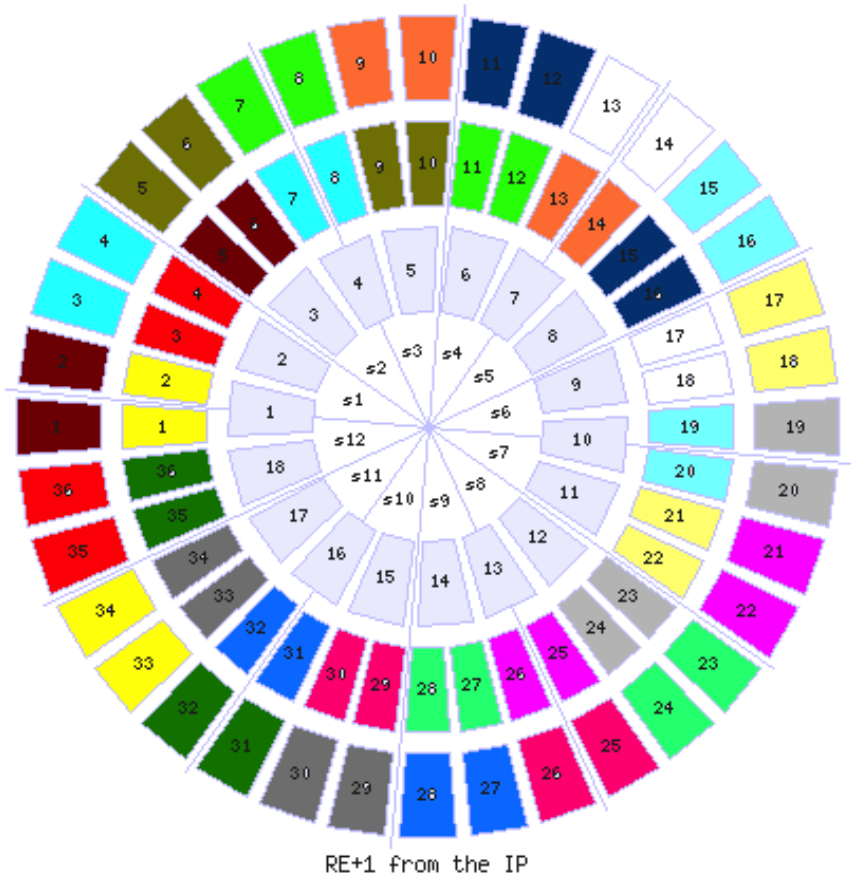

Figure 3.8: Pair of chambers connected to one channel of HV modules.

3.2.2 HV Distribution Box

High voltage modules are very expensive. So high voltage distribution boxes are used to distribute the power. The high voltage distributor actually converts a single input voltage into four output voltages, two for bottom gap and two for top gap. The boxes were prepared at ISR. Preparation was done in following steps

1. Preparation of empty box to house cables
2. Making ground cables
3. Making of connectors
4. Soldering of 1 to 4 cables
5. Epoxy filling
6. Testing at 15kV

For positive endcap system 12 distribution boxes are needed to be installed in the HV control room. If there are 10 input channels, the total number of output channels is 40. These are insulated from each other with stycast or epoxy 2651-40. Infra red light is used to heat the epoxy so its viscosity is decreased and it becomes easy to mix. An 18% of sty cast LV 23 is used as catalyst. Figure 3.9 shows a high voltage distribution box. Hence 4 distribution boxes are required for a single disk and 12 distribution boxes for 3 wheels or for positive endcap. The total number

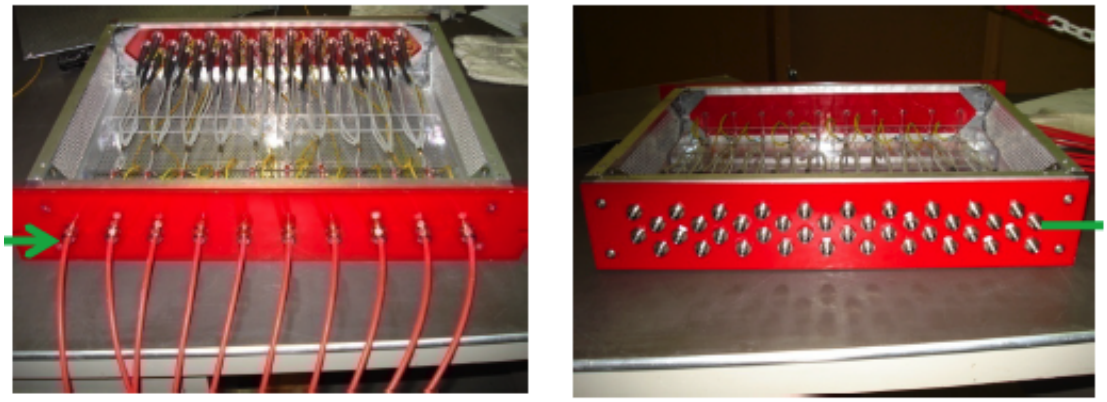

Figure 3.9: HV distribution box

of chamber which can be powered on by a single distribution box is 18. Out of 40, 4 output are kept as spares.

3.2.3 Testing

Output of commercial products: Each of hardware mention in Table 3.2 was tested at Bldg. 904 in CERN, Prevessin site. Different values of HV was applied via keyboard which controlled mainframe. Output voltage and current V_{mon}, I_{mon} were observed.

HV Distribution box: Output was terminated with 50 Ω resistance. Input voltage was varied from 0 to 15kV in regular steps and dark current was measured. The distribution boxes are tested channel by channel with the help of a Multi-channel power supply. Channels were tested at various voltages and the current corresponding to given voltage was noted. The Figure 3.9 shows the HV distribution boxes testing results.

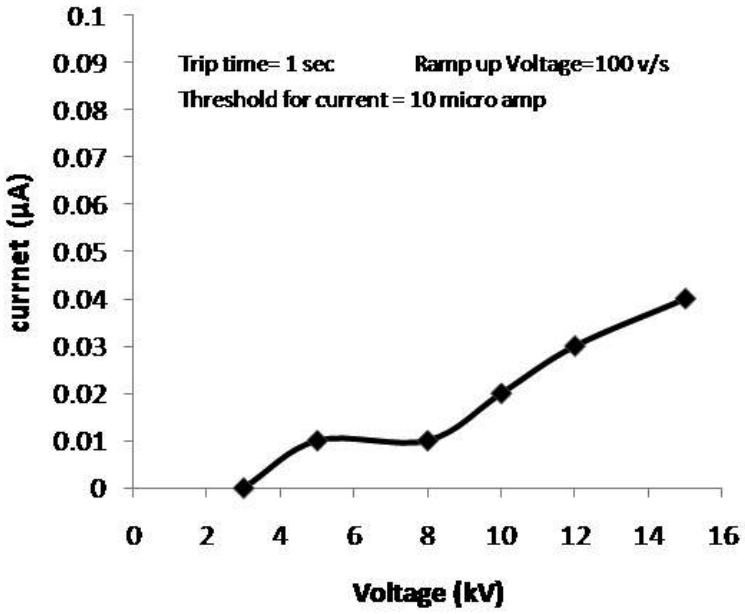

Figure 3.10: HV distribution box test results

HV Cables: High voltage system is installed in the High voltage control room according to the rack lay out. The Figure 3.6 shows the detailed HV rack layout in the HV control room. The system was tested piece by piece; starting with HV cables which are connected between patch panel and distribution boxes. The

cables from chambers to patch panel were already tested at the time of installation of these cables.

The cables were tested by connecting them with the High Voltage module (Model no A3512N) housed in the multichannel power supply SY1527 in the HV control room. The high voltage cable coming from control room is disconnected from the chamber at the Patch Panel. Tripolar female connectors are inserted at the patch panel instead of the chamber cable in this way the chamber is disconnected from the high voltage cable. The high voltage cable between patch panel and distribution box is made of four conductor cable. At the patch panel end two grounds are joined. So that it can be attached to tripolar connector. At distribution box end it is attached to two Jupiter connectors. Each Jupiter connector has an HV conductor and other ground conductor. The Jupiter connectors are labeled as top or bottom such that when whole chain is connected the top provides HV to top gap and bottom provides HV to the bottom gap of the same chamber. A loose connection at either end, patch panel or distribution box can result in large fluctuation in the voltage and corresponding dark current. It is important to make the connections as much tight and clean as possible.

No.	Model	Name	Quantity
1	SY1527	LV Mainframe	1
2	A3485S	3-phase AC/DCs Converter (MAO)	12
3	A1676N	Branch Controller	4
4	EASY 3000S	Easy Crates	24
5	A34FU	Fan Units for Easy Crates	24
6	A3009	LV FEB Modules	36
7	A3016	LV LBB Modules	24

Table 3.3: Hardware used in Low Voltage System.

Cable Testing: The cables are tested at 5, 10, 12, and 15 kV, the current limit is set to 10 μA, ramp up voltage is set to 100 volts/sec and ramp down voltage is 150 volts/sec. The current which the cable draws must not exceed 0.1 μA. The current corresponding to the 'Top' and 'Bottom' is noted from the multichannel power supply. There is a limit set on the current drawn by each chamber which

CH#	Board-1 LV cables	Board-2 LV cables	Board-3 LV cables
1	RE2/2-13,RE2/3-13 A	RE1/2-07,RE1/2-08 A	RE1/3-07,RE1/3-08 A
2	RE2/2-13,RE2/3-13 D	RE1/2-07,RE1/2-08 D	RE1/3-07,RE1/3-08 D
3	RE2/2-14,RE2/3-14 A	RE1/2-09,RE1/2-10 A	RE1/3-09,RE1/3-10 A
4	RE2/2-14,RE2/3-14 D	RE1/2-09,RE1/2-10 D	RE1/3-09,RE1/3-10 D
5	RE2/2-15,RE2/3-15 A	RE1/2-11,RE1/2-12 A	RE1/3-11,RE1/3-12 A
6	RE2/2-15,RE2/3-15 D	RE1/2-11,RE1/2-12 D	RE1/3-11,RE1/3-12 D
7	RE2/2-16,RE2/3-16 A	RE1/2-13,RE1/2-14 A	RE1/3-13,RE1/3-14 A
8	RE2/2-16,RE2/3-16 D	RE1/2-13,RE1/2-14 D	RE1/3-13,RE1/3-14 D
9	RE2/2-17,RE2/3-17 A	RE1/2-15,RE1/2-16 A	RE1/3-15,RE1/3-16 A
10	RE2/2-17,RE2/3-17 D	RE1/2-15,RE1/2-16 D	RE1/3-15,RE1/3-16 D
11	RE2/2-18,RE2/3-18 A	RE1/2-17,RE1/2-18 A	RE1/3-17,RE1/3-18 A
12	RE2/2-18,RE2/3-18 D	RE1/2-17,RE1/2-18 D	RE1/3-17,RE1/3-18 D

Table 3.4: Scheme for YE+1-X4 far side.

is 10 μA. The channel trips with in 1 sec (the trip time) when the current in a cable exceeds this limit. Such a cable must be marked and then repaired (Jupiter connectors at HV control room or tri-polar connectors at the patch panel). The value of the current drawn at different voltage say 10, 12 and 15 kilovolts is noted down after a regular intervals of time. The Figure 3.10 shows the high voltage cable testing results.

3.2.4 Low Voltage System

The Low voltage System of the RPCs is used to provide power to FEBs in chambers and to LBBs in the LV-Racks. The FEBs are first in the readout chain to get the signal. Then this signal is sent to Link Boards (LBs) located in the galleries at the sides of the CMS detector. The LBs are housed inside Link Board Boxes (LBBs). The LBs send data to control room via optical fibers. The hardware used for setting up a low voltage system for positive side contains 1- Universal Power Supply SY 1527. 2- Branch controllers A1676N. 6- AC to DC Converters A3486S. 6- EASY Crates (Embedded Assembly System)3000S 18- Low Voltage Modules A3009N. Hardware used for HV system is shown in Table 3.3. The universal Power Supply SY1527, Easy Crates A3000 and Branch Controller A1676N is same for both high voltage and Low voltage System. The LV module has 12 output channels

which can be used to supply analog or digital low voltage to FEB or LBB.One channel of LV module is used to supply analog or digital to two chambers. So each module powers up 12 chambers. FEBs collects the signal from read out strips on RPC detector. Each RPC has 96 charge collecting strips. Each chamber has three FEBs corresponding to 3 eta partition of a strips. Each FEB would receive a data of 32 strips. The data received by FEBs is then sent to Link boards LBs. There are 3 FEBs which corresponds to 6 readout cables going to Link boards. The link board can handle the data of 6 chamber. So the total number of link boards required for each disk is 12 since there are 72 chambers on each disk. The LV system for disk 1 and disk 2 is located at the level X2 and X4 while for disk 3 it is located at X3. Each LV rack has one AC-DC converter (MAO). The Table 3.4 show the low voltage cabling scheme for YE+1 at level X4. There is a DCS (Detector Control System) cable at each level to read/write threshold on FEBs. Five phase power cable is used to power up the AC-DC (MAO) converter. This AC-DC converter also provides the 48V power cable to power up the EASY crates which houses Low Voltage modules. Each easy crate is controlled form the mainframe via branch controller. The tower which is near to the control room named as Near side and the other is named as Far Side.

3.2.5 Threshold Scanned Connectivity Test

The current limit for LV Analog is set to 2 A and 3 A for digital to keep the drawn current in the safe limit. The operating voltage for analog and digital channel is 7 and 7.5 volts respectively. The software used to set the threshold of FEBs is known as XDAQ. It also reads output signal from FEB via LBBs. First we test if all FEBs are connected properly. This is performed by 'Connectivity' Test. In this test we set FEB threshold to 40 mV for one eta partition. The default threshold for taking the data is 210 - 230 mV. So 40 mV being very low we should get hits on all strips of partition say A. If we set threshold of A to 400 mV, which is very high, then no strip on this partition should show any hit. When threshold is set to 40 mV and a strip shows no hit then this strip is called a dead strip. When threshold is set to 400 mV and some strip still shows hits then it is called a noisy strip.

According to CMS criterion total number of dead and/or noisy strips should not exceed 3. Each FEB is tested in this way. Dead and noisy strip are also noticed. Exchange of signal cables is also noted with this test and fixed when access is available to chambers.

3.2.6 Gas System

Resistive plate chambers are gaseous detectors. The performance of RPCs depends largely on the gas which is being used. RPCs have a gas volume of 10 m^3 for the barrel region and about 8 m^3 for the both positive and negative endcap. The gas mixture consists of Freon 95.9%, Iso-butane 3.8% and SF_6 0.3%. A very small percentage of SF6 is added. Because of its high density about 6.14 kg/m^3 and molecular weight it is used as a quenching agent to reduce the avalanche in the detector. The basic function of gas system is to mix the three components of gas together in the appropriate proportions and to distribute clean gas mixture into the individual chambers at a pressure between 1 and 3 mbar above the atmospheric pressure. Pressure, temperature and gas flow rate control the overall working of RPCs. Every disk has two pressure sensors installed; one at the top of the disk and other at the X3 level of near side opposite to the gas distribution rack. The gas is flushed in the chambers in the closed loop configuration during commissioning with a fresh replenishing rate of nearly 15 %. Total flow rate is 4 m^3 (half volume change/hour). The volume of RE*/2 chamber is 5.6 L and of RE*/3 is 7.5 Liters. There are 72 chambers on each disk. Six gaps are joined together to form one gas sector all 6 being the top or all 6 being the bottom gaps. For RE+1 gaps of 6 consecutive RE */3 or RE */2 are joined to make one gas sector. Thus gas sector for RE+1 is of 60^o while for RE+2 and RE+3 it's of 30^o. In RE+2 and RE+3, the 6 gaps from layer 2 and layer 3 are joined together. There are 6 gas bulkheads located at regular interval around the disk. These bulkheads have two inputs and two outputs for supply/return of gas to/from chambers. Overall there are 12 inputs and 12 outputs channels for gas system which are connected to gas racks at X2 level.

3.2.7 Cooling System

There are three FEBs attached to a single chamber. To avoid heating of the FEBs, a cooling system is installed on the chamber. On the outer face of the chamber copper plats are mounted under each electronic board. Water circulates in these pipes, takes the heat from the FEBs. In RE1 6 chambers from same layer are joined together to form one cooling sector. Thus in RE1 the cooling sector is of 60 degrees while for RE2 and RE3 it's of 20 degrees. In RE2 and RE3, 4 adjacent chambers (2 from RE */2 and 2 from RE */3) are joined to make one cooling sector. The good performance of FEB depends on good cooling system. A heated FEB can give unreliable values for threshold hence of signal at readout.

3.2.8 The Detector Control System (DCS)

The role of the RPC Detector Control System is to monitor the detector conditions and performance and control all subsystems related to RPC and their electronics, and store all the information in a dedicated database, called the Condition DB.

The LHC experiments are build for long period running for approximately more then 10 years. Therefore some Detector Control System (DCS) is required for correct and safe operation of all sub-detectors of CMS [34]. The DCS system is also used to detect harmful and abnormal situations of sub-detectors and to prevent them by taking automatic actions to minimize the damage. The DCS of RPC is divided into sub-systems according to their hardware requirement like: High Voltage, Low Voltage, gas and cooling system and some environmental sensors (temperature, pressure and humidity). The DCS system of RPCs is developed using commercial ETM Supervisory Control And Data Acquisition (SCADA) software, PVSS 3.6 and the Joint Control Project (JCOP) framework components.

The CMS consist of many type of sub-detectors like CSC, DT, Tracker ,e.g. It is recommended to use some uniform, user friendly states and the commands for all sub-detectors. The states for some sub-detector are ON, OFF, STANDBY and ERROR and the commands are ON, OFF and STANDBY. These particular states and commands are used to ensures uniformity and compatibility with the central CMS DCS, permitting adequate transitions between the states. The use of

these particular states and commands ensures compatibility and uniformity with the central CMS DCS, permitting adequate transitions between the states. The small number and general definitions of DCS states makes them suitable for all sub-detectors.

The Graphical User Interface (GUI): The GUI is developed to control and monitor the detector, which is easy to use also by non-experts and able to preserve the system from any dangerous action. The GUI allows a complete control of the entire RPC system and therefore, the different access levels have been set to prevent the system from human error. The alarm handling is an indispensable feature of any control system. An alarm is issued every time the system unusually leaves the desired state or if a given parameter deviates from its set limit. A sets of alarm conditions, access levels, and recovery procedures have been defined and implemented for all the critical hardware parameters.

3.3 Problems and solutions from commissioning

Problems faced during the commissioning of different services installed on RPCs are listed below.

HV system: There was tripping problem and current spikes in some HV channels which were cured once the bad connectors were removed. Some HV channels showed continuous slow rise in current during working hours. This problem was fixed by adjusting the values of temperature and humidity in the experimental cavern. The flow rate of gas also contributed to this problem. Increased flow rate reduced the rising current problem.

LV system: There were communication problem between the EASY crates and MAO, tripping and over current problem. Communication was fixed by tightening connection of cables used for communication. The LV to the channels with over current and tripping problems was turned off. Few LV distribution boxes malfunctioned. Due to accessibility only two of those boxes were successfully replaced.

Gas system: Each endcap disk was tested for gas leaks. The blockage observed in flow was removed by increasing flow rate. Some of the gas channel were swapped. This problem was fixed by correcting the labels on the gas connections. Gas leaks

were fixed by properly tightening the connections. Another problem was flow cell calibration. For which no solution was applied during commissioning.

Coolant system: Leaks were found at some joints. The joints were tightened and fixed where required and possible.

Readout system: Some signal cable swapping problem was found. Swapping was fixed where possible. For some FEB threshold could not be changed by software. This was fixed by applying a default setting from hardware. Link board failure was removed by changing link boards

Detector Control System(DCS): The software was modified completely to display read and control endcap according to endcap geometry

3.4 Efficiency of Endcap RPCs

During LHC Run I, the hardware was working properly. All hardware subsystem performed according to CMS criteria in separate and combined testing. RPC parameters were also observed to be in the range as given in Section 3.1.3. RPC performed well during CMS data taking period in 2010 and 2011. Efficiency of endcap RPCs during 2010 and 2011 is shown in Figures 3.11, which is more the 94% in both years.

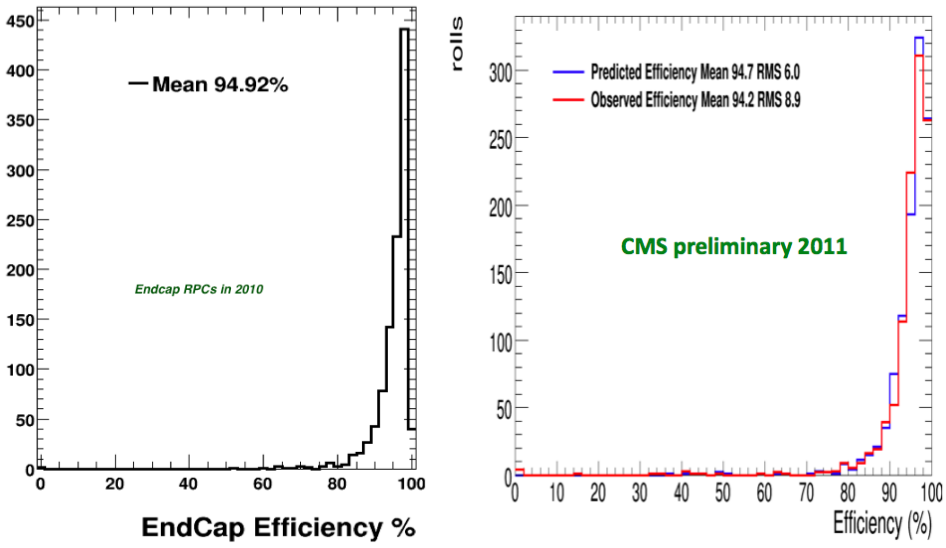

Figure 3.11: Efficiency plot for Endcap RPCs for period 2010 and 2011

Chapter 4

Reconstruction and Selection of χ_C Candidate

4.1 Introduction

Heavy quarkonia, bound states of charm and bottom quark-antiquark pairs, play an important role in the detailed understanding of quantum-chromodynamics (QCD), the theory describing the strong interactions among elementary particles. Given their high mass, heavy-quarkonium states are non-relativistic. They allow the application of theoretical tools in a non-relativistic regime that simplify and constrain the analyses of non-perturbative effects. Thus providing a unique laboratory to explore the interplay between perturbative and non-perturbative effects in QCD [36]. During the last decade, significant progress resulted from intense work on the mechanisms of heavy quarkonium production, from both the experimental and the theoretical sides. Nevertheless, a definitive understanding of the mechanisms of quarkonium production remains a challenge, with several models competing for confirmation.

The J/ψ production cross section measurement at Tevatron [37, 38] was found in disagreement with color singlet models [39], and soon after the same experiment reported a value of the χ_{c2} and χ_{c1} production ratio which deviates significantly from the value of 5/3 obtained from simple spin counting [40]. It is particularly interesting to reproduce the cross section ratio measurement at LHC, since its value is not expected to suffer from large experimental uncertainties apart from

statistical fluctuations and can be compared to relatively simple theoretical calculations. This comparison can be used to validate, for example, the Color Singlet calculation rather than the NLO NRQCD calculation [41, 42]. The calculation of the ratio is not affected by theoretical and experimental uncertainties such as the quark masses or the value of α_s which cancel out. The understanding of the χ_c meson production cross section is also important for the study of the J/ψ and in particular of its polarization. Infact the feed-down contribution of the χ_c to prompt J/ψ production cannot be distinguished from directly produced J/ψ.

There are two mechanisms by which χ_c can be produced in a hadron collider; one is known as prompt production while other is called non-prompt production of χ_c. In prompt production, partons from protons directly interact to produce a χ_c while in non-prompt b-hadrons are formed by partons which further decay into χ_c. Since b-hadrons decay away from primary vertex, non-prompt χ_c can be distinguished from prompt by using the secondary vertex.

In this analysis χ_c is reconstructed using their radiative decays to J/ψ which is accompanied by a photon. Reconstruction of χ_c using their daughters is explained in this chapter. Selection criteria for each particle is also given in following sections. Section 1 and 2 respectively give details of data samples and triggers used for this analysis. Section 3 and 4 gives selection criteria for muons and J/ψ (reconstructed using di- muon channel). In section 5 the criteria for electron pair and converted photons is given. Finally section 7 explains reconstruction of χ_c candidates.

During working in the group, I went through all analysis steps. Data processing was one of the major task for our analysis. I took all the responsibility of data processing of 2011 available data for the tuning of different parameters for more precise results. I have also been involved in the fitting of the mass plots for signal and background functions and presented the status of each step. In the same time I have also contributed in the improvement and modification of some plots which we have presented in our final results. I have also worked in calculating systematics uncertainties coming from mass fit and χ_{c1} and χ_{c2}.

4.2 Data Samples

In 2011 LHC delivered nearly 6.01 $fb^{-1}$of pp collision data at 7 TeV centre of mass energy to CMS out of which 5.56 fb^{-1} was collected. LHC increased it's instantaneous luminosity from $5 \times 10^{32} - 5 \times 10^{33}$ resulting in more than one interaction per bunch crossing. Extra interactions are called pileup, identified in data by number of primary vertices in each event. At the start of 2011 mean number of primary vertices were about 1. At the end of 2011 this number increased to 6 primary vertices per interaction.

The data of 2011 is divided in two periods; 2011A and 2011B. The second one is characterized by higher instantaneous luminosity and larger number of interactions per bunch crossing. The dependence of our results on pileup will be discussed in a separate section. The details of the data sample are reported in Table 4.1. We used CMSSW version `CMSSW_4_2_3`, with conditions global tag `FT_R_42_V13A`. Measurement is done using the MuOnia data samples. These samples are based on data recorded with the CMS detector by using the B-Physics HLT dimuon resonant and non-resonant triggers.

Data samples	Run Range
`/MuOnia/Run2011A-May10ReReco-v1/AOD`	160404-163869
`/MuOnia/Run2011A-PromptReco-v4/AOD`	165071-168437
`/MuOnia/Run2011A-PromptReco-v5/AOD`	170053-172619
`/MuOnia/Run2011A-PromptReco-v6/AOD`	172620-175770
`/MuOnia/Run2011B-PromptReco-v1/AOD`	175832-180252
Monte Carlo simulation samples `/JPsiToMuMu_2MuPEtaFilter_7TeV-pythia6-evtgen/Summer11-PU_S4_START42_V11-v2/`	

Table 4.1: Official CMS Data samples used for the analysis.

4.3 Triggers for χ_c analysis

In general, all B-Physics triggers are based on a selection of opposite sign muon pairs. Additionally for each trigger there is a cut on the transverse momentum p_T, rapidity $|y_{J/\psi}|$, invariant mass J/ψ, displacement of the muon pair from the

primary vertex etc. Figure 4.1 shows the contributions of several B-Physics triggers to the dimuon mass distribution obtained from MuOnia data sample. The steps in Figure 4.1 indicate usage of different triggers. Due to increase in instantaneous

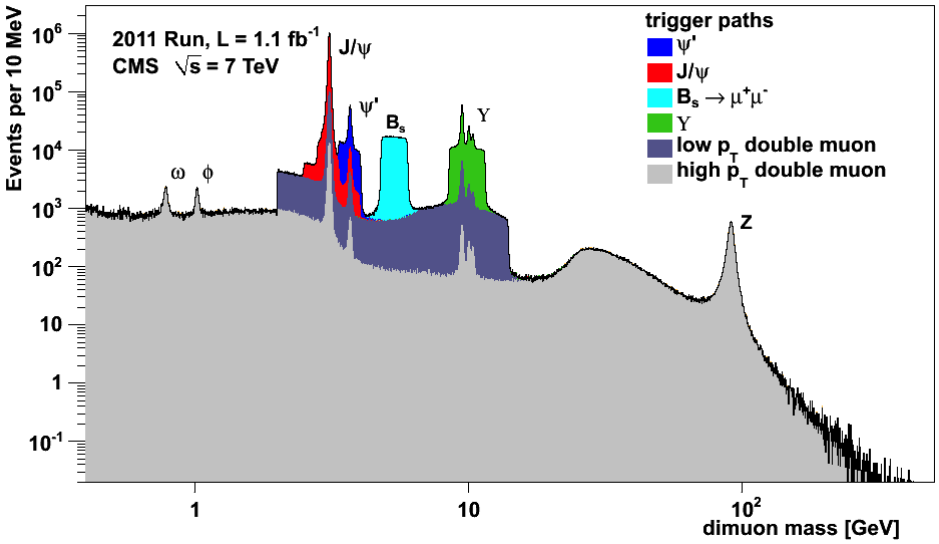

Figure 4.1: Di-muon mass distribution obtained from overlapping several trigger paths

luminosity, trigger conditions changed rapidly to accommodate increasing number of collisions. The threshold on transverse momentum of trigger objects increased gradually as seen in Table 4.2. The Table also gives the list of trigger paths used in this analysis.

The HLT trigger paths in Table 4.2 are characterized by two opposite charge muons, dimuon rapidity $|y| < 1.25$, momentum threshold for the pair that increases from 6.5 to 10 GeV, vertex χ^2 probability more than 0.005 and dimuon mass from 2.95 to 3.25 GeV/c_2. In Table 4.2 the instantaneous luminosities, L, are reported for each trigger path as well as their time integrated luminosity.

4.4 Reconstruction of Muons

Muons are charged particles which can be detected in the tracker and muon system of CMS detector. Based on where they are detected, muons can be divided in three categories.

- Stand-alone muons

Run Range	Trigger Path	Lumi [pb^{-1}]
163269-163869	HLT_Dimuon6p5_Barrel_Jpsi_v1	165.11
165088-166043	HLT_Dimuon7_Jpsi_X_Barrel_v1	722.94
166346-166346	HLT_Dimuon7_Jpsi_X_Barrel_v2	4.42
167078-167913	HLT_Dimuon7_Jpsi_X_Barrel_v3	244.54
170722-173198	HLT_Dimuon7_Jpsi_X_Barrel_v5	872.94
173236-178380	HLT_Dimuon10_Jpsi_Barrel_v6	1918.00
178420-179889	HLT_Dimuon10_Jpsi_Barrel_v9	600.28
180072-180252	HLT_Dimuon10_Jpsi_Barrel_v10	94.34

Table 4.2: HLT trigger paths used in this analysis

- Tracker muons
- Global muons

The reconstruction is performed by algorithms which are based on detector geometry. The information of these muons is stored in a dedicated collection for each event.

4.4.1 Standalone Muons

Stand-alone muons are built using only the information from the muon system. The reconstruction starts by finding hit positions in DT, CSC and RPC. Then, hits within each of the DT and CSC chambers are matched to form seeds. The seeds are the starting point for trajectory building of muons. The track finding and fitting procedure based on a combinatorial Kalman filter [43] explores the next DT, CSC and RPC layers, adjacent to the layers where the seeds are formed, to build the muon trajectory.

4.4.2 Tracker Muons

Reconstruction of the Tracker muons starts from the tracker by considering all tracks above a certain minimum $p_T$which are later matched with at least one muon segment in the muon chambers. Muons are identified by their deposited energy in the electromagnetic calorimeter. The requirement is that the energy deposited in ECAL is compatible with a minimum ionizing particle. This approach of muon

reconstruction works well for muons with $p_T$below 6 GeV/c when they can not reach the outer muon chambers. Tracker muons have a minimum momentum of 2.5 GeV/c.

4.4.3 Global Muons

Global muons are a combination of stand-alone muons and tracks in the silicon pixel and strip tracker. The muon track reconstructed in the muon chambers is matched with a track reconstructed in the tracker. Global muons have a minimum momentum of 3 GeV/c. The tracker and the muon systems play different roles in the muon reconstruction depending on its momentum scale. The tracker has high momentum resolution, about 1 - 2% for 100 GeV/c particles and it is not much affected by multiple scattering and energy loss.

The magnetic field in the tracker is homogeneous and almost constant. Therefore the tracker has very high efficiency in low p_T muon reconstruction. Moreover, the low p_T muons can not reach the muon stations because they lose energy in the material and bend in the magnetic field before reaching the muon system. On the other hand, the muon systems can reconstruct higher momentum muons because they can measure curvatures with a lever arm of 4-7 m from the beam line as opposed to 1 m in the tracker (the higher the momentum of the muons is the less curved is its trajectory).

Knowing the trajectory's curvature of the muon, the tangent to the trajectory as well as the magnetic field one can find a relation between the momentum of the muon and its motion in magnetic field using Lorentz force. Low p_T muons trajectory is a helix, while high p_T muons trajectory is nearly a straight line. High p_T muons can emit photons leading to electromagnetic showers in the muon systems. This can cause a loss of efficiency in the reconstruction of high p_T muons.

In this analysis, we use two types of muons: reconstructed inside-out (Tracker muons) and reconstructed outside-in (Global muons). We apply additional selection cuts on the muon candidates as reconstructed with CMS standard algorithms to reject tracks that are not coming from muons. These cuts reject muon candidates, which may come from decays in flight from kaons and pions or cosmic

muons. Table 4.3 shows the list of selection requirements for tracks [44]:

Track selection	
At least 11 hits in the tracker no less than 2 hits in the pixel	removes decays in flight from kaons and pions
$\|d_0\| < 4$ cm and $\|z_0\| < 35$ cm with respect to the primary vertex track $p_T > 3.3$ GeV/c and $\|\eta\| < 1.3$	to reject decays in flight and cosmic muons

Table 4.3: Track selection criteria for Muons.

- Two types of muons are used: "TrackerMuonOneStationTight" and "TrackerMuonArbitrated". For the first type, the silicon track is matched to two segments in the muon chambers. For the second type, an arbitration process is used to assign segments in the muon chambers uniquely to the muon tracks.

- Fit to the trajectory of Tracker muon in the Tracker is required to have $\chi^2/\text{ndf} < 4.0$ to suppress muons from decays in flight.

- Fit to the trajectory of Global muon is required to have $\chi^2/\text{ndf} < 1.8$ in the tracker and $\chi^2/\text{ndf} < 20.0$ in the muon systems to suppress muons from decays in flight. The Muon selection cuts are summarized in Table 4.4.

Muon Track selection	
track fit χ^2/ndof	<1.8
hits in Pixel	≥ 2
hits in Tracker	≥ 11
Fiducial cylinder	$4cm(r) \times 35cm(z)$
$\mu\mu$ vertex fit probability	>0.01
$p_T(\mu)$, $\|\eta\| < 1.3$	3.3 GeV/c
$p(\mu)$, $1.3 < \|\eta\| < 2.2$	2.9 GeV/c
Muon id	TrackerMuonOneStationTight

Table 4.4: Muons selection cuts

4.5 Dimuon (J/ψ) Candidates

There are three possibilities to get a J/ψ using pair of Global and Tracker muons i.e. Global-Global, Global-Tracker and Tracker-Tracker. After pairing the two oppositely charge muons, their tracks are fitted with a common vertex constraint. Muon candidate tracks are required to have $p_T > 3.3$ GeV/c, $|\eta| \leq 1.3$ and match a well-reconstructed segment in at least one muon detector. The vertex fit χ^2 probability is required to be larger than 1%. If more than one muon pairs is found in the event, the pair with largest vertex χ^2 probability is retained. The dimuon mass is constrained to the J/ψ mass range of 3.0 and 3.2 GeV/c^2 and the rapidity of the muon pair is constrained to barrel range of -1 to 1. The J/ψ is constrained to barrel region because of photons. Photons follow path not very far from J/ψ and can be poorly reconstructed in the forward region of the tracker. Invariant mass spectrum of the muon pair after above selection criteria is shown in Figure 4.2. The J/ψ and ψ' peaks are clearly visible. The steps in the plot correspond to the usage of different dimuon triggers. Figure 4.1 and the selection cuts summarized in Table 4.5.

J/ψ **selection**	
$\mu^+\mu^-$ vertex fit probability	>0.01
$m_{\mu^+\mu^-}$	3.0 - 3.2 GeV/c^2
$\|y(\mu^+\mu^-)\|$	< 1

Table 4.5: J/ψ selection cuts

4.6 Converted Photon

To reconstruct the photon from radiative decays, we use the tracker-based conversion reconstruction described in [45, 46, 47]. Photon conversions are characterized by an electron positron pair originating from a common vertex. The e^+e^- invariant mass must be consistent with zero within its uncertainties and the two tracks are required to be parallel at the conversion point. The reconstruction of e^+e^- pair and photon is explained in detail here.

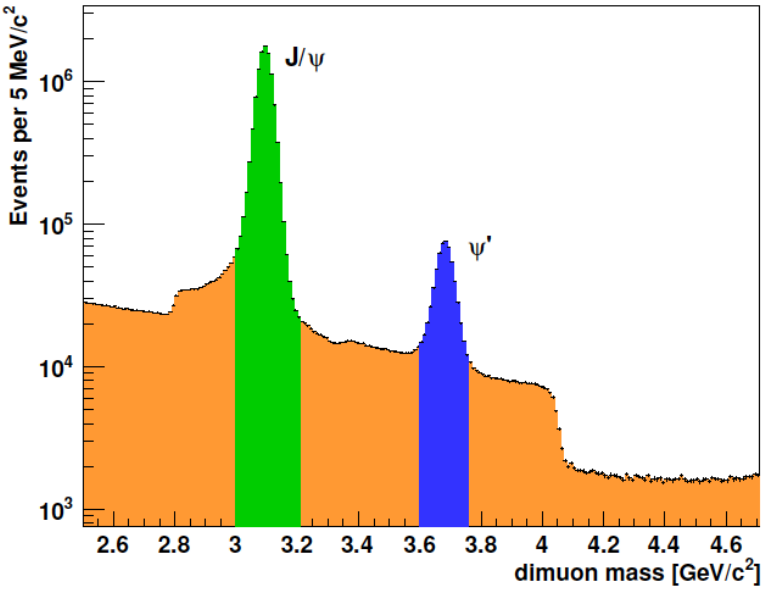

Figure 4.2: Invariant Mass of $\mu^+\mu^-$

4.6.1 Electron Positron Pair

Track reconstruction starts with seeds in the tracker (either pixel or strip tracker). These seeds are hits in different layer with electronic signal crossing a certain threshold. Starting from seed the track is reconstructed by adding hits in the adjacent tracker layers. Whenever a new hit is added in the track, track parameters and uncertainties are recalculated by using Kalman Filter [43] or Gaussian Sum Filter methods. This process continues until last tracker layer is reached. Tracking is performed in several iterations. Hits which are already associated to a track in one iteration are removed from next iteration. At the end of each iteration, tracks not compatible with primary vertex and having bad fit probability are removed. These tracks are termed as fake tracks. A list of track parameters is given in Table 4.6. To reconstruct e^+e^-, there must be at least four hits in the track and the χ^2/ndf should be less than 10. Making requirement tighter can reduce efficiency of converted photons.

4.6.2 Reconstruction of Converted Photon

In order to reconstruct converted photon following conditions are required to be fulfilled by the pair of track.

track normalized fit χ^2
number of hits used for building track trajectory
number of tracker layers with a hit on the track trajectory
number of layers with missing hits between the first and the last hit on the track trajectory
transverse momentum $p_T$of the track
transverse impact parameter d0 with respect to the mean pp collision
significance of the transverse impact parameter d_0/σ_{d_0}
longitudinal impact parameter z0 with respect to the primary vertex
significance of the longitudinal impact parameter z_0/σ_{z_0}

Table 4.6: Track parameters for converted photons

- Charge of the two tracks should be opposite.
- The charge-signed impact parameter $q \cdot d_0$ must be positive, $q \cdot d_0 > 0$, where q is the track's charge and d_0 is transverse impact parameter. This means conversion vertex lies outside electron and positron helices.
- Helices transform into circles when projected onto the transverse plane. The distance of minimum approach in the transverse plane, dm, between two points of tangent approach of the two tracks helices must be between -0.25 and 1 cm. Figure 4.3 shows the meaning of the parameter dm, defined as $d_{O1-O2} - (R_1 - R_2)$), where d_{O1-O2} is the distance between the centers of the two tracks circles and R_1 and R_2 are the two circles radii. The parameter dm is negative when the two tracks circles are intersecting. The upper cut on dm is used to reject tracks that bend around in the magnetic field and travel backward also known as "loopers". The "loopers" have a spiral trajectory and they lose energy with every turn.
- The difference in z, Δz, of the innermost hits in a track pair must be less than 5 cm.
- To reduce fake tracks due to looper, pair of tracks must have one of the two innermost hits in the same tracker layer.

- To reduce fake converted photons, transverse momentum, p_T , of the converted photon is constrained to be greater 0.5 GeV/c.

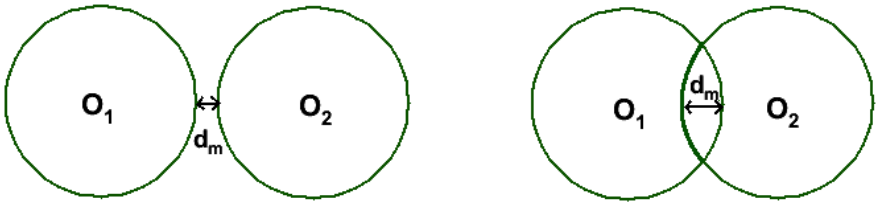

Figure 4.3: Positive and a negative distance of minimum approach d_m between two ideal track circles

Track of both electron and positron are fitted with a common 3d-constrained kinematic vertex fitter. This constraint keeps tracks which are parallel in both the transverse and longitudinal planes. The pair is rejected if the fit does not converge or its χ^2 probability is less than 5×10^{-4}. Few additional cuts are given below and summarized in Table 4.7:

- The conversion vertex should be at a transverse distance larger than 1.5 cm from the center of the beam pipe (radius of the beam pipe is $\sim$ 3 cm). Fake track pairs coming from the primary vertex are reduced by this cut.

- Each conversion track candidate must be compatible in z with at least one reconstructed primary vertex. This is ensured by requiring that the longitudinal impact parameter z_0 of the conversion track with respect to the primary vertex satisfies $|z_0/\sigma_{z_0}| < 5$. The primary vertices in pp-collisions are centrally reconstructed with special CMS algorithms from selected tracks for each event. Additionally, we require that the number of the tracks from the primary vertices is at least 4, corresponding to the muons and electrons tracks. Among the two primary vertices closest in z to each of the e^+, e^- tracks, at least one must be common to the two tracks.

- A reconstructed primary vertex from proton-proton collision is assigned to the reconstructed conversion by projecting the photon momentum along the beamline and by choosing the closest vertex along the z direction. If the distance along the z between the vertex and the projected photon momentum,

Δz, is larger than five times its uncertainty ($|\Delta z/\sigma_{\Delta z}| < 5$) the candidate is rejected.

Photon conversion selection	
Electron track hits	≥ 4
Electron track fit χ^2/ndof	< 10
Distance of approach	-0.25cm $< d_m <$ 1cm
Signed impact parameter	$q \cdot d_0 > 0$
e^+e^- vertex fit probability	$> 5 \times 10^{-4}$
Radius of conversion	$R_{conv} > 1.5$ cm
$p_T(\gamma)$	> 0.5GeV/c

Table 4.7: Selection cuts for converted photons

4.6.3 π^0 Rejection

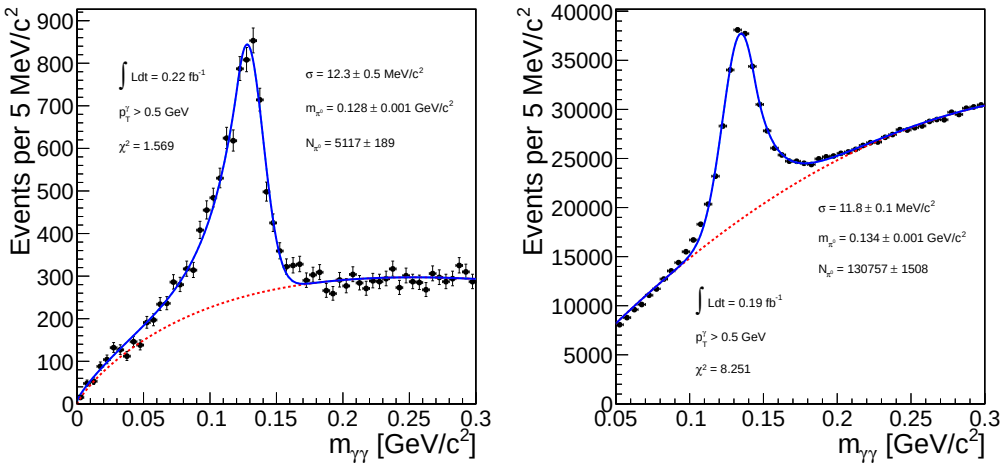

Figure 4.4: Left: invariant mass distribution for pairs of converted photons. Right: invariant mass distribution of a converted photon with a calorimetric (Particle Flow) photon.

Finally each conversion candidate is associated to every other conversion candidate in the event, and to any Particle-Flow reconstructed photon. The resulting invariant mass distribution is shown in Figure 4.4 where the π^0 peak is clearly visible. Any conversion with a pair having invariant mass in the range between 0.11 and 0.15 GeV/c^2 is rejected, since it assumed to be compatible with a π^0

decay photon. The cut correspond to a 2σ window around the observed resonance peak. We have verified that the π^0 rejection cut, while effectively reducing the background, does not affect our result. Converted photon candidates are required to have $p_T > 0.5$ GeV/c, while no requirement is imposed on the η of the photon (which in facts does not fly far from the J/ψ candidate).

4.6.4 Conversion Radius

The distribution of χ_c candidates photon conversion radius is shown in Figure 4.5. It reflects the tracker material distribution convoluted with the χ_c production flux and the reconstruction efficiency as well. The first three peaks where most of the statistic is accumulated, correspond to the beam pipe, merged with the peak of the first pixel barrel layer, and the two outermost pixel barrel layers. For radii larger than about 20 cm the buildups due to the four innermost silicon strip layers are visible. The observed distribution of the photon conversion radius is consistent with the known distribution of material in the tracking volume and with Monte Carlo simulations [47].

4.7 χ_c Selection

As χ_c is reconstructed using converted photons and J/ψ , the primary vertex associated to the conversion should be compatible with the reconstructed J/ψ vertex. This requirement is fulfilled when the three-dimensional distance between the two vertices, D, satisfies $|D/\sigma_D| < 5$. To make sure we get prompt χ_c for analysis, the J/ψ, should also be produced promptly in pp-collisions. The J/ψ coming from a b-hadrons is displaced from the primary vertex [48]. The 3D decay length of b-hadrons or the distance between the primary vertex and the b-hadron decay vertex is

$$L = \beta\gamma ct \tag{4.1}$$

where c is the speed of light, t is the proper lifetime of the b-hadron, $\beta = v/c$ where v is the speed of the b-hadron and γ is the Lorentz boost defined as $1/\sqrt{(1-\beta^2)}$. The transverse decay length of b-hadrons in x-y plane of the detector is

$$L_{xy} = \beta_T\gamma ct \tag{4.2}$$

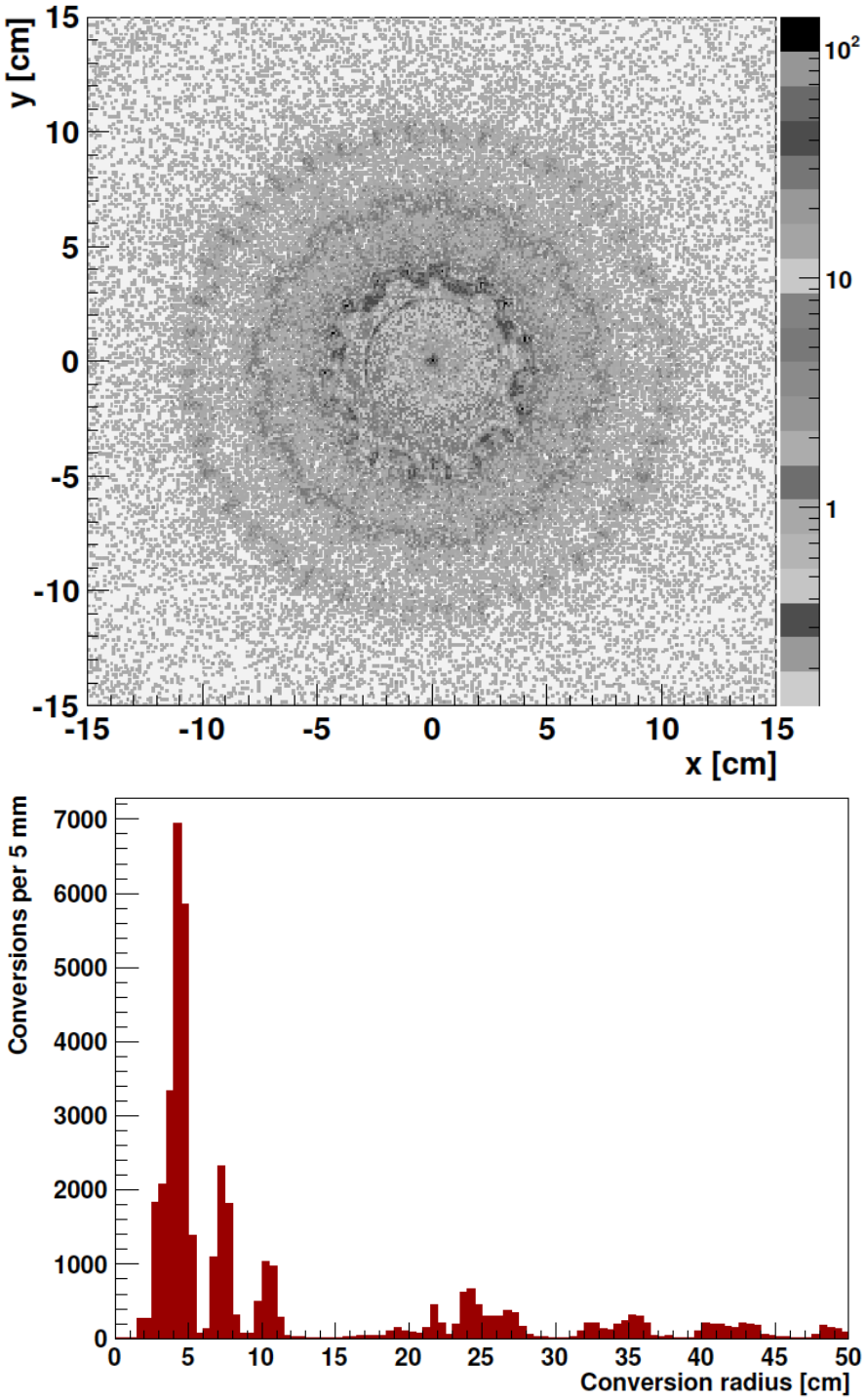

Figure 4.5: x-y distribution in the pixel detector region (above) Conversion Radius (below)

and it can be used to separate the J/ψ produced in b decays from prompt J/ψ. For events with J/ψ p_T greater than 1.25 GeV/c, the J/ψ flight direction aligns well with that of the b-hadron. Therefore L_{xy} can be written as

$$L_{xy} = \overrightarrow{L} \cdot \frac{\overrightarrow{p}_T(J/\psi)}{|p_T(J/\psi)|} \tag{4.3}$$

where $\overrightarrow{L}$ is the vector from the primary vertex to the J/ψ decay vertex in the $r-\phi$ plane and $\overrightarrow{p}_T$ is the transverse momentum vector in x-y plane.

4.7.1 Extraction of Prompt Component

To distinguish between prompt and non-prompt contribution of J/ψ, a variable called pseudo-proper decay length, $l_{J/\psi}$ is used. This decay length is derived from Equations 4.2 and 4.3 by using $\beta_T\gamma = p_T(J/\psi)/m_{J/\psi}$

$$l_{J/\psi} = ct = \frac{L_{xy}}{\beta_T\gamma} = L_{xy} \cdot \frac{m_{J/\psi}}{p_T(J/\psi)} \tag{4.4}$$

where $m_{J/\psi}$ is the mass of the J/ψ and L_{xy} is measured by using Equation 4.3 For prompt J/ψ pseudo-proper decay length is zero while for non-prompt J/ψ there is an exponentially decaying pseudo-proper decay length distribution.

In an ideal detector, the $l_{J/\psi}$ should be zero for the prompt events. Therefore for the prompt component we use a resolution function which is taken to be a double Gaussian Probability Distribution Function (PDF). The J/ψ shape of the non-prompt component is given by convolving the same resolution function with an exponential decay function of a b-hadron. Figure 4.6 illustrates the fit to the pseudo-proper decay length of the J/ψ. We calculated the fraction of the non-prompt component of the J/ψ in the region $l_{J/\psi} < 30\mu m$ to be around 8%. This has been done by counting the number of non-prompt J/ψ events with respect to the number of prompt J/ψ events in the region $l_{J/\psi} < 30\mu m$. A contamination from background was not taken into account. The selection cuts used to define the χ_c candidates are summarized in Table 4.8

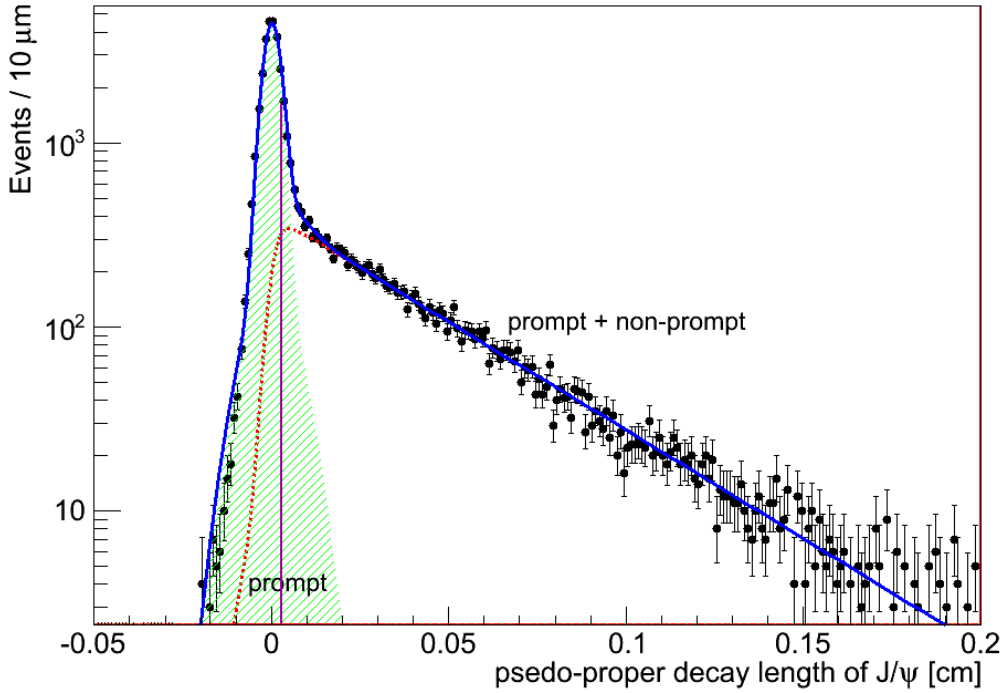

Figure 4.6: Pseudo-proper decay length for separation of prompt and non-prompt component of J/ψ

χ_c **selection**	
π^0 rejection	$m_{\gamma\gamma} < 0.11$ GeVc^2 and $m_{\gamma\gamma} > 0.15$ GeVc^2
Photon - J/ψ vertex compatibility	5σ
Prompt component selection	$L_{J\psi} < 30$ μm

Table 4.8: Summary of the cuts used to select χ_c candidates

Chapter 5

Cross Section ratio measurement of χ_{c1} and χ_{c2}

5.1 Analysis Procedure

We select χ_{c1} and χ_{c2} candidates by searching for their radiative decays into the $J/\psi + \gamma$ final state, with the J/ψ decaying into two muons. The χ_{c0} has too small a branching fraction into this final state to perform a useful measurement, but we consider it in the modeling of the signal line shape. An accurate reconstruction of the photon is then needed to finalize the reconstruction of the χ_c with sufficient resolution. In the center of mass of the charmonium states, the photon has an energy of 390 MeV when emitted by the χ_{c1} and of 430 MeV when emitted by the χ_{c2}, which results in a p_T of the photon to be measured mostly between 0.5 and 6 GeV/c in the laboratory frame. A calorimetric measurement of the photon energy would not provide sufficient resolution to disentangle the two states, whose masses differ by only 45 MeV . On the contrary, a measurement of the momentum of the electron-positron pair originating from a conversion of the photon, in the beam pipe or in the inner layers of the Tracker, results in a very accurate measurement of the photon energy. The drawback is the reduced yield due to the small probability for a conversion to occur in the innermost part of the tracker detector and mostly to the low reconstruction efficiency.

For each χ_{c1} and χ_{c2} candidate, we evaluate the mass difference $\Delta m = m_{\mu\mu\gamma} - m_{\mu\mu}$ between the dimuon-plus-photon invariant mass $m_{\mu\mu\gamma}$ and the dimuon invariant mass $m_{\mu\mu}$. We use the quantity $Q = \Delta m + m_{J/\psi}$, where $m_{J/\psi}$ is the

world-average mass of the J/ψ [49], as a convenient variable for plotting the invariant-mass distribution.

In experimental particle physics the mathematical expression for the measurement of the production cross section of particle is given in equation 5.1.

$$\sigma = \frac{N_{obs} - N_{bkg}}{\mathscr{L}_{int} \cdot \epsilon \cdot A_{cc} \cdot \mathscr{B}} \tag{5.1}$$

Where σ is cross section, N_{obs} and N_{bkg} are the total number of observed events and number of background events respectively, $\mathscr{L}_{int}$ is integrated luminosity, ϵ is the reconstruction efficiency, A_{cc} is acceptance of the detector and $\mathscr{B}$ represents the branching ratio of the decay.

In this analysis we present our measurement of cross section ratio of χ_{c2} over χ_{c1}. When we measure the ratio, most of the theoretical and experimental uncertainties are canceled out, including the quark masses, value of the strong coupling constant α_s, trigger efficiencies, integrated luminosity and in some cases reconstruction efficiency. Therefore, this ratio can be regarded as an important reference measurement to test the validity of various theoretical quarkonium production models.

The ratio R_p of the production cross section of χ_{c2} to χ_{c1} is measured as a function of J/ψ transverse momentum from 7-25 GeV/c. The R_p can be calculated by the equation 5.2.

$$R_p(p_T(J/\psi)) = \frac{\sigma(pp \to \chi_{c2} + X)\mathscr{B}(\chi_{c2} \to J/\psi + \gamma)}{\sigma(pp \to \chi_{c1} + X)\mathscr{B}(\chi_{c1} \to J/\psi + \gamma)} = \frac{N_{\chi_{c2}}}{N_{\chi_{c1}}} \cdot \frac{\epsilon_1}{\epsilon_2} \tag{5.2}$$

where $N_{\chi_{c1}}$ and $N_{\chi_{c2}}$ are the number of reconstructed χ_{c1} and χ_{c2} respectively extracted from data. The term $\varepsilon_1/\varepsilon_2$ consists of the detector acceptance ratio multiplied with the reconstruction efficiency ratio for χ_{c1} and χ_{c2}. The values of branching ratios taken from taken from Particle Data Book (PDG) [49], summarized in Table 5.1, are used to calculate the total production cross section ratio of by the expression 5.3.

$$\frac{\sigma(pp \to \chi_{c2} + X)}{\sigma(pp \to \chi_{c1} + X)} = \frac{N_{\chi_{c2}}}{N_{\chi_{c1}}} \cdot \frac{\epsilon_1}{\epsilon_2} \frac{\mathscr{B}(\chi_{c1} \to J/\psi + \gamma)}{\mathscr{B}(\chi_{c2} \to J/\psi + \gamma)} \tag{5.3}$$

In the next section, numbers of χ_{c1} and χ_{c2} events extracted from the maximum likelihood fit, and the ratio of the two values will be measured. The ratio $\varepsilon_1/\varepsilon_2$ is discussed in section 5.2 in detail.

Particle	Mass $[MeV/c^2]$	Width $[MeV/c^2]$	$\mathscr{B}(\chi_{cJ} \to J/\psi\gamma[\%]$)
χ_{c0}	3414.75 ± 0.31	10.5 ± 0.8	1.16 ± 0.08
χ_{c1}	3510.66 ± 0.07	0.88 ± 0.05	34.4 ± 1.5
χ_{c2}	3556.20 ± 0.09	1.95 ± 0.13	19.5 ± 0.8
J/ψ	3096.9 ± 0.01	0.093 ± 0.002	5.93 ± 0.06

Table 5.1: Values of Mass, Width and Branching fraction

5.1.1 Fitting Procedure

Due to the small intrinsic width of the states we are investigating, the observed signal shape is dominated by the experimental resolution. The resolution of the invariant mass difference Q, which is dominated by the energy resolution of the converted photon, is sufficient to cleanly separate the χ_{c1} and χ_{c2} peaks, as can be seen in Figure 5.1. However the resolution function presents a low-energy tail, typical of processes in which radiative losses play a role, as in the case of electrons from converted photons loosing energy in the silicon detector. Since the tail of the χ_{c2} falls under the χ_{c1} peak, and the tail of the χ_{c1} falls in part under the χ_{c0} peak, it is important to obtain a reliable parametrization of the resolution function in order to achieve an unbiased estimation of the ratio $N_{\chi_{c2}}/N_{\chi_{c1}}$, which cannot be derived directly from data.

The number of reconstructed χ_{c1} and χ_{c2} represented by $N_{\chi_{c1}}$ and $N_{\chi_{c2}}$, respectively, are extracted from data by performing an unbinned extended maximum likelihood fit to the mass difference spectrum in various p_T ranges of J/ψ using `Roofit` [62]. The pdf used for the extended likelihood fit takes the form:

$$P(Q) = \sum_{i=0}^{i<=2} N_i \cdot S_i(Q) + N_B \cdot S_B(Q), \tag{5.4}$$

where N_i is the number of signal events for each resonance, $S_i(Q)$ is the signal probability distribution function (PDF) for each resonance, N_B is the number of background events and $S_B(Q)$ is the background PDF. The correlation within$N_{\chi_{c1}}$ and $N_{\chi_{c2}}$ is taken into account when estimating the error for $N_{\chi_{c2}}/N_{\chi_{c1}}$. To empirically model processes, in which radiative losses are involved, the Crystal Ball function [51] is frequently used. It is composed of a gaussian core, described by the two parameters m and σ, and an exponential tail described by another two

$p_T(J/\psi)$	m [GeVc^2]	$\sigma[GeV]$	α_1	α_2
χ_{c1}				
7-9	3.50523 ± 0.00026	0.00635 ± 0.00020	0.588 ± 0.022	2.119 ± 0.093
9-11	3.50532 ± 0.00011	0.00648 ± 0.00009	0.579 ± 0.009	2.090 ± 0.069
11-13	3.50524 ± 0.00011	0.00647 ± 0.00009	0.557 ± 0.009	2.017 ± 0.054
13-16	3.50477 ± 0.00016	0.00706 ± 0.00013	0.584 ± 0.012	1.918 ± 0.045
16-20	3.50486 ± 0.00022	0.00670 ± 0.00024	0.524 ± 0.019	1.571 ± 0.060
20-25	3.50479 ± 0.00028	0.00694 ± 0.00037	0.516 ± 0.027	1.389 ± 0.078
χ_{c2}				
7-9	3.55057 ± 0.00017	0.00677 ± 0.00014	0.542 ± 0.013	2.122 ± 0.088
9-11	3.55000 ± 0.00060	0.00749 ± 0.00027	0.580 ± 0.032	2.151 ± 0.055
11-13	3.55002 ± 0.00015	0.00766 ± 0.00015	0.566 ± 0.011	1.982 ± 0.060
13-16	3.54947 ± 0.00027	0.00829 ± 0.00021	0.600 ± 0.018	1.880 ± 0.042
16-20	3.5505 ± 0.0011	0.00766 ± 0.00001	0.518 ± 0.000	1.681 ± 0.002
20-25	3.5502 ± 0.0020	0.00696 ± 0.00016	0.479 ± 0.072	1.28 ± 0.14

Table 5.2: Parameters of the double-sided crystal ball function

parameters, α (the transition point between gaussian and exponential) and n (the exponent index of the exponential part). The Crystal Ball function (Equation 5.5) allows the gaussian component of the detector resolution to be described, as well as the component corresponding to unrecovered energy losses by means of the exponential tail.

$$f(Q;\alpha,n,\sigma,m) = N \cdot \begin{cases} \exp(-\frac{(Q-m)^2}{2\sigma^2}), & \text{for } \frac{Q-m}{\sigma} > -\alpha \\ A \cdot (B - \frac{Q-m}{\sigma})^{-n}, & \text{for } \frac{Q-m}{\sigma} \leqslant -\alpha \end{cases} \tag{5.5}$$

where A $= \left(\frac{n}{|\alpha|}\right)^n \cdot \exp\left(-\frac{|\alpha|^2}{2}\right)$ and B $= \frac{n}{|\alpha|} - |\alpha|$

5.1.2 Number of χ_c from data

Simulations show that, in the signal shape, a small high-energy tail is also present. Therefore we choose to parametrize our resolution function with a double-sided Crystal Ball function, which is composed of both a high-energy and low-energy exponential tail, with independent exponents and transition points, but with a common gaussian core. As the α and n parameters are strongly correlated, we choose to fix n for both tails. The double sided crystal ball function is given in

equation 5.6.

$$f(Q;\alpha,n,\sigma,m) = N \cdot \begin{cases} \frac{\left(\frac{n_l}{|\alpha_l|}\right)^{n_l} \exp\left(-\frac{|\alpha_l|^2}{2}\right)}{(\frac{n}{|\alpha_l|} - |\alpha_l| - \frac{Q-m}{\sigma})^{-n_l}} & \text{for } \frac{Q-m}{\sigma} \leqslant -\alpha_l, \\ \frac{\left(\frac{n_r}{|\alpha_r|}\right)^{n_r} \exp\left(-\frac{|\alpha_r|^2}{2}\right)}{(\frac{n}{|\alpha_r|} - |\alpha_r| - \frac{Q-m}{\sigma})^{-n_r}} & \text{for } \frac{Q-m}{\sigma} \geqslant -\alpha_r, \\ \exp(-\frac{(Q-m)^2}{2\sigma^2}), & else \end{cases} \tag{5.6}$$

where α_l and n_l are parameters for low energy tail and α_r and n_r are parameters for high energy tail of double sided crystal ball function. The combinatorial background is modeled by a probability distribution function defined as

$$N_{bkg} = (x - q_0)^{\alpha_1} \cdot e^{(x-q_0)\cdot\beta_1}, \tag{5.7}$$

where α_1 and β_1 are free parameters and q_0 is fixed to 3.2 GeV.

For the χ_{c1} and χ_{c2} state we use the Monte Carlo simulation to extract resolution parameters. Results of the fits with Double Crystal Ball from Monte Carlo simulation for χ_{c1} and χ_{c1} are shown in Appendix A and the parameters extracted from the fit are summarized in Table 5.2. In the Figures 5.1, 5.2 and 5.3, the variable Q for χ_c candidates is plotted with $p_T(J/\psi)$ ranges [7.0 - 9.0], [9.0 - 11.0], [11.0 - 13.0], [13.0 - 16.0], [16.0 - 20.0] and [20.0 - 25.0] GeV/c.

The values of signal parameters of gaussian part of Crystal Ball function σ, mass and background parameters α_1 and α_2 are presented in the Table 5.2 for each p_T bin. Numbers of χ_{c1} and χ_{c2} events extracted from the maximum likelihood fit, and the ratio of the two values are reported in Table 5.3.

Few important features can be observed with the help of this method. First, an increase of the value of σ with $p_T(J/\psi)$ is observable for both resonances. At relatively small energies, we believe $\Delta p/p$ is constant. Photons associated with at J/ψ of higher p_T are likely to be more energetic, and therefore measured with slightly less precision. The same reason could explain the systematically higher value of σ for the χ_{c2}.

5.1.3 Study of Kinematic Variables from Data

We separate the χ_c states by their invariant mass. We consider the invariant mass of χ_{c1} in the region 3.45 to 3.52 GeV/c^2 and invariant mass of χ_{c2} in the region

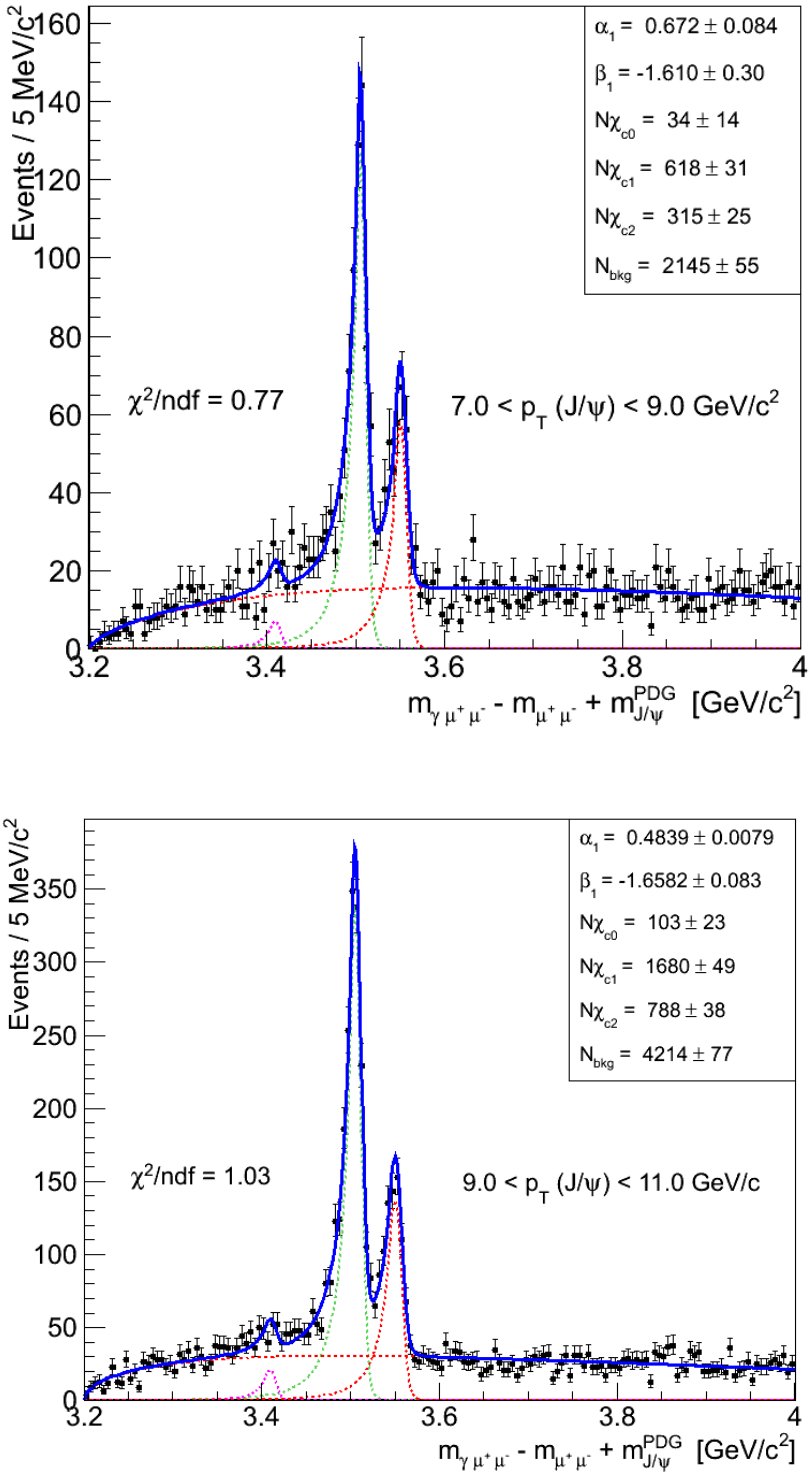

Figure 5.1: The distribution of the variable Q = $m_{\mu\mu\gamma}$ - $m_{\mu\mu}$ + $m_{J/\psi}$ for χ_c candidates with $p_T(J/\psi)$ in [7.0 - 9.0] GeV/c (top) and in [9.0 - 11.0] GeV/c (bottom)

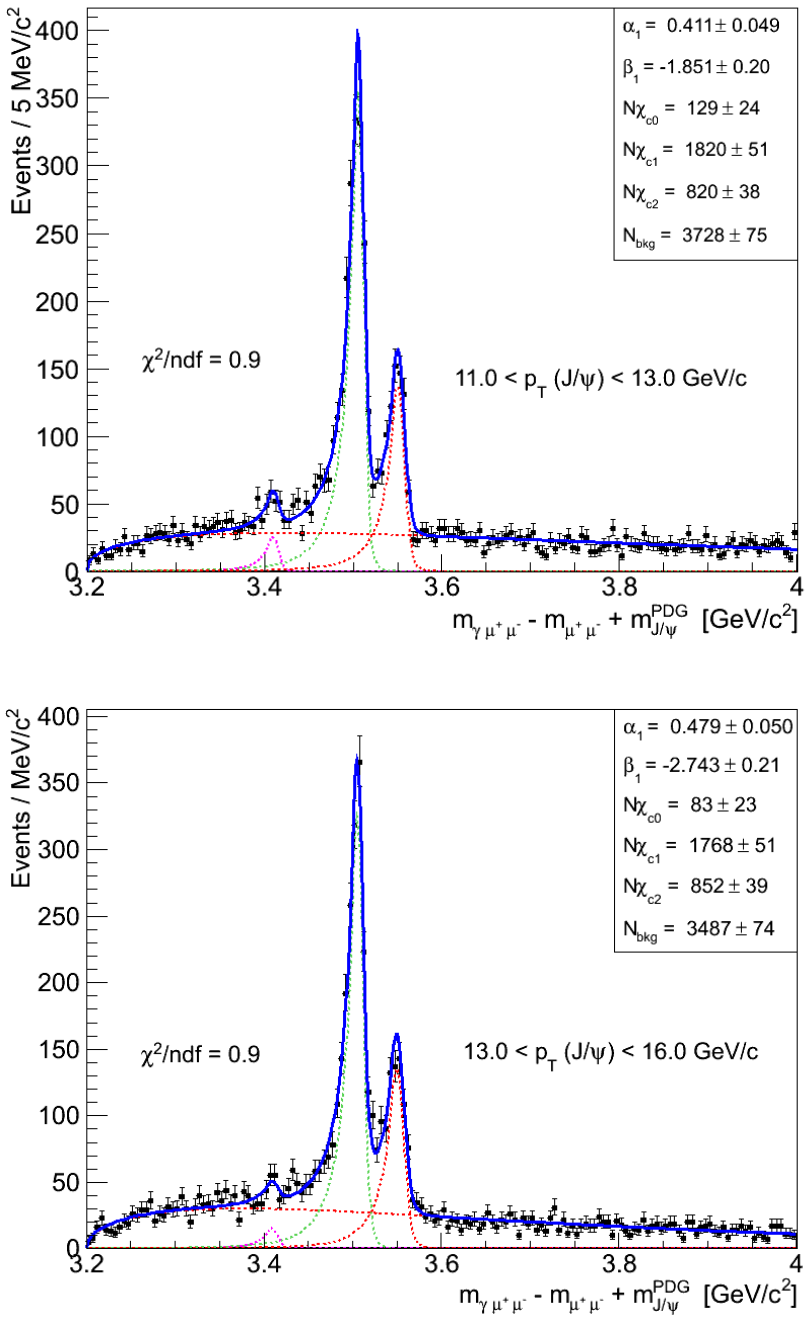

Figure 5.2: The distribution of the variable Q = $m_{\mu\mu\gamma}$ - $m_{\mu\mu}$ + $m_{J/\psi}$ for χ_c candidates with $p_T(J/\psi)$ in [11.0 - 13.0] GeV/c (top) and in [13.0 - 16.0] GeV/c (bottom)

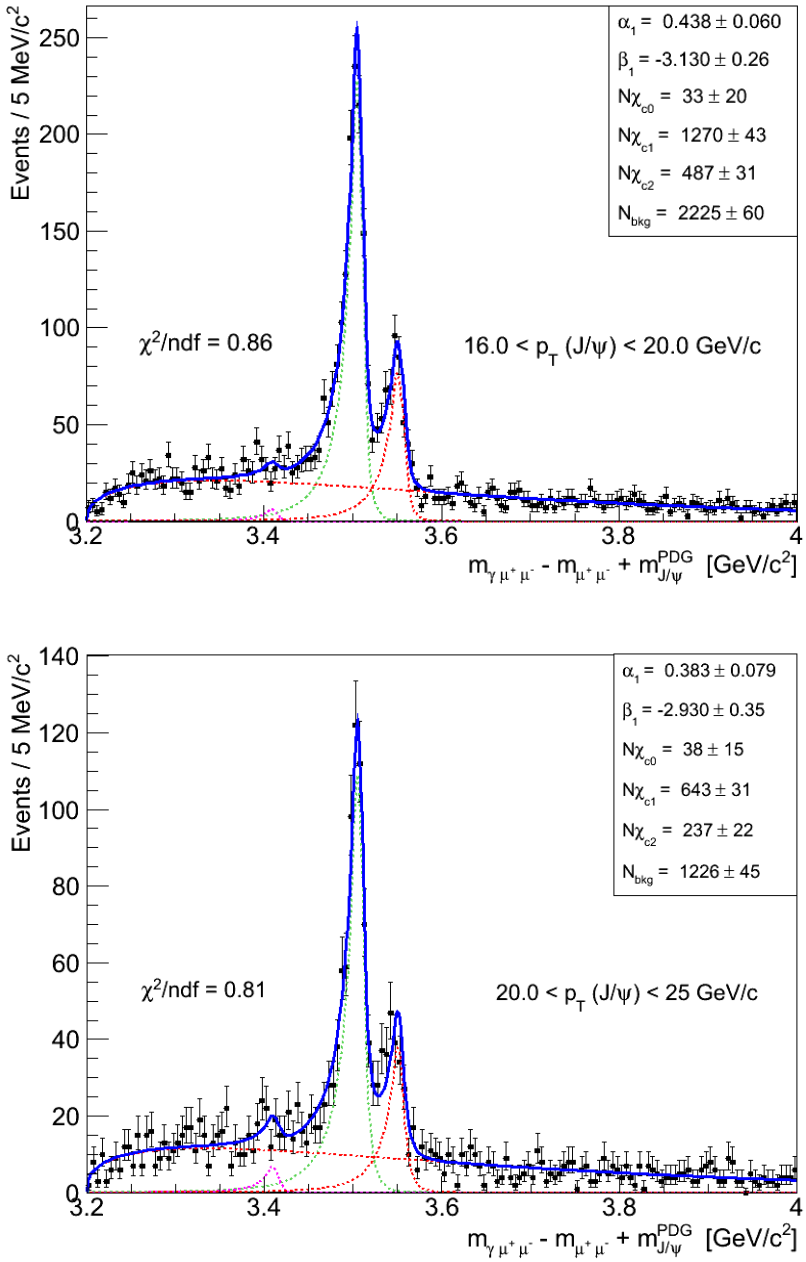

Figure 5.3: The distribution of the variable Q = $m_{\mu\mu\gamma}$ - $m_{\mu\mu}$ + $m_{J/\psi}$ for χ_c candidates with $p_T(J/\psi)$ in [16.0 - 20.0] GeV/c (top) and in [20.0 - 25.0] GeV/c (bottom)

$p_T^{J\psi}$ [GeV/c]	$N_{\chi_{c1}}$	$N_{\chi_{c2}}$	$N_{\chi_{c2}}$ / $N_{\chi_{c1}}$
7.0-9.0	618 ± 31	315 ± 24	0.510 ± 0.049
9.0-11.0	1680 ± 49	788 ± 37	0.469 ± 0.027
11.0-13.0	1819 ± 51	819 ± 38	0.451 ± 0.025
13.0-16.0	1767 ± 51	851 ± 39	0.482 ± 0.027
16.0-20.0	1269 ± 43	487 ± 30	0.384 ± 0.028
20.0-25.0	642 ± 31	236 ± 22	0.368 ± 0.040

Table 5.3: Numbers of χ_{c1} and χ_{c2} events extracted from the maximum likelihood fit, and the ratio of the two values. Uncertainties are statistical only

3.52 to 3.57 GeV/c^2. The presence of cross contamination and background events is not taken into account. Kinematic distributions of J/ψ and converted photons coming from radiative decay of χ_c states are studied to understand their behavior. Transverse momentum and rapidity distribution for both χ_c states and J/ψ are shown in Figure 5.4 and 5.5. While p_T spectrum and η of converted photons is plotted in Figure 5.6. It is observed that the rapidity and pseudorapidity distri-

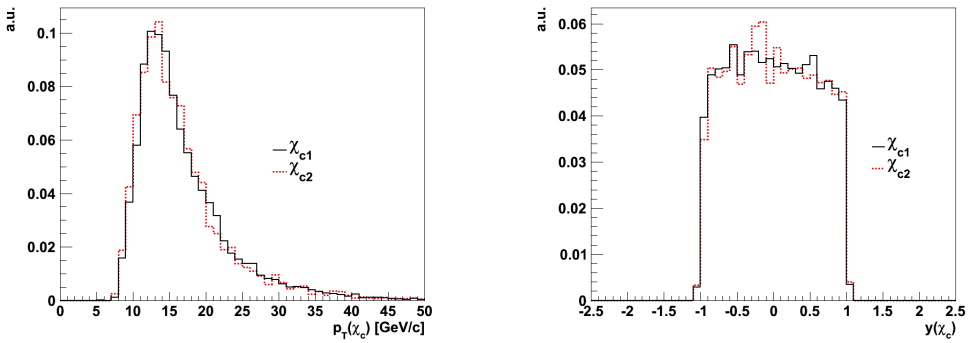

Figure 5.4: Kinematic distribution from data for p_T of χ_c (top) and rapidity of χ_c (bottom)

butions of γ and J/ψ from χ_{c1} and χ_{c2} are very similar and uniformly distributed in the range [-1, 1]. The p_T spectrum of J/ψ from χ_{c1} and χ_{c2} are also similar but p_T spectrum of γ coming from χ_{c2} is harder than that of χ_{c1}. In Figure 5.4 the rapidity distribution for both χ_{c1} and χ_{c2} are also similar where p_T spectrum of χ_{c2} is relatively harder than that of χ_{c1}. The harder p_T spectrum of χ_{c2} is due to harder p_T spectrum of photons.

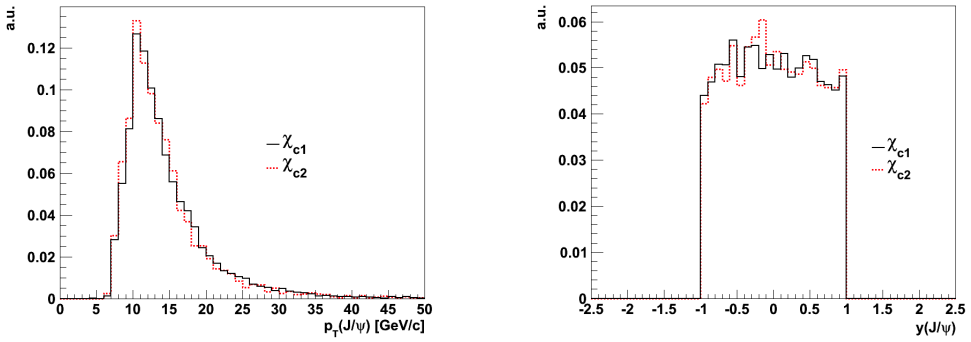

Figure 5.5: Kinematic distribution from data for p_T of J/ψ (top) and rapidity of J/ψ (bottom)

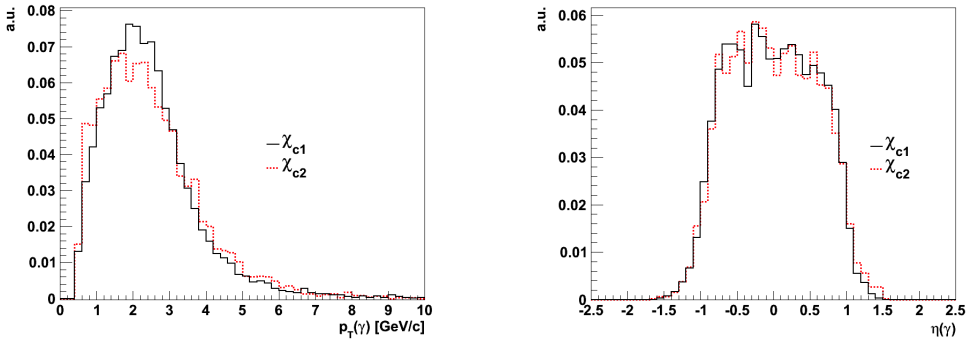

Figure 5.6: Kinematic distribution from data for p_T of γ (top) and pseudorapidity of γ (bottom)

5.2 Study of Acceptance and Efficiency

The study of acceptance and efficiency is an important part to study the cross section of any process. In the measurement of the cross section ratio of χ_{c2} to χ_{c1}, ratio of efficiency also appear as shown by Equation 5.2. The MC sample generation of χ_c states and the measurement of acceptance and reconstruction efficiency of χ_c states is discussed in this section.

5.2.1 MC Sample Generation

To determine the efficiency ratio of χ_c states, a Monte Carlo simulation sample of equal number of χ_{c1} and χ_{c2} is generated. The ratio $\varepsilon_1/\varepsilon_2$ is the product of detector acceptance ratio and the reconstruction efficiency ratio for χ_{c1} and χ_{c2}.

Detector acceptance is defined as the probability to find the decay products of χ_{c1} and χ_{c2} within the fiducial region of the CMS detector. This probability is less than one because certain events with generated χ_c can be lost due to an imperfect detector. Reconstruction efficiency gives the probability to reconstruct χ_c with respect to the total number of χ_c in the given fiducial region of the detector.

Ths MC sample was produced by using a PYTHIA particle gun [52] configured in such a way that χ_{c1} and χ_{c2} particles are generated with the same p_T spectrum, chosen to be the one observed by the CMS experiment for the ψ', ranging between 5 GeV/c and 40 GeV/c [53]. The motivation of choosing p_T spectrum of ψ' is the proximity of ψ' mass (3.686 GeV/c^2) with the masses of χ_c states. Another reason is the existence of p_T spectrum of ψ' in various rapidity ranges including the observed rapidity range of χ_c states. We use the p_T spectrum of ψ' in the range $|\mathrm{y}(\ \psi')| < 1.2$, and parameterize the data using the expression 5.10.

The particle gun method allows large samples of detectable χ_{c1} and χ_{c2} to be generated. The method is however based on the following assumptions:

1. The p_T spectrum of the χ_{c1} as produced in the pp interaction does not differ from the p_T spectrum of the χ_{c2}. The χ_c gun generates the two states with the same p_T spectrum.

2. The p_T spectrum of the photon emitted by the χ_{c1} and χ_{c2} is determinted by the kinematics of the process, and polarization does not affect the two photon spectra in different ways. The χ_c gun generates unpolarized particles.

The χ_c states are generated in the rapidity range $|y| < 1.25$. Both χ_c states are forced to decay to $J/\psi + \gamma$. The decay products are then processed through the full CMS detector simulation, trigger selection and reconstruction. In order to increase computational efficiency, only events in which a conversion occurs are passed through the trigger emulation and reconstruction. The input $p_T(\chi_c)$ spectrum used for the particle gun simulation is derived from a parameterizaion of the data available in [48] for the ψ' in the range $|y(J/\psi)| < 1.2$. The functional form for the parametrization has the expression:

$$\frac{dN}{dp_T} \propto p_T \left(1 + \frac{1}{\beta - 2} \frac{p_T^2}{< p_T^2 >}\right)^{-\beta} \tag{5.8}$$

where β and $< p_T^2 >$ are free parameters and their values are $\beta = 3.71 \pm 0.27$, $< p_T^2 > = 19.5 \pm 5.8$. The fitted ψ' spectrum used to model the $p_T(\chi_c)$ spectrum is shown in Figure 5.7.

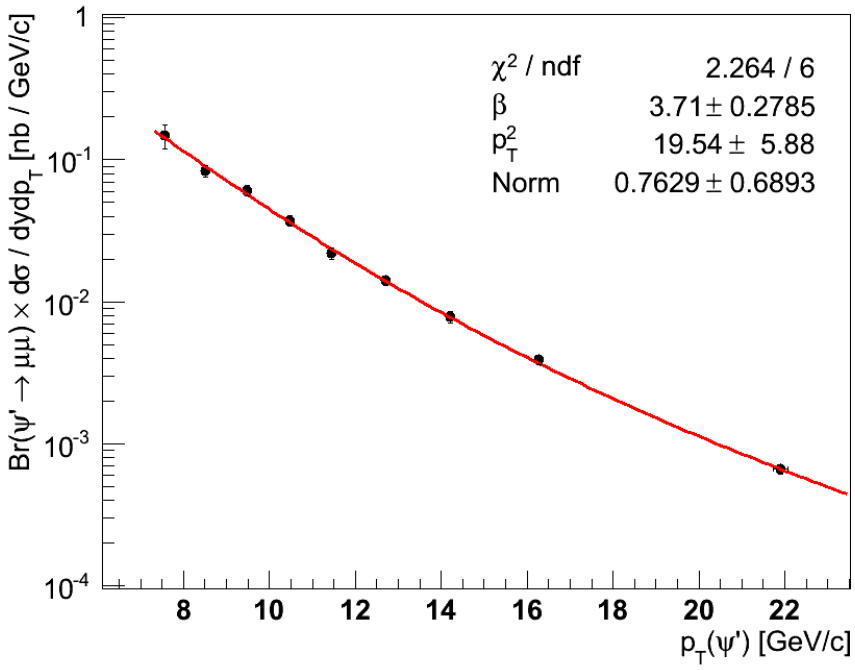

Figure 5.7: The measured p_T spectrum of ψ'. The red line is fitted with Equation 5.10 used as input distributeion for the PYTHIA particle gun

5.2.2 Decay Angular Distribution

Particle gun used to produce the χ_c monte carlo gives a flat distribution of photons and muons along polar and azimuthal direction. For calculation we take polar angle and azimuthal angle between positive muons and J/ψ's. Direction of both muon and J/ψ is taken to be in their parent's rest frame i.e muon in J/ψ rest frame and J/ψ in χ_c rest frame. These angles are denoted by θ' and ϕ' respectively (Figure 5.8). The polar angle θ is between J/ψ and χ_c, when J/ψ is in χ_c rest frame and χ_c is in laboratory frame.

The angles θ, θ' and ϕ' gives polarization of χ_c and J/ψ respectively. To first approximation the distribution of polar angle $\mathrm{W}(\theta', \phi', \theta)$ is given by

$$W(\theta') = 1 - \lambda_{\theta'} cos^2\theta' \tag{5.9}$$

Where W is integrated over θ and ϕ' in Equation 5.9. For χ_{c1} $\lambda_{\theta'} = 1/3$ and for χ_{c2} $\lambda_{\theta'} = 1/13$. To get correct angular distribution of J/ψ which is compatible with prediction, a reweighting procedure is applied to events produced by particle gun. Instead of polarization we studied helicity $h = J.\overrightarrow{P}/|P|$ using MC technique.

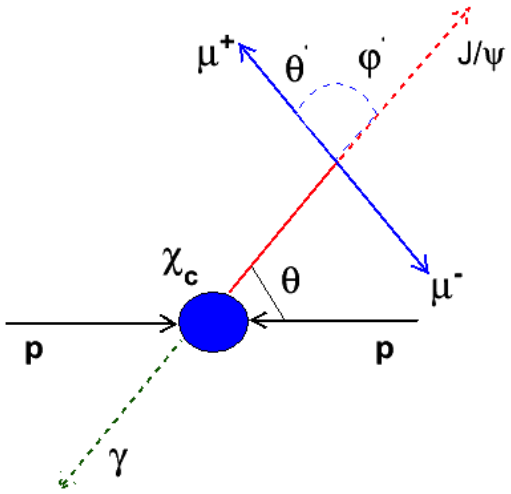

Figure 5.8: Production of χ_c in pp collisions and its decay to $J/\psi + \gamma$.

For a χ_{c1} h can be $0, \pm 1$ and for a χ_{c2} it can be $0, \pm 1, \pm 2$. The uncertainties coming in our result due to different values of polarization is taken as systematic uncertainties.

5.2.3 Detector Simulation, Reconstruction and Selection of MC Sample

The MC events of χ_c states generated using PYTHIA particle gun with the ψ' p_T spectrum and properly reweighed angular distribution. This sample then processed through the full CMS detector simulation using CMS software (CMSSW). This simulation is based on GEANT4 [54, 55], which is a software package used to simulate the passage of particles through matter. The simulated raw data is then passed through standard CMSSW reconstruction algorithms, trigger selection, χ_c reconstruction and selection cuts as real data.

Until now we simulated only the tracks coming from χ_c particles, which are $\mu^+\mu^-$ and γ tracks. To measure the corrected ratio of $\varepsilon_1/\varepsilon_2$, we add additional

digitized signals of low p_T tracks from the underlying events and pileup. All particles coming from soft interaction of partons are called the underlying events. Pileup is a result of multiple interactions caused by the existence of many parton collisions per bunch crossing.

To achieve a more realistic way to determine the ratio of efficiencies we added tracks from the underlying event and pileup. We use the standard CMSSW mixing procedure [56] which adds tracks from the underlying events and pileup to our muon, electron and positron tracks as simulated with CMSSW. The mixing scheme which we used is $mix\_E7TeV\_AVE\_5\_BX156$ and it was chosen because it was found to best match the observed distribution of the number of reconstructed primary vertices in Run2011A and Run2011B. After adding the mixing of underlying events and pileup to the simulated digitized decay products of χ_c states, the simulated sample is processed through standard CMSSW reconstruction algorithms, trigger selection 4.2, χ_c reconstruction and selection as real data. The final reconstructed event sample is used to measure and study $\varepsilon_1/\varepsilon_2$ ratio.

5.2.4 Ratio of Efficiencies of χ_{c1} and χ_{c2}

The ratio of efficiencies $\varepsilon_1/\varepsilon_2$ for the different J/ψ transverse momentum bins is determined using

$$\frac{\varepsilon_1}{\varepsilon_2}(p_T(J/\psi)) = \frac{N^{rec}_{\chi_{c1}}}{N^{gen}_{\chi_{c1}}} / \frac{N^{rec}_{\chi_{c2}}}{N^{gen}_{\chi_{c2}}} \tag{5.10}$$

where N^{rec} is the number of candidates reconstructed, and N^{gen} is the number of candidates generated in the Monte Carlo simulation in the kinematic range $|y^{J/\psi}| < 1.0$, $p_T^{\gamma} > 0.5$GeV/c. The resulting values are shown in Table 5.4, where the error due to the limited size of the simulation sample is assumed to be binomial. The errors are assigned after reweighting [57].

5.2.5 Study of Kinematic Variables from MC

Transverse momentum distributions of converted photons and the J/ψ for χ_{c1} and χ_{c2} generated with Pythia Monte Carlo particle gun and reconstructed with the CMS detector with selection cuts discussed in chapter 4. Figure 5.9 shows the p_T distribution for the generated and reconstructed χ_{c1} and χ_{c2} candidates. The plots

$p_T^{J\psi}$ [GeV/c]	$\varepsilon_1/\varepsilon_2$
7.0-9.0	0.903 $\pm$0.023
9.0-11.0	0.935 $\pm$0.019
11.0-13.0	0.945 $\pm$0.021
13.0-16.0	0.917 $\pm$0.022
16.0-20.0	0.981 $\pm$0.031
20.0-25.0	1.028 $\pm$0.049

Table 5.4: Ratio of efficiencies $\varepsilon_1/\varepsilon_2$ measured with $PYTHIA$ particle gun. Errors are statistical only.

lead to the conclusion that the transverse momentum spectrum of reconstructed χ_{c2} photon is harder with respect to the χ_{c1} photon and the transverse momentum distributions of J/ψ from χ_{c1} and χ_{c2} are very similar both at the generation and reconstruction level. The transverse momentum spectra of generated χ_c in Figure 5.9 are almost identical as expected because both of them were generated with identical input $p_T(\psi')$ spectrum. The p_T distributions of the generated and reconstructed J/ψ and converted photons are also shown in Figure 5.10 and 5.11 respectively.

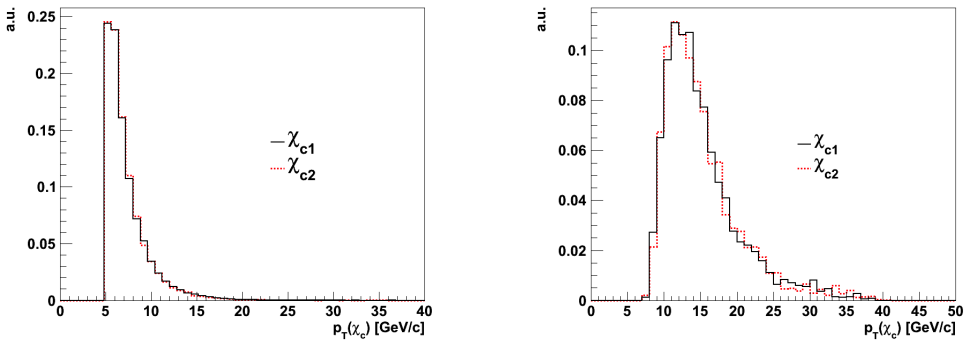

Figure 5.9: p_T distribution of generated (left) and reconstructed (right) χ_c MC events.

Since we are going to measure $N_{\chi_{c2}}/N_{\chi_{c1}}$ as a function of $p_T(J/\psi)$, we want to study the correlations among the quantities $p_T(\chi_c)$, $p_T(J/\psi)$ and $p_T(\gamma)$. We generated the χ_c states using PYTHIA particle gun with flat p_T spectrum. This is a useful assumption to study other kinematic variables of χ_{c1} and χ_{c2}. We plot $p_T(\chi_c)$ vs $p_T(J/\psi)$ and$p_T(J/\psi)$ vs $p_T(\gamma)$, shown in Figure 5.12 and 5.13

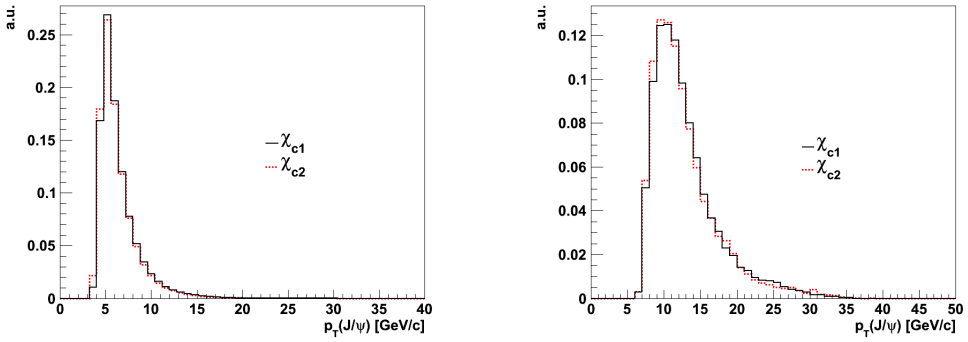

Figure 5.10: p_T distribution of generated (left) and reconstructed (right) γ MC events.

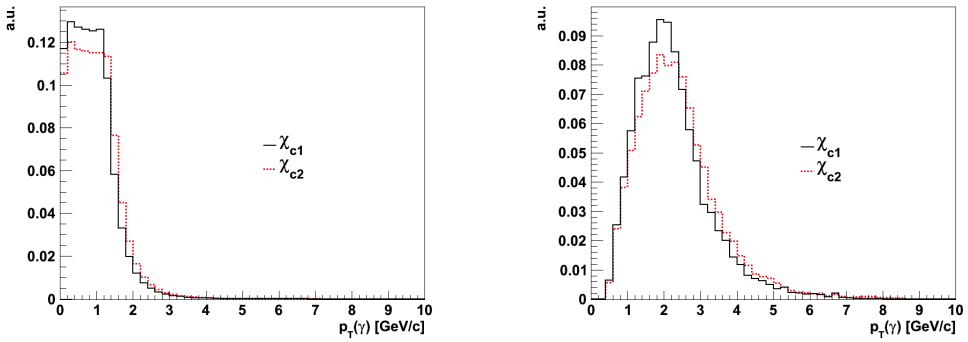

Figure 5.11: p_T distribution of generated (left) and reconstructed (right) J/ψ MC events.

respectively.

In Figure 5.12, the slope of the fit of the profile histogram is 0.875 $\pm$ 0.001 for the χ_{c1} and 0.879 $\pm$ 0.001 for the χ_{c2}, showing that the J/ψ takes most of the transverse momentum of the χ_c, with a very small difference between the two states. In Figure 5.13, we show the correlation between $p_T(\gamma)$ and $p_T(J/\psi)$ for the two states. The slope of the profile plot is 0.128 $\pm$ 0.001 and 0.142 $\pm$ 0.001 respectively, showing that photons from the χ_{c2} have on average a p_T higher by 10% with respect to photons from the χ_{c1}.

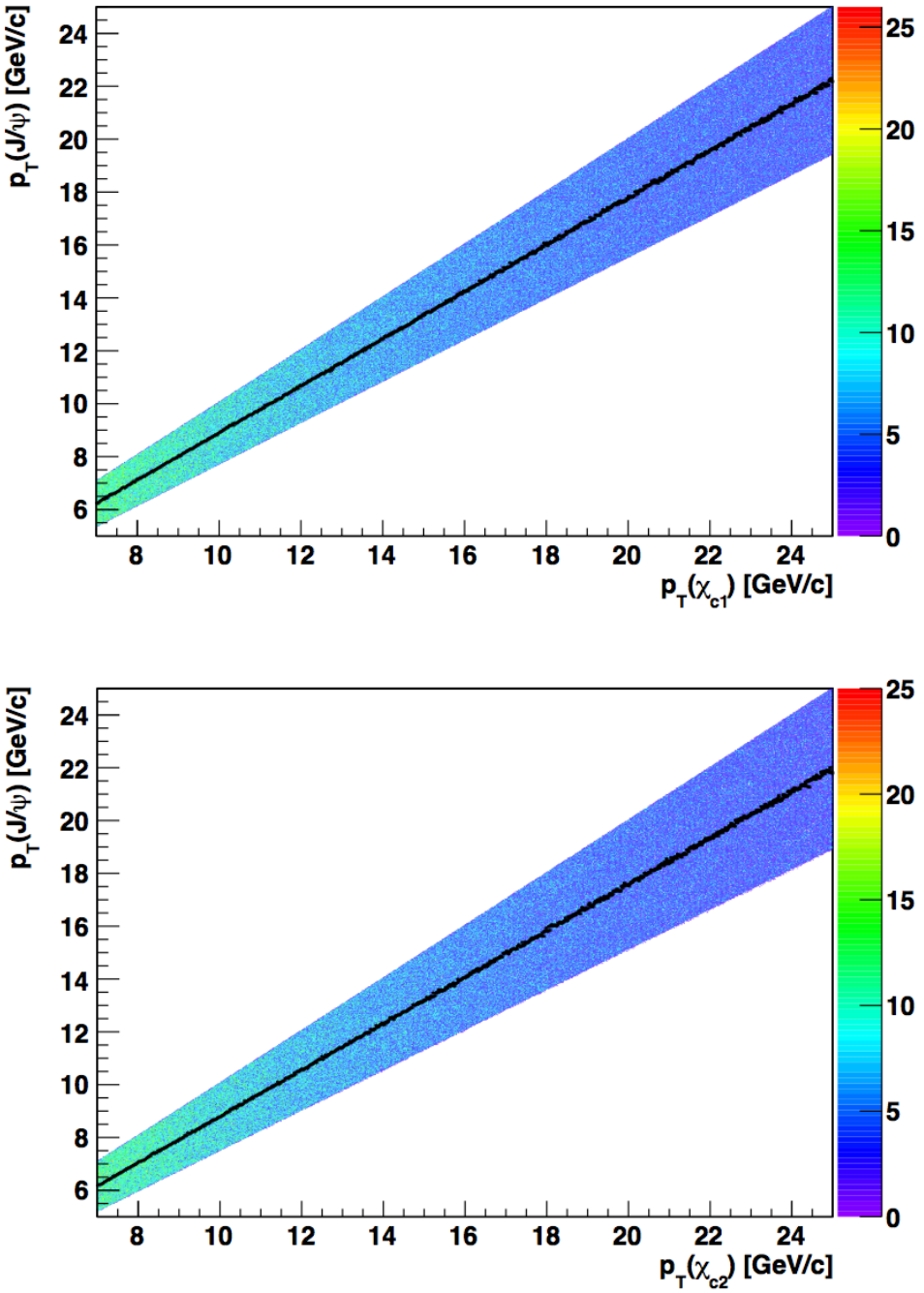

Figure 5.12: $p_T(J/\psi)$ vs $p_T(\chi_c)$ with mean distributions superimposed for χ_{c1} (top) and χ_{c2} (bottom) generated with Pythia Monte Carlo particle gun with flat p_T input spectrum for χ_c. The slopes of the mean distributions are 0.875 and 0.879 respectively

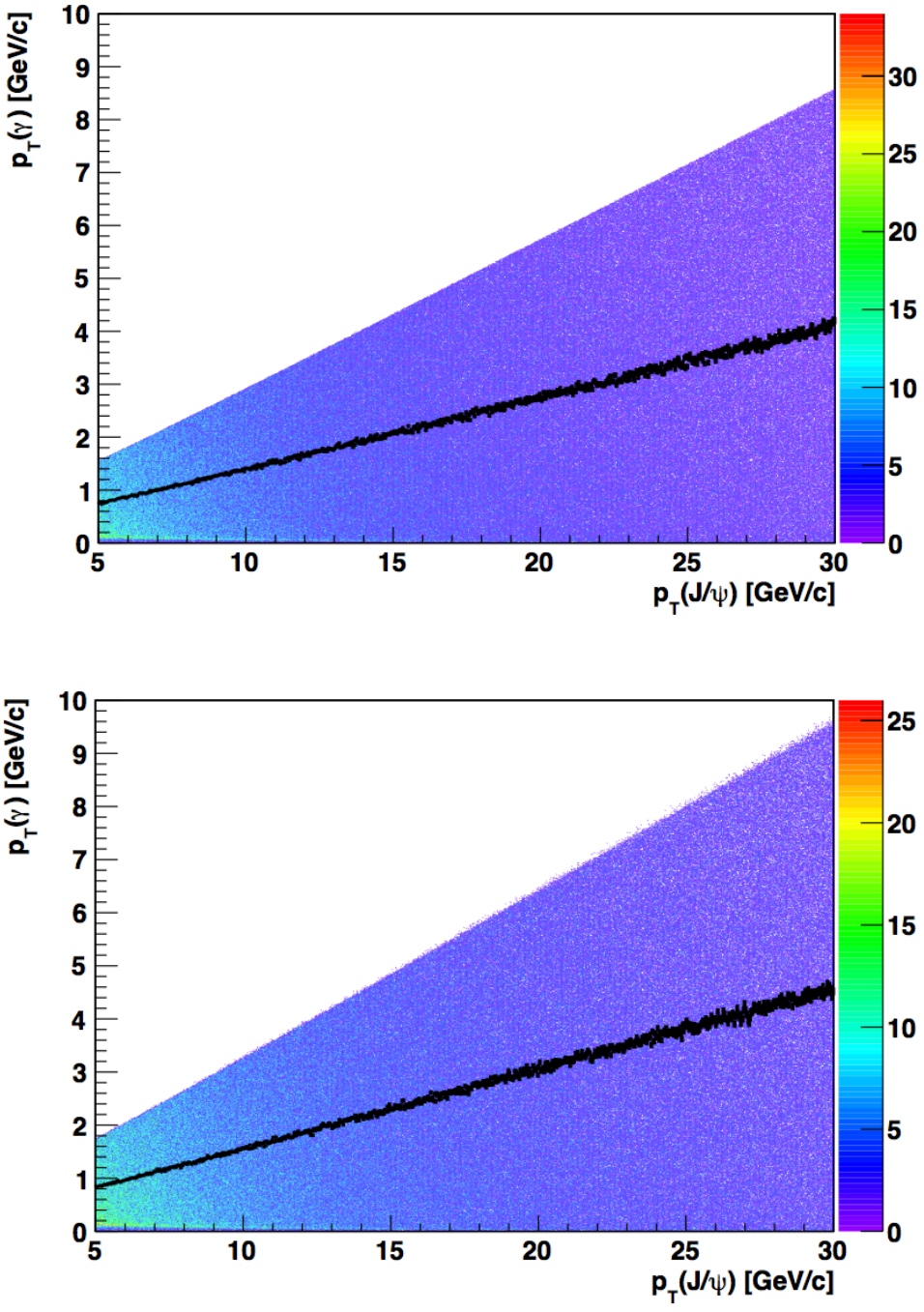

Figure 5.13: $p_T(\gamma)$ vs $p_T(J/\psi)$ with mean distributions superimposed for χ_{c1} (top) and χ_{c2} (bottom) generated with Pythia MC particle gun with flat p_T input spectrum for χ_c. The slopes of the mean distributions are 0.128 and 0.142 respectively.

5.2.6 Reconstruction Efficiency of J/ψ

To quantify the difference in acceptance we estimated the ratio of reconstruction efficiencies for J/ψ coming from χ_{c1} and χ_{c2} respectively, by comparing the number of reconstructed J/ψ with respect to the generated J/ψ. The resulting ratio $\varepsilon_{\chi_{c1}}(J/\psi)/\varepsilon_{\chi_{c2}}(J/\psi)$ is shown in Figure 5.14. From the fact that this ratio is compatible with one for all the values of $p_T(J/\psi)$. We infer that the deviation from unity of $\varepsilon_1/\varepsilon_2$ is entirely due to a slightly different photon acceptance for the two states.

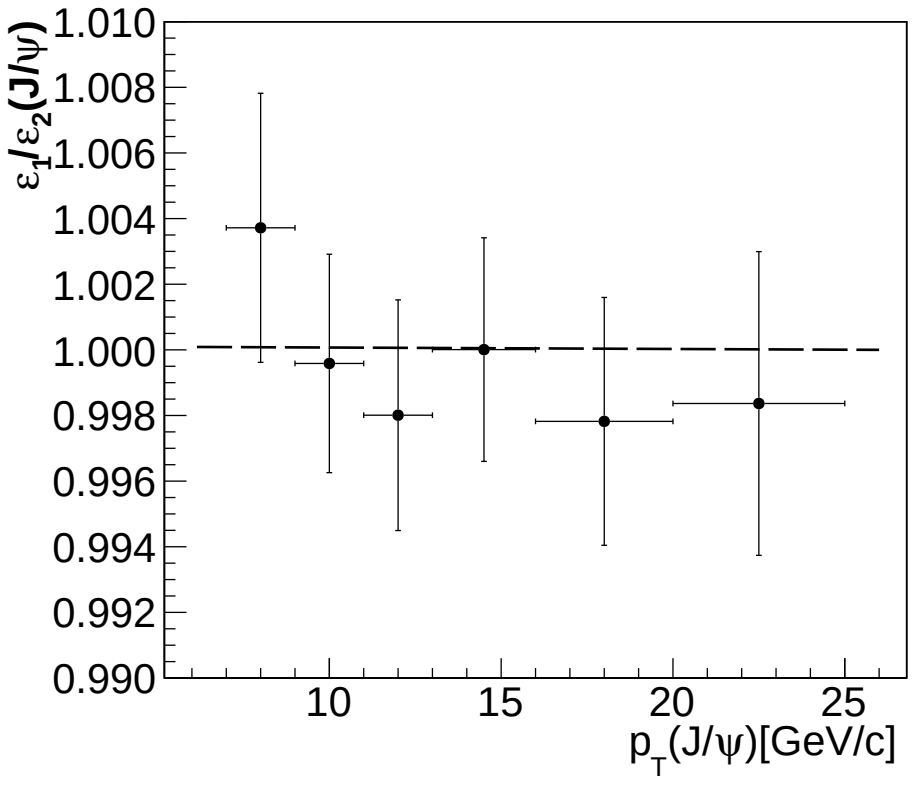

Figure 5.14: Ratio of reconstruction efficiencies for J/ψ coming from χ_{c1} and χ_{c2}

5.2.7 Reconstruction Efficiency of Photons

To understand the acceptance and reconstruction efficiency of χ_c quantitively we evaluate $\varepsilon(\chi_c)$ as a function of $p_T(\gamma)$ given below

$$\varepsilon(\chi_c) = \frac{N^{rec}_{\chi_c}}{N^{gen}_{\chi_c}}(p_T(\gamma)) \tag{5.11}$$

where N^{rec} is the number of reconstructed χ_{c1} and χ_{c2} in the kinematic range $|y_{J/\psi}| < 1.0$ and $p_\gamma > 0.5$ GeV/c. The efficiency $\varepsilon(\chi_c)$ is proportional to

$$\varepsilon(\chi_c) \propto \rho^{\gamma}_{conv} \times \varepsilon^{\gamma}_{reco} \times \varepsilon^{\chi_c}_{sel} \tag{5.12}$$

where ρ^{γ}_{conv} is the probability for a photon to convert in the tracker, $\varepsilon^{\gamma}_{reco}$ is the photon conversion reconstruction efficiency and $\varepsilon^{\chi_c}_{sel}$ is the χ_c selection efficiency. The conversion probability of a photon is

$$\rho^{\gamma}_{conv} \propto \frac{1}{\lambda^{\gamma}} \propto \frac{P}{X_0} \tag{5.13}$$

where λ^{γ} is the mean free path of the photon to convert into an e^+e^- pair in the tracker. The factor $\frac{P}{X_0}$ is the average conversion probability where P $\sim 7/9$ [58] and X_0 is the radiation length (thickness of material where an electron reduces its energy by a factor of 1/e emitting bremsstrahlung radiation). The value of X_0 varies with pseudorapidity (η) and azimuthal angle (ϕ_0) in the tracker depending on the material distribution as explained in Chapter 2. On average, about 70% of all the photons convert into an e^+e^- pair in the tracker.

The convolution of the conversion probability, the reconstruction and the selection efficiency, $\rho^{\gamma}_{conv} \times \varepsilon^{\gamma}_{reco} \times \varepsilon^{\chi_c}_{sel}$, is shown in Figure 5.15 as a function of p_T of the photon in the pseudorapidity range $|\eta(\gamma)| < 1$. Figure 5.15 is very important because it shows the very small probability of the χ_c photon to convert and its very small reconstruction efficiency. Most of the χ_c photons are in the range 0.5-5.0 GeV/c (Figure 5.15). The slope of the efficiency curve between 0.5-5.0 GeV/c is very steep which leads to a large variation in the reconstruction of χ_c photons in that region. This combined with the different momentum spectra for χ_{c1} and χ_{c2} photons leads to their different acceptance with CMS detector.

Since the value of the radiation length X_0, varies with pseudorapidity which affects the conversion probability. We studied the dependence of $\rho^{\gamma}_{conv} \times \varepsilon^{\gamma}_{reco} \times \varepsilon^{\chi_c}_{sel}$ as a function of the pseudorapidity of the photon in the ranges [-1.0,-0.6], [-0.6,-0.2], [-0.2,0.2], [0.2,0.6], [0.6,1.0]. We did not find significant fluctuations in $\rho^{\gamma}_{conv} \times \varepsilon^{\gamma}_{reco} \times \varepsilon^{\chi_c}_{sel}$ for the different pseudorapidity ranges of the χ_c photon. In the same spirit, we used the particle gun to understand the origin of the difference of a few percent between ε_1 and ε_2 that we observe. The ratio $\varepsilon_1/\varepsilon_2$, which

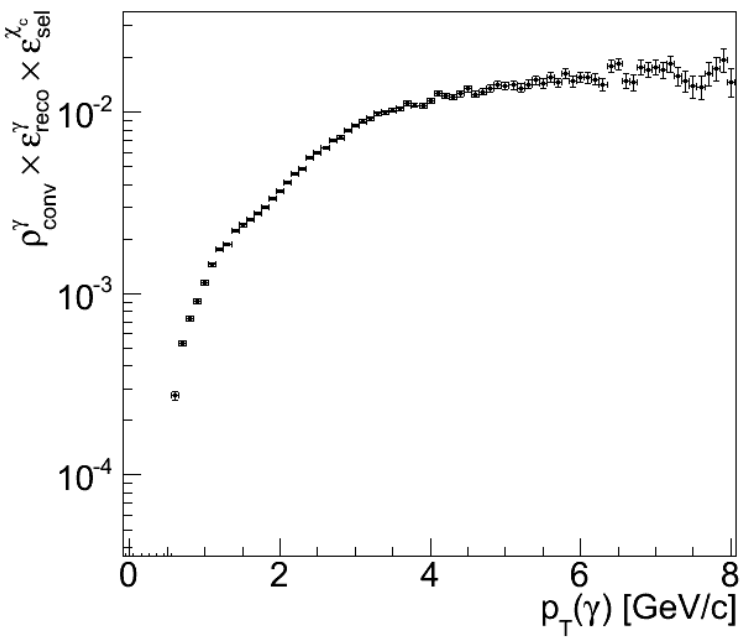

Figure 5.15: Kinematic distribution from data for p_T of γ (top) and pseudorapidity of γ (bottom)

is actually the ratio of the geometric acceptances multiplied by the ratio of the reconstruction efficiencies, could be influenced by the different acceptance for the muon pair originating from the J/ψ or the different p_T spectrum of the emitted photon, resulting from the decay of the χ_{c1} and χ_{c2}.

5.3 Consistency Checks in the Measurement of $\varepsilon_1/\varepsilon_2$

5.3.1 Reweighing Procedure

We want to test the assumption on the production p_T spectra for χ_{c1} and χ_{c2} states. For that we compare the spectra obtained from the Pythia Monte Carlo particle gun with the spectra obtained experimentally. The ratio histograms of the generated and measured p_T spectra for χ_{c1} and χ_{c2} is used to reweight the events generated with the Pythia particle gun. The goal is to match the generated and observed p_T spectra for χ_{c1} and χ_{c2}. We recalculate the ratio $\varepsilon_1/\varepsilon_2$ using reweighted events when counting the numbers $N^{rec}_{\chi_{c1}}$ and $N^{rec}_{\chi_{c2}}$. The values of $N^{gen}_{\chi_{c1}}$

and $N_{\chi_{c2}}^{gen}$ remain the same as in the default case. The comparison between the default method and the method with reweighting gives a maximum difference of 3% in the ratio $\varepsilon_1/\varepsilon_2$. For example, in the range $7.0 < p_T(J/\psi) < 25.0$ GeV/c we obtain $\varepsilon_1/\varepsilon_2 = 0.958 \pm 0.022$ for the default case and $\varepsilon_1/\varepsilon_2 = 0.935 \pm 0.022$ for the weighted case.

5.3.2 Effect of $p_T(\gamma)$ on Efficiency

We calculate the ratios $N_{\chi_{c2}}/N_{\chi_{c1}}$ and $\varepsilon_1/\varepsilon_2$ for different cuts on $p_T(\gamma)$, namely 0.75, 1.00 and 1.25 GeV/c, and compare their values with the default cut value of $p_T(\gamma) = 0.5$ GeV/c. This is done to ensure that the result for $\frac{N_{\chi_{c2}}}{N_{\chi_{c1}}} \cdot \frac{\varepsilon_1}{\varepsilon_2}$ is not dependent on the steep photon reconstruction efficiency, see Figure 5.15. The fluctuations of $\frac{N_{\chi_{c2}}}{N_{\chi_{c1}}} \cdot \frac{\varepsilon_1}{\varepsilon_2}$ for different cuts are of the order of 2% with maximum difference in the first $p_T(J/\psi)$ bin of 6%. The fluctuations are all within the statistical uncertainties.

5.3.3 Effect of π^0 Rejection

It might be possible that the π^0 rejection cut could bias our measurement. The cut could favor high energy photons, and the fact that the χ_{c2} emits slightly harder photons would lead to an increased acceptance for this state. In fact, the measurement of $\varepsilon_1/\varepsilon_2$ that we described, in which χ_c decays are mixed with minimum bias events, already taken into account in the ratio of acceptances. As a check, we calculated R_p in two ways: with and without applying the π^0 cut to data to measure $N_{\chi_{c2}}/N_{\chi_{c1}}$ and to simulation to measure $\varepsilon_1/\varepsilon_2$.

We calculated the values of $N_{\chi_{c2}}/N_{\chi_{c1}}$ and $\varepsilon_1/\varepsilon_2$ without applying the π_0 rejection cut. The effects of this π_0 cut rejection is summarized in Table 5.5 and 5.6, and we found the values compatible with the default values.

5.4 Systematic Uncertainties

Several types of systematic uncertainties are addressed. In particular, we investigate possible effects that could influence the measurement of the numbers of χ_{c1}

$p_T^{J\psi}$ [GeV/c]	$N_{\chi_{c1}}$	$N_{\chi_{c2}}$	$N_{\chi_{c2}}$ / $N_{\chi_{c1}}$
7.0-9.0	697 ± 34	338 ± 28	0.485 ± 0.048
9.0-11.0	1922 ± 56	912 ± 43	0.475 ± 0.027
11.0-13.0	2166 ± 58	978 ± 44	0.452 ± 0.024
13.0-16.0	2038 ± 57	957 ± 44	0.470 ± 0.026
16.0-20.0	1464 ± 48	566 ± 35	0.387 ± 0.028
20.0-25.0	738 ± 35	260 ± 25	0.353 ± 0.040

Table 5.5: The values of $N_{\chi_{c2}}$ / $N_{\chi_{c1}}$ without π^0 rejection

$p_T^{J\psi}$ [GeV/c]	$\varepsilon_1/\varepsilon_2$
7.0-9.0	0.902 ± 0.028
9.0-11.0	0.890 ± 0.017
11.0-13.0	0.909 ± 0.016
13.0-16.0	0.939 ± 0.016
16.0-20.0	0.922 ± 0.017
20.0-25.0	0.956 ± 0.022

Table 5.6: The values of $\varepsilon_1/\varepsilon_2$ without π^0 rejection

and χ_{c2} from data, the evaluation of $\varepsilon_1/\varepsilon_2$ from the MC simulation, and the derivation of the R_p ratio. In Table 5.7 the various sources of systematic uncertainties and their contributions to the total uncertainty are summarized. The following subsections describe how the various contributions are evaluated.

5.4.1 Uncertainty from the mass fit and χ_{c1} and χ_{c2} counting

Signal Model

We estimated the systematic uncertainty resulting from the parametization of our resolution function by varying the double-sided Crystal Ball parameters derived from MC within their uncertainties. We measure the ratio $N_{\chi_{c2}}/N_{\chi_{c1}}$ for all possible variations of those parameters, which are recorded in Table B.1. We observe that the largest deviations from the default value of $N_{\chi_{c2}}/N_{\chi_{c1}}$ come from variations of the parameter α_l for χ_{c2}. The maximum deviation with respect to the default case in the last $p_T(J/\psi)$ bin [20-25], due to low statistics in this p_T bin. We recorded this variation as systematics in Table 5.7.

Background Model

In order to study the uncertainty on the determination of $N_{\chi_{c2}}/N_{\chi_{c1}}$ which is derived from the the background parametrization, we used an alternative background PDF, namely the so called $D^* - D^0$ mass difference function given below and available in Roofit [62].

$$S_B = \left(1 - exp\left(-\frac{Q - q_0}{c}\right)\right) \cdot \left(\frac{Q}{q_0}\right)^a + b \cdot \left(\frac{Q}{q_0} - 1\right) \tag{5.14}$$

where $P(Q) = \sum_{i=0}^{i<=2} N_i \cdot S_i(Q) + N_B \cdot S_B(Q)$, $q_0 = 3.2$ and a, b, c are free parameters.

We take the relative difference in $N_{\chi_{c2}}/N_{\chi_{c1}}$ obtained with this parametrization and our default parametrization as systematic error, as shown in Table 5.3. We take the difference in $N_{\chi_{c2}}/N_{\chi_{c1}}$ obtained with $D^* - D^0$ parameterization and our default parameterization as systematic uncertainties summarized in Table 5.7.

5.4.2 Uncertainty in the ratio of efficiencies

Simulation sample size

We have generated 240 million events with χ_{c1} and χ_{c2} using Pythia Monte Carlo particle gun. The big sample is chosen due to the fact that the reconstruction efficiency of converted photons with the CMS tracker is very low. As Figure 5.15 for $p_T(\gamma) = 0.5$ GeV/c, the reconstruction efficiency of the converted photons is 0.01% while for $p_T(\gamma) = 4$ GeV/c it is about 1%. Therefore a Monte Carlo sample of a considerable size is needed for a proper calculation of the ratio $\varepsilon_1/\varepsilon_2$. The statistical uncertainty on $\varepsilon_1/\varepsilon_2$ recorded in Table 5.4, from the limited simulation sample size is accounted as a systematic uncertainty and their values are reported in Table 5.7.

5.4.3 Choice of Input $p_T(\chi_c)$ Spectrum

The p_T spectrum used by nature to produce χ_{c1} and χ_{c2} is unknown. We have to rely on reasonable assumptions. Fortunately, as we will explain in the following, the value $\varepsilon_1/\varepsilon_2$ is stable within a few percent even for extreme variations of input p_T spectrum.

$p_T^{J\psi}$ [GeV/c]	$7-9$	$9-11$	$11-13$	$13-16$	$16-20$	$20-25$
Source of uncertainty	**Relative uncertainty (%)**					
Background Shape	1.4	1.5	0.9	1.2	1.8	2.4
Simulation Sample Size	2.6	2.0	2.2	2.4	3.1	4.8
Signal Shape	1.4	3.0	1.1	1.5	1.6	2.2
Choice of $p_T(\chi_c)$ spectrum	4.5	3.7	2.9	1.9	0.6	1.1
Total uncertainty	5.5	5.4	3.9	3.6	4.0	5.9

Table 5.7: Relative systematic uncertainties on R_p for different ranges of J/ψ transverse momentum from different sources and the total uncertainty

We used the ψ' p_T spectrum to produce χ_{c1} and χ_{c2} states using PYTHIA particle gun. We compared the values of $\varepsilon_1/\varepsilon_2$ obtained with the J/ψ and ψ' spectrum and found them to be statistically compatible except in one p_T bin. To get a flavor of the sensitivity of $\varepsilon_1/\varepsilon_2$ to more radically different input $p_T(\chi_c)$ distributions, we used the particle gun with a flat spectrum. The flat spectrum can in fact be considered the extreme scenario with respect to the rapidly falling functions which characterize the production of the states we are considering. The relative differences between the ψ' spectrum and the flat spectrum vary between 2% and 7% in the various bins of $p_T(J/\psi)$. The value of the relative difference in the whole range $p_T(J/\psi) \in [7, 25]$ is 1%. We use the comparison between flat

$p_T^{J\psi}$ [GeV/c]	ψ'	J/ψ	flat
7.0-9.0	0.903 ± 0.023	0.910 ± 0.022	0.963 ± 0.027
9.0-11.0	0.935 ± 0.019	0.924 ± 0.018	0.956 ± 0.018
11.0-13.0	0.945 ± 0.021	0.973 ± 0.021	0.964 ± 0.018
13.0-16.0	0.917 ± 0.022	0.926 ± 0.023	0.987 ± 0.018
16.0-20.0	0.981 ± 0.031	0.899 ± 0.028	0.961 ± 0.020
20.0-25.0	1.028 ± 0.049	1.022 ± 0.046	1.004 ± 0.026

Table 5.8: The values of $\varepsilon_1/\varepsilon_2$ for different choices of input $p_T(\chi_c)$spectrum

spectrum and ψ' spectrum to evaluate the systematic error associated to the choice of input p_T spectrum. To do so, we fit the values of $\varepsilon_1/\varepsilon_2$ obtained with the flat case and ψ' case with a straight line, and we quote as relative systematic error the relative difference between the fit function at any given value of $p_T(J/\psi)$. This

procedure is illustrated in Fig.16. The results are reported in Table 5.8. A further choice for the input spectrum that we have investigated is that of the reconstructed J/ψ spectrum. This has the advantage of matching the detector trigger and acceptance, and therefore maximize the Monte Carlo yield of reconstructible χ_c candidates, but is biased by a sharp drop around 8 GeV due to the acceptance itself, which results in an incomplete coverage of the phase space as discussed above. A comparison of $\varepsilon_1/\varepsilon_2$ for the various choices of input p_T spectrum is available in Table 5.8.

Tracker Material

Since the analysis relies on photon conversions, the effect of a possible incorrect simulation of the tracker detector material is estimated. Two modified material scenarios, i.e., special detector geometries prepared for this purpose, in which the total mass of the silicon tracker varies by up to 5% from the reference geometry, are used to produce new MC simulation samples [59]. With these models, local variations of the radiation length with respect to the reference simulation can be as large as +8% and -3%. No significant difference in the ratio of efficiencies is observed and the corresponding systematic uncertainty is taken to be negligible.

5.4.4 Pileup

Another possible systematic effect might come from pileup. The 2011 run was characterized by different periods with increasing instantaneous luminosity, leading to a different average number of primary vertices per bunch crossing. The stability of our analysis as a function of the number of primary vertices in the event has been investigated.

The 2011 data is divided into two periods, 2011A and 2011B. The number of primary vertices for each periods, 2011A and 2011B, is shown in Figure 5.16. For 2011A period most of the events have on average six primary vertices, for 2011B period the average number of vertices is nine and they are distributed in the z direction with spread of 6 cm. We have studied two different cases for pileup studies (Table 5.9).

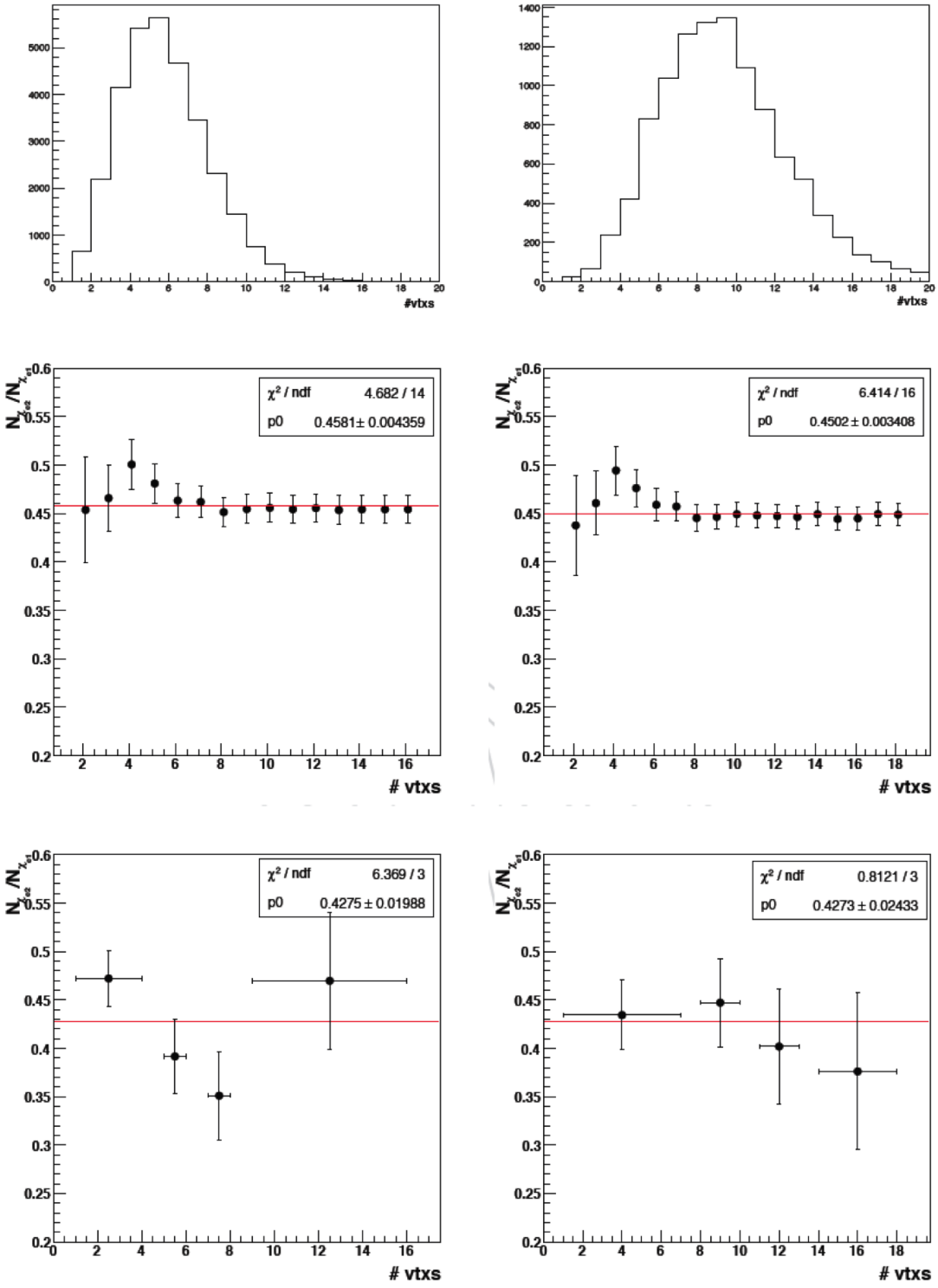

Figure 5.16: pileup

Run 2011A	
Case 1	[1-2], [1-3], [1-4], [1-5] [1-6], [1-7], [1-8], [1-9] [1-10], [1-11], [1-12], [1-13] [1-14], [1-15], [1-16]
Case 2	[1-4], [5-6], [7-8], [9-16]
Run 2011B	
Case 1	[1-2], [1-3], [1-4], [1-5] [1-6], [1-7], [1-8], [1-9] [1-10], [1-11], [1-12], [1-13] [1-14], [1-15], [1-16], [1-17], [1-18]
Case 2	[1-4], [5-6], [7-9], [10-18]

Table 5.9: Pileup

- **Case1:** We calculate the ratio $N_{\chi_{c2}}/N_{\chi_{c1}}$ in bins up to a given number of vertices like [1,2], [1,4], É, [1,16]. The ratio of $N_{\chi_{c2}}/N_{\chi_{c1}}$ for all bins up to a given number converges to the value of $N_{\chi_{c2}}/N_{\chi_{c1}}$ obtained with the maximum number of primary vertices observed in data, where the fluctuations in the first bin for Run2011A are due to low statistics (Figure 5.16).

- **Case2:** We also studied the case for individual bins of number of vertices like [1-4], [5-6], [7-8], [9-16] and fitted with the straight line as shown in Figure 5.16.

The maximum deviation from the straight line is statistically not significant and it is quantitatively measured by the corresponding p value of the χ^2 distribution. For 2011A period it is p = 0.99(Case 1)/0.09(Case 2) and for 2011B period it is p = 1(Case 1)/0.84(Case 2). The measured ratio $N_{\chi_{c2}}/N_{\chi_{c1}}$ is found to be constant as a function of the number of primary vertices in the event, within the statistical uncertainties. Thus, no systematic uncertainty due to pileup is included in the final results.

5.4.5 χ_c Polarization

Polarization of a particle depends on total angular momentum **J** of a particle. There can be 2J+1 states with J_z values ranging from -J to +J. Polarization of particles can be studied using their angular distributions [61, 65]. For case of

J=1 as is the case for χ_c (or a photon) there can be transverse ($J_z = \pm 1$) and longitudinal ($J_z = 0$) polarization.

The angular distributions, $W(\theta, \theta', \phi')$, varies with the choice of the coordinate system. There are four different frames used to study polarization.

- Helicity axis (HX): quarkonium momentum direction
- Gottfried-Jackson axis (GJ): direction of one or the other beam
- Collins-Soper axis (CS): average of the two beam directions [60]
- Perpendicular helicity axis (PX): perpendicular to CS

The polarization of the χ_{c1} and χ_{c2} is unknown and another possible source of uncertainty. The different angular distribution of the photon may affect the photon p_T distribution. In order to study how $\varepsilon_1/\varepsilon_2$ varies with different polarization scenarios, we have applied a reweighing procedure to our particle-gun Monte Carlo. The particle gun generates decays in which both the χ_c and the J/ψ are emitted isotropically, and therefore the angular distributions of the photon (J/ψ) in the χ_c rest frame and of the μ in the J/ψ rest frame are flat. We use the theoretical angular distribution as a weight to our Monte Carlo events, and therefore obtain χ_c's according to the desired angular distribution.

The ratio $\varepsilon_1/\varepsilon_2$ is measured for the χ_{c1} unpolarized or with helicity 0,$\pm$1 in combination with the χ_{c2} unpolarized or with helicity 0 or $\pm$2. Table 5.10 and Table 5.11 reports the values of $\varepsilon_1/\varepsilon_2$ for the various polarization cases in each p_T bin for helicities defined within the *helicity frame* and *Collins-Soper frame*, respectively, relative to the unpolarized case. The usual kinematical cuts, $|y(J/\psi)| < 1.0$ and $p_T(\gamma) > 0.5 GeV/c$, have been applied. These tables therefore provide the correction factor that would be applied to the default measurement of $\varepsilon_1/\varepsilon_2$ in each polarization scenario and each p_T range.

It might be noted that the largest positive/negative deviations from the unpolarized case are obtained for the $(\pm 1, \pm 2)/\ (0, 0)$ case in the helicity frame and for the $(0, 0)/(\pm 1, \pm 2)$ case in the Collins-Soper frame. This is expected, since the two frames are almost orthogonal at mid rapidity.

$\mathscr{P}(h_{\chi_{c1}},h_{\chi_{c1}})$	$p_T^{J\psi}$ [GeV/c]					
	$7-9$	$9-11$	$11-13$	$13-16$	$16-20$	$20-25$
$\mathscr{P}(Unpol,0)$	0.886	0.871	0.855	0.857	0.847	0.862
$\mathscr{P}(Unpol,\pm1)$	0.920	0.935	0.938	0.930	0.945	0.935
$\mathscr{P}(Unpol,\pm2)$	1.203	1.204	1.212	1.201	1.201	1.172
$\mathscr{P}(0,Unpol)$	0.832	0.839	0.848	0.848	0.854	0.861
$\mathscr{P}(\pm1,Unpol)$	1.077	1.072	1.068	1.068	1.067	1.064
$\mathscr{P}(0,0)$	0.737	0.730	0.725	0.727	0.723	0.743
$\mathscr{P}(0,\pm1)$	0.765	0.783	0.795	0.788	0.806	0.805
$\mathscr{P}(0,\pm2)$	1.001	1.010	1.028	1.019	1.025	1.010
$\mathscr{P}(\pm1,0)$	0.954	0.933	0.913	0.916	0.904	0.917
$\mathscr{P}(\pm1,\pm1)$	0.991	1.003	1.001	0.993	1.008	0.995
$\mathscr{P}(\pm1,\pm2)$	1.295	1.291	1.294	1.283	1.281	1.247

Table 5.10: The efficiency ratio $\varepsilon_1/\varepsilon_2$ for different polarization scenarios in which the χ_{c1} is either unpolarized or has helicity $m_{\chi_c1} = 0, \pm 1$ and the m_{χ_c2} is either unpolarized or has helicity $m_{\chi_c1} = 0, \pm 2$ in the helicity frame, relative to the unpolarized case

5.5 Results

The results of the measurement of the ratio R_p and of the ratio of the χ_{c2} to χ_{c1} prompt production cross sections for the kinematic range $p_T(\gamma) > 0.5GeV/c$ and $|y(J/\psi)| < 1.0$ are reported in Tables 5.12 and 5.13, respectively, for different ranges of $p_T(J/\psi)$ [67]. The first uncertainty is statistical, the second is systematic, and the third comes from the uncertainty in the branching fractions in the measurement of the cross section ratio. Separate columns are dedicated to the uncertainty derived from the extreme polarization scenarios in the helicity and Collins-Soper frames, by choosing from Tables 5.10 and 5.11 the scenarios that give the largest variations relative to the unpolarized case. These correspond to $(m_{\chi_{c1}},(m_{\chi_{c2}})) = (\pm1,\pm2) and ((m_{\chi_{c1}},(m_{\chi_{c2}})) = (0,0)$ for both the helicity and Collins-Soper frames. Figure 5.17 displays the results as a function of the J/ψ transverse momentum for the hypothesis of unpolarized production [66].

The error bars represent the statistical uncertainties and the green bands the systematic uncertainties. Measurement of the ratio of the prompt χ_{c2} to χ_{c1} cross sections includes both directly produced χ_c mesons and indirectly produced ones

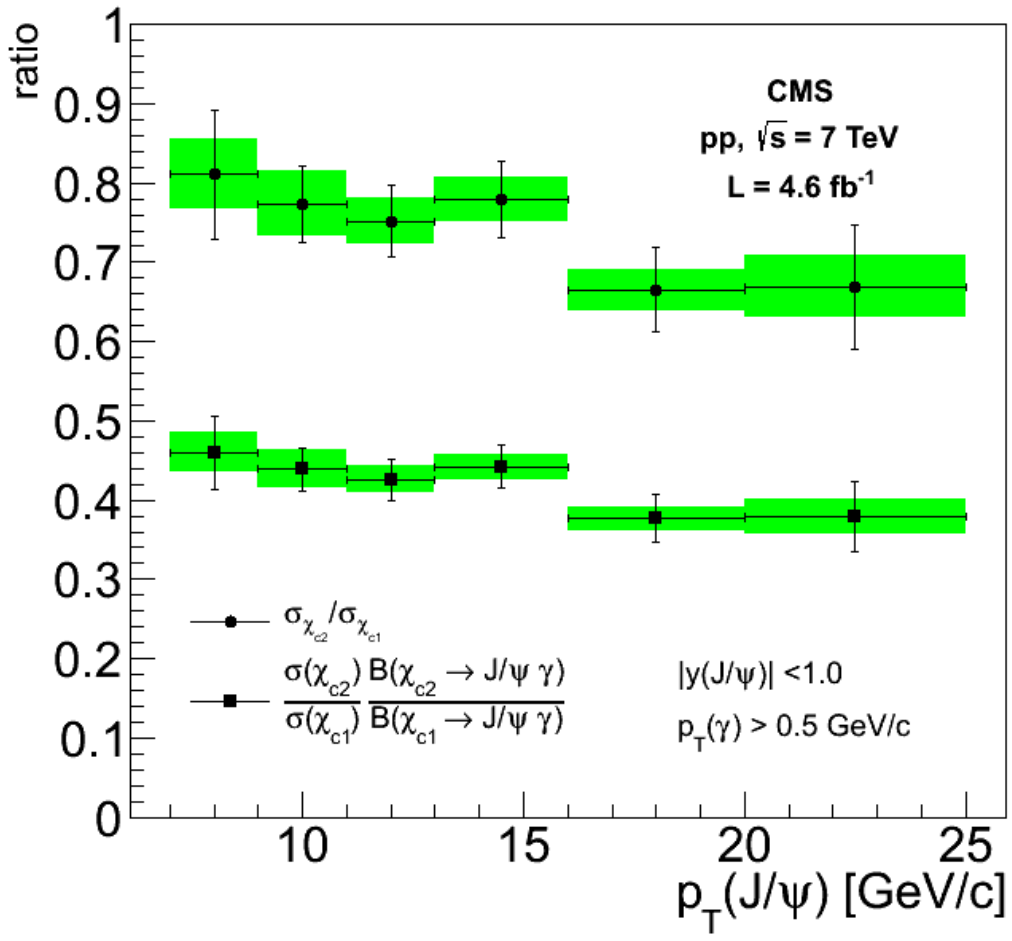

Figure 5.17: Ratio of the χ_{c2} to χ_{c1} production cross sections (circles) and ratio of the cross sections times the branching fractions to $J/\psi\ \gamma$ (squares) as a function of the J/ψ transverse momentum with the hypothesis of unpolarized production. The error bars correspond to the statistical uncertainties and the green band corresponds to the systematic uncertainties. For the cross section ratios, the 5.6% uncertainty from the branching fractions is not included.

$\mathscr{P}(h_{\chi_{c1}},h_{\chi_{c1}})$	$p_T^{J\psi}$ [GeV/c]					
	$7-9$	$9-11$	$11-13$	$13-16$	$16-20$	$20-25$
$\mathscr{P}(Unpol,0)$	1.040	1.063	1.076	1.075	1.084	1.077
$\mathscr{P}(Unpol,\pm1)$	1.016	1.035	1.048	1.033	1.056	1.037
$\mathscr{P}(Unpol,\pm2)$	0.968	0.948	0.930	0.933	0.921	0.925
$\mathscr{P}(0,Unpol)$	1.039	1.053	1.059	1.067	1.069	1.062
$\mathscr{P}(\pm1,Unpol)$	0.980	0.972	0.969	0.965	0.964	0.968
$\mathscr{P}(0,0)$	1.081	1.119	1.139	1.147	1.157	1.144
$\mathscr{P}(0,\pm1)$	1.056	1.092	1.108	1.101	1.127	1.102
$\mathscr{P}(0,\pm2)$	1.006	0.998	0.985	0.995	0.984	0.982
$\mathscr{P}(\pm1,0)$	1.019	1.033	1.042	1.037	1.045	1.042
$\mathscr{P}(\pm1,\pm1)$	0.995	1.005	1.016	0.997	1.019	1.003
$\mathscr{P}(\pm1,\pm2)$	0.949	0.921	0.902	0.900	0.888	0.895

Table 5.11: The values of $\varepsilon_1/\varepsilon_2$ for different polarization scenarios in the Collins-Soper frame, relative to the unpolarized case

from the decays of intermediate states. To convert our result to the ratio of directly produced χ_{c2} to χ_{c1} mesons requires knowledge of the amount of feed-down from all possible short-lived intermediate states that have a decay mode into χ_{c2} or χ_{c1}. The largest known such feed-down contribution comes from the ψ'. Using the measured prompt J/ψ and ψ' cross sections in $p\bar{p}$ collisions at 7 TeV [53], the branching fractions for the decays $\psi' \to \chi_{c1,2}$, and assuming the same fractional χ_c contribution to the total prompt J/ψ production cross section as measured in $p\bar{p}$ collisions at 1.96 TeV [50], we estimate that roughly 5% of both our prompt χ_{c1} and χ_{c2} samples come from ψ' decays. The correction in going from the prompt ratio to the direct ratio is about 1%. In comparing our results with the theoretical predictions described below, we have not attempted to correct for this effect since the uncertainties on the fractions are difficult to estimate, the correction is much smaller than the statistical and systematic uncertainties, and our conclusions on the comparisons with the theoretical predictions would not be altered by a correction of this magnitude.

5.6 Comparison with Theory

We compare our results with theoretical predictions derived from the k_T-factorization [63] and NRQCD [64] calculations in Figure 5.18 and 5.19. The k_T-factorization approach predicts that both χ_{c1} and χ_{c2} are produced in an almost pure helicity-zero state in the helicity frame. Therefore, in our comparison, we apply the corresponding correction on the ratio of efficiencies from Table 4, amounting to a factor of 0.73, almost independent of p_T. The theoretical calculation is given in the same kinematic range ($p_T(\gamma) > 0.5GeV/c, |y(J/\psi)| < 1.0$) as our measurement. There is no information about the χ_c polarization from the NRQCD calculations, so we use the ratio of efficiencies estimated in the unpolarized case for our comparison.

The prediction is given in the kinematic range ($p_T(\gamma) > 0GeV/c, |y(J/\psi)| < 1.0$). We use the same MC simulation described in Section 5.2 to derive the small correction factor (ranging from 0.98 to 1.02 depending on p_T, with uncertainties from 1 to 4 %) needed to extrapolate the phase space of our measurement to the one used for the theoretical calculation. The uncertainty in the correction factor stemming from the assumption of the χ_c transverse momentum distribution is added as a systematic uncertainty. The values of R_p after extrapolation are shown in Table 5.14. The comparison of our measurements with the k_T-factorization and NRQCD predictions are shown in Figure 5.18 and Figure 5.19, respectively. The k_T-factorization prediction agrees well with the trend of R_p versus transverse momentum of the J/ψ, but with a global normalization that is higher by about a factor two with respect to our measurement. It is worth noting that this calculation assumes the same wave function for the χ_{c1} and the χ_{c2}. On the other hand, the NRQCD prediction is compatible with our results within the experimental and theoretical uncertainties, though, since predictions for χ_{c1} or χ_{c2} polarizations were not provided, the level of agreement can vary considerably [66].

A direct comparison of our results with previous measurements, in particular from [39] and [18], is not straightforward, because of the different conditions under which they were carried out. Specifically, there are differences in the kinematical phase space considered and, in the case of [39], in the initial-state colliding beams and center-of-mass energy used. However, with these caveats, a direct comparison

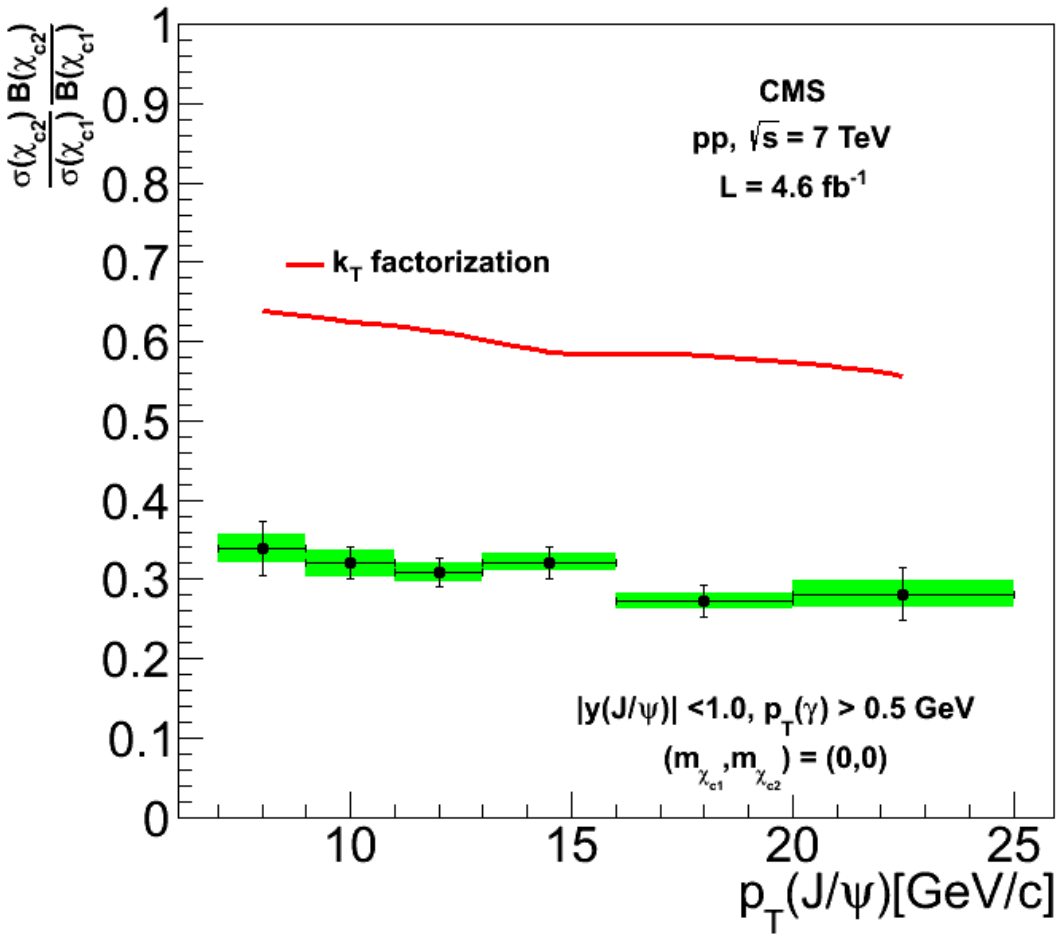

Figure 5.18: Comparison of the measured $\mathscr{B}(\chi_{c2})\sigma(\chi_{c2})/\mathscr{B}(\chi_{c1})\sigma(\chi_{c1})$ values with theoretical predictions from the k_T-factorization calculations (solid red lines). The error bars and bands show the experimental statistical and systematic uncertainties, respectively. The measurements use an acceptance correction assuming zero helicity for the χ_c , as predicted by the k_T-factorization model

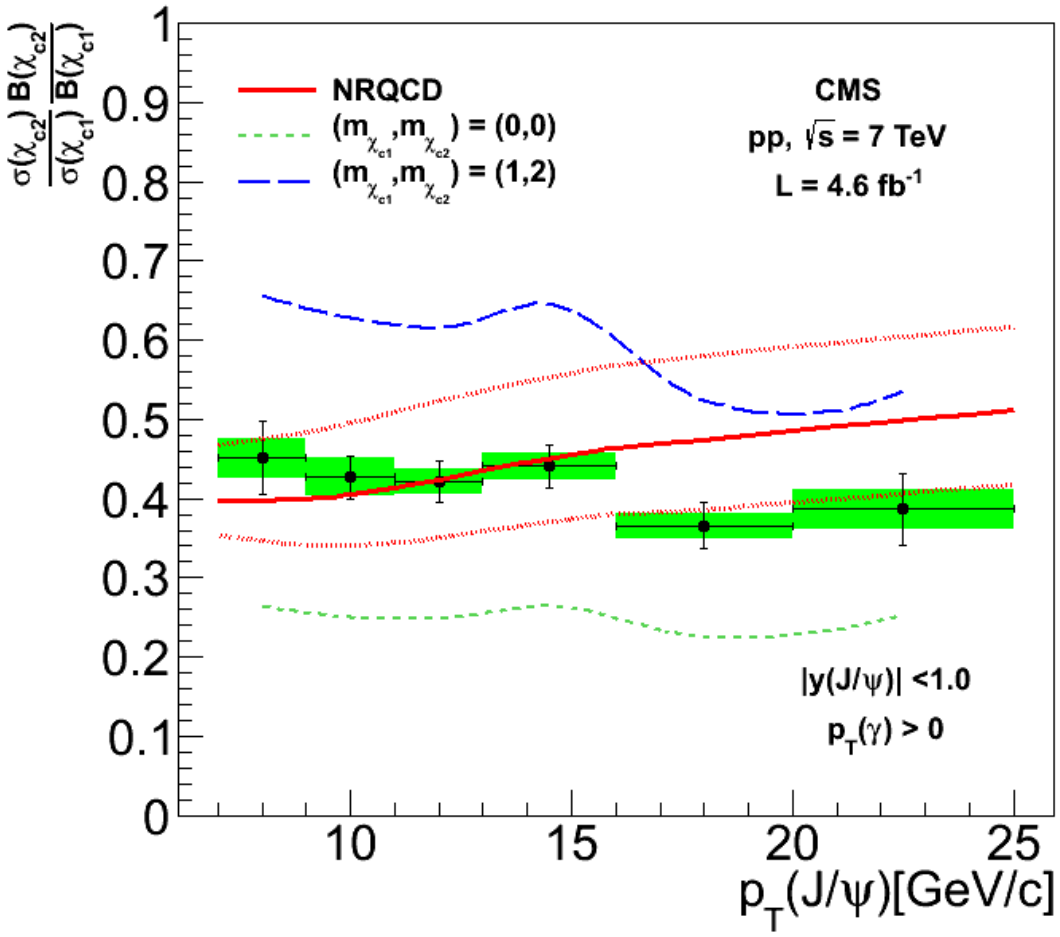

Figure 5.19: Comparison of the measured $\mathscr{B}(\chi_{c2})\sigma(\chi_{c2})/\mathscr{B}(\chi_{c1})\sigma(\chi_{c1})$ values with theoretical predictions from the NRQCD calculations (solid red lines). The measurements are corrected to match the kinematic range used in the NRQCD calculation and assume the χ_c are produced unpolarized. The measurements assuming two different extreme polarization scenarios are shown by the long-dashed and short-dashed lines in the plot. The 1-standard-deviation uncertainties in the NRQCD prediction, originating from uncertainties in the color-octet matrix elements, are displayed as the dotted lines

shows that the three results are compatible within their uncertainties. In particular, all three results confirm the trend of a decreasing ratio of χ_{c2} to χ_{c1} production cross sections as a function of $p_T(J/\psi)$, under the assumption that the χ_{c2} and χ_{c1} polarizations do not depend on $p_T(J/\psi)$.

$p_T^{J\psi}$ $[GeV/c]$	$\mathscr{B}(\chi_{c2})\sigma(\chi_{c2})/\mathscr{B}(\chi_{c1})\sigma(\chi_{c1})$	Pol. CS	Pol. HX
7.0-9.0	0.460± 0.044(stat) ± 0.025(sys)	$^{+0.136}_{-0.121}$	$^{+0.037}_{-0.023}$
9.0-11.0	0.439± 0.025(stat) ± 0.024(sys)	$^{+0.128}_{-0.119}$	$^{+0.052}_{-0.035}$
11.0-13.0	0.426± 0.024(stat) ± 0.017(sys)	$^{+0.125}_{-0.117}$	$^{+0.059}_{-0.042}$
13.0-16.0	0.442± 0.025(stat) ± 0.016(sys)	$^{+0.125}_{-0.121}$	$^{+0.065}_{-0.044}$
16.0-20.0	0.377± 0.028(stat) ± 0.015(sys)	$^{+0.106}_{-0.104}$	$^{+0.059}_{-0.042}$
20.0-25.0	0.379± 0.041(stat) ± 0.022(sys)	$^{+0.094}_{-0.097}$	$^{+0.055}_{-0.040}$

Table 5.12: The results of our measurement of $\frac{\mathscr{B}(\chi_{c2})\sigma(\chi_{c2})}{\mathscr{B}(\chi_{c1})\sigma(\chi_{c1})}$ for the various values of $p_T^{J/\psi}$. The first error is statistical, the second is systematic. Two separate columns report the uncertainty deriving from the extreme polarization scenarios in the *Collins-Soper frame*, and the *Helicity frame*

$p_T^{J\psi}$ [GeV/c]	$\sigma(\chi_{c2})/\sigma(\chi_{c1})$	Pol. CS	Pol. HX
7.0-9.0	0.811±0.078 (stat) ± 0.045 (sys) ± 0.046(BR)	$^{+0.239}_{-0.313}$	$^{+0.066}_{-0.041}$
9.0-11.0	0.774±0.044 (stat) ± 0.042 (sys) ± 0.044(BR)	$^{+0.225}_{-0.209}$	$^{+0.092}_{-0.061}$
11.0-13.0	0.752±0.042 (stat) ± 0.029 (sys) ± 0.043(BR)	$^{+0.221}_{-0.207}$	$^{+0.105}_{-0.074}$
13.0-16.0	0.780±0.044 (stat) ± 0.028 (sys) ± 0.044(BR)	$^{+0.221}_{-0.213}$	$^{+0.115}_{-0.078}$
16.0-20.0	0.665±0.049 (stat) ± 0.027 (sys) ± 0.038(BR)	$^{+0.187}_{-0.184}$	$^{+0.104}_{-0.074}$
20.0-25.0	0.669±0.072 (stat) ± 0.039 (sys) ± 0.038(BR)	$^{+0.165}_{-0.172}$	$^{+0.096}_{-0.070}$

Table 5.13: The results of our measurement of $\frac{\sigma(\chi_{c2})}{\sigma(\chi_{c1})}$ for the various values of $p_T^{J/\psi}$. The first error is statistical, the second is systematic. Two separate columns report the uncertainty derived from the extreme polarization scenarios in the *Collins-Soper frame*, and the *Helicity frame*

$p_T^{J\psi}$ [GeV/c]	$\mathscr{B}(\chi_{c2})\sigma(\chi_{c2})/\mathscr{B}(\chi_{c1})\sigma(\chi_{c1})$	Polarization
7.0-9.0	0.451± 0.043(stat) ± 0.025(sys)	$^{+0.137}_{-0.153}$
9.0-11.0	0.427± 0.024(stat) ± 0.023(sys)	$^{+0.134}_{-0.144}$
11.0-13.0	0.421± 0.024(stat) ± 0.017(sys)	$^{+0.133}_{-0.142}$
13.0-16.0	0.441± 0.025(stat) ± 0.017(sys)	$^{+0.138}_{-0.143}$
16.0-20.0	0.365± 0.027(stat) ± 0.016(sys)	$^{+0.114}_{-0.115}$
20.0-25.0	0.387± 0.042(stat) ± 0.026(sys)	$^{+0.109}_{-0.105}$

Table 5.14: Measurements of $\mathscr{B}(\chi_{c2})\sigma(\chi_{c2})/\mathscr{B}(\chi_{c1})\sigma(\chi_{c1})$ for the given $p_T(J/\psi)$ ranges after extrapolating the measurement to the kinematic region $p_T(\gamma) > 0$ and assuming unpolarized χ_c production. The first uncertainty is statistical and the second is systematic. The last column reports the largest variations due changes in the assumed χ_c polarizations

Conclusion

In the first part of thesis Commissioning of EndCap RPC is discussed in detail. EndCap RPCs are assembled in Pakistan and are commissioned by Pakistani team during 2008-09. The main purpose of commissioning was to certify that the performance of our detector is still of the same level as during the production and test phases. The RPC systems that have been tested for good performance during commissioning are Gas System, High Voltage System, Low Voltage System, Cooling system, Detector Readout System.

In the second part cross section ratio of χ_{c1} and χ_{c2} is measured for different J/ψ p_T ranges at CMS. The measurement is done using 4.7 fb^{-1} data of CMS collected in 2011. The χ_{c1} and χ_{c2} are reconstructed through their decays into J/ψ and a photon. The J/ψ was reconstructed with two oppositely charged muons detected in the CMS tracker and muon chambers. The photons were reconstructed through conversions in the tracker. An unbinned extended maximum likelihood fit to the data was used to extract the number of χ_{c1} and χ_{c2} candidates. The signal shape of χ_{c1} and χ_{c2} was modeled with a Double Crystal Ball PDF while the χ_{c0} shape was modeled with a Single Crystal Ball PDF. For the combinatorial background a generic PDF which consists of a product of exponential and power law functions was used. Using a Monte Carlo generator, a correction factor to the observed numbers of χ_{c1} and χ_{c2} candidates was calculated to account for detector acceptance and reconstruction efficiency. Several sources of systematic uncertainties were evaluated and their effect on the cross section ratio was estimated. The unknown χ_c polarization represents the biggest source of uncertainty on the measured ratio. Correction coefficients to the ratio were evaluated to account for different χ_{c1} and χ_{c2} polarization states and to allow an easier comparison with theory predictions.

The result was compared with two theory predictions: k_T factorization and NLO Non-Relativistic QCD. None of these models gives a fully satisfactory description of the data [66]. The trend of $\sigma(\chi_{c2})/\sigma(\chi_{c1})$ in data is well described by the k_T factorization approach but the normalization is off by a factor of two. In the k_T factorization calculations, the χ_{c1} and χ_{c2} wave functions are assumed to be identical, following the results of potential model calculations which neglect spin-orbit interactions. A large deviation from the assumption of identical χ_{c1} and χ_{c2} wave functions may explain why the $p_T(J/\psi)$ dependence of the ratio is the same and the difference is a global scale factor. Similarly to CDF, we observe a discrepancy of the same order with NLO NRQCD calculations.

Moreover, both CDF and CMS experiments observe a decrease of the χ_{c2}/χ_{c1} production ratio while NLO NRQCD predicts an increase of the χ_{c2}/χ_{c1} production ratio with J/ψ p_T . Higher order corrections in the perturbative calculations of the formation of the $c\bar{c}$ pair are not expected to reduce this discrepancy with experimental results at high $p_T(J/\psi)$. This difference can only be explained with non-perturbative contributions related to the binding of the $c\bar{c}$ pair into charmonium.

A proper comparison between the NLO NRQCD prediction and the measurement depends on the predicted polarization of χ_c, which is not known. For example, if the predicted polarization were to increase the measured production ratio, the agreement between theory and measurement would be better at high $p_T(J/\psi)$. Hence, a measurement of the χ_c polarization is crucial to interpret the existing results within the framework of NRQCD. This measurement is among the most precise measurements of the χ_c production cross section ratio made in hadron collisions which extends the explored range to high p_T values of the J/ψ.

Bibliography

[1] Introduction to elementary particles, by David Griffiths

[2] Discovery of a Narrow Resonance in e^+e^- Annihilation, Phys. Rev. Lett. 33, 1406-1408 (1974)

[3] The Discovery of the B quark at Fermilab in 1977: The Experiment coordinator's story, FERMILAB-Conf-97/432

[4] M.B. Voloshin, Charmonium, Prog.Part.Nucl.Phys.61:455-511, 2008

[5] Producing Heavy Quark Flavors in Hadronic Collisions: A Test of Quantum Chromodynamics, Phys.Lett. B67 (1977) 217

[6] CVC for Gluons and Hadroproduction of Quark Flavors, Phys.Lett. B69 (1977) 105

[7] J .F. Amundson, O. J. P. Eboli, E. M. Gregores, F. Halzen, Charged particle multiplicity in e^+e^- interactions at $\sqrt{s}$ =130 GeV, Phys. Lett. B 372 (1996)127

[8] J.F Amundsonet al., Quantitative tests of color evaporation: charmonium production, Phys. Lett. B 390 (1997) 323

[9] Jean-philippe Lansberg, J/ψ, ψ' and υ production at hadron collider. A Review, Int. J. Mod. Phys. A, 21, 3857 (2006)

[10] Production of heavy quarks and heavy quarkonia, arXiv:hep-ph/9504242-v2

[11] R. Baier and R. Ruckl, Z. Phys. C 19 (1983) 251.

[12] R. Gastmans, W. Troost and T.T. Wu, Nucl. Phys.B291(1987) 731.

[13] B. Humpert, Phys. Lett. B184 (1987) 105.

[14] G.A. Schuler, CERN-TH.7170/94 (1994)

[15] S. Catani et. al, Phys. Lett. B242 (1990) 97.

[16] J.C. Collins et. al, Nucl. Phys. B360 (1991) 3.

[17] M.G. Ryskin et. al, Phys. Atom. Nucl. 64 (2001) 1995.

[18] LHCb Collaboration, Measurement of the cross-section ratio $\sigma(\chi_{c2})/\sigma(\chi_{c1})$ for prompt χ_c production at $\sqrt{s} = 7$ TeV, Phys. Lett. B 714, 215 (2012)

[19] Lyndon Evans and Philip Bryant, LHC Machine, J. Instrum. 3, S08001 (2008).

[20] CMS Collaboration, The CMS experiment at the CERN LHC, J. Instrum. 3, S08004 (2008).

[21] ATLAS Collaboration, The ATLAS experiment at the CERN Large Hadron Collider, J. Instrum. 3, S08003 (2008).

[22] LHCb Collaboration, The LHCb Detector at the CERN LHC, J. Instrum. 3, S08005 (2008).

[23] ALICE Collaboration, The CMS experiment at the CERN LHC, J. Instrum. 3, S08002 (2008).

[24] Detector Performance and Software, CERN/LHCC 2006-001

[25] CMS Collaboration, The Compact Muon Solenoid Technical Proposal, CERN/LHCC 94-38, LHCC/P1, 15 December 1994.

[26] CMS Collaboration, CMS Design Team, CMS: The Magnet Project Technical Design Report, CERN/LHCC 97-10, CMS TDR 1, 2 May 1997

[27] CMS Collaboration, CMS: The Tracker Project Technical Design Report, CERN/LHCC 98-06, CMS TDR 5, 15 April 1998

[28] CMS Collaboration, CMS: The Electromagnetic Calorimeter Project Technical Design Report, CERN/LHCC 97-33, CMS TDR 4, 15 December 1997

[29] CMS Collaboration, CMS: The Hadron Calorimeter Project Technical Design Report, CERN/LHCC 97-31, CMS TDR 2, 20 June 1997

[30] CMS Collaboration, CMS: The Muon Project Technical Design Report, CERN/LHCC 97-32, CMS TDR 3, 15 December 1997

[31] Wrochna, G, The muon system of the CMS detector at LHC, Nuclear Inst. and Methods in Physics Research, A, 19940421

[32] https://twiki.cern.ch/twiki/bin/view/CMSPublic/LumiPublicResults2011

[33] CMS Collaboration, "Muon Project", CERN/LHCC 94-138, 15 December 1997.

[34] Polese Giovanni, The detector control systems for the CMS Resistive Plate Chamber, Nuclear Science Symposium Conference Record, 2008. NSS 08. IEEE.10.1109/NSSMIC.2008.4775035 (2008)

[35] http://www.caen.it/csite/HomePage.jsp

[36] N. Brambilla et al., Heavy Quarkonium Physics, CERN Yellow Report CERN-2005-005 (2005).

[37] CDF Collaboration, Inclusive J/ψ, $\psi(2S)$ and b quark production in $p\bar{p}$ collisions at $\sqrt{s} = 1.8$ TeV, Phys. Rev. Lett. 69, 3704(1992).

[38] CDF Collaboration, J/ψ, $\psi(2S)$ production in pp collisions at $\sqrt{s} = 1.8$ TeV, Phys. Rev. Lett. 79, 572 (1997).

[39] M. Kramer, Quarkonium production at high-energy colliders, Prog. Part. Nucl. Phys. 47, 141 (2001)

[40] CDF Collaboration, Measurement of $\sigma_{\chi_{c2}} B(\chi_{c2} \to J/\psi\gamma$ / $\sigma_{\chi_{c1}} B(\chi_{c1} \to J/\psi\gamma$ in $p\bar{p}$ Collisions at $\sqrt{s} = 1.96$ TeV, Phys. Rev. Lett. 98, 232001 (2007)

[41] R. Li and J.-X.Wang, Next-to-Leading-Order QCD corrections to J/ψ (Upsilon)+gamma production at the LHC, Phys. Lett. B672 (2009) 51-55

[42] Y.-Q. Ma, K. Wang, and K.-T. Chao, QCD radiative corrections to χ_{cJ} production at hadron colliders, Phys. Rev. D 83 (Jun, 2011) 111503.

[43] Widl Edmund, Fruhwirth R, Adam Wolfgang, A Kalman Filter for Track-based Alignment, CMS-NOTE-2006-022

[44] CMS Collaboration, Performance of CMS muon reconstruction in cosmic-ray events, J. Instrum. 5, T03022 (2010)

[45] CMS Collaboration, Tracking and vertexing results from first collisions, CMS physics analysis summary CMS-PAS-TRK-10-001(2010)

[46] CMS Collaboration, CMS tracking performance results from early LHC operation, Eur. Phys. J. C 70, 1165 (2010)

[47] CMS Collaboration, Studies of tracker material in the CMS detector, CMS physics analysis summary CMS-PAS-TRK-10-003 (2010)

[48] CMS Collaboration, Prompt and non-prompt J/ψ production in pp collisions at $\sqrt{s} = 7$ TeV, Eur. Phys. J. C 71, 1575 (2011)

[49] J. Beringer et al. (Particle Data Group), Review of particle physics, Phys. Rev. D 86, 010001 (2012).

[50] CDF Collaboration, Production of J/ψ mesons from χ_c meson decays in pp collisions at $\sqrt{s} = 1.8$ TeV, Phys. Rev. Lett. 79, 578(1997).

[51] M.J. Oreglia, A study of the reactions $\psi' \to \gamma\gamma\psi$, PhD thesis, Stanford University, 1980, SLAC Report SLAC-R-236

[52] T. Sjostrand, S. Mrenna, P. Skands, PYTHIA 6.4 physics and manual, J. High Energy Phys. 05, 026 (2006)

[53] CMS Collaboration, J/ψ, $\psi(2S)$ production in pp collisions at $\sqrt{s} = 7$ TeV, J. High Energy Phys. 02, 011 (2012)

[54] S. Agostinelli et al., GEANT4 a simulation toolkit, Nucl. Instrum. Methods A 506, 250 (2003)

[55] J. Allison et al., GEANT4 developments and applications, IEEE Trans. Nucl. Sci. 53, 270 (2006).

[56] The CMS Collaboration, https://twiki.cern.ch/twiki/bin/view/CMSPublic/SWGuideFastSi

[57] J. Alcaraz, Uncertainties in acceptance calculations with weights, CMS-AN-2010-051.

[58] G. Cerati, G.Sguazzoni, CMS Note 2010/040 (2010).

[59] E. Migliore, G. Sguazzoni, Altered scenarios of the CMS Tracker material for systematic uncertainties studies, Technical Report CMS-NOTE-2010-010, CERN (2010)

[60] J.C. Collins, D.E. Soper, Angular distribution of dileptons in high-energy hadron collisions, Phys. Rev. D 16, 2219 (1977).

[61] P. Faccioli et al., Determination of χ_c and χ_b polarizations from dilepton angular distributions in radiative decays, Phys. Rev. D 83, 096001 (2011)

[62] W. Verkerke et al., Proceedings of the Conference for Computing in High-Energy and Nuclear Physics (CHEP 03), La Jolla, California (2003), arXiv:physics / 0306116 (2003).

[63] S.P. Baranov, $\sigma(\chi_{c1})/\sigma(\chi_{c2})$ ratio in the k_t-factorization approach, Phys. Rev. D 83, 034035 (2011)

[64] Y.-Q. Ma, K.Wang, K.-T. Chao, QCD radiative corrections to χ_{cJ} production at hadron colliders, Phys. Rev. D 83, 111503 (2011)

[65] HERA-B Collaboration, Production of the charmonium states χ_{c1} and χ_{c2} in proton nucleus interactions at $\sqrt{s} = 41.6$ GeV, Phys. Rev. D 79, 012001 (2009)

[66] CMS Collaboration, Measurement of the relative prompt production rate of χ_{c2} and χ_{c1} in pp collisions at $\sqrt{s} = 7TeV$, Eur. Phys. J. C (2012) 72:2251

[67] M. Ahmad, Vasileva Akin, S. Argiro, T. Dahms, A. Degano, D. Giordano, G. Sguazzoni, and E. Usai, Measurement of the ratios $\sigma(pp \to \chi_{c2} + X)/\sigma(pp \to \chi_{c1} + X)$ from radiative decays in $J/\psi + \gamma$ using converted photons, CMS NOTE AN-11-332

Appendix A

Fits to Pythia Monte Carlo particle gun

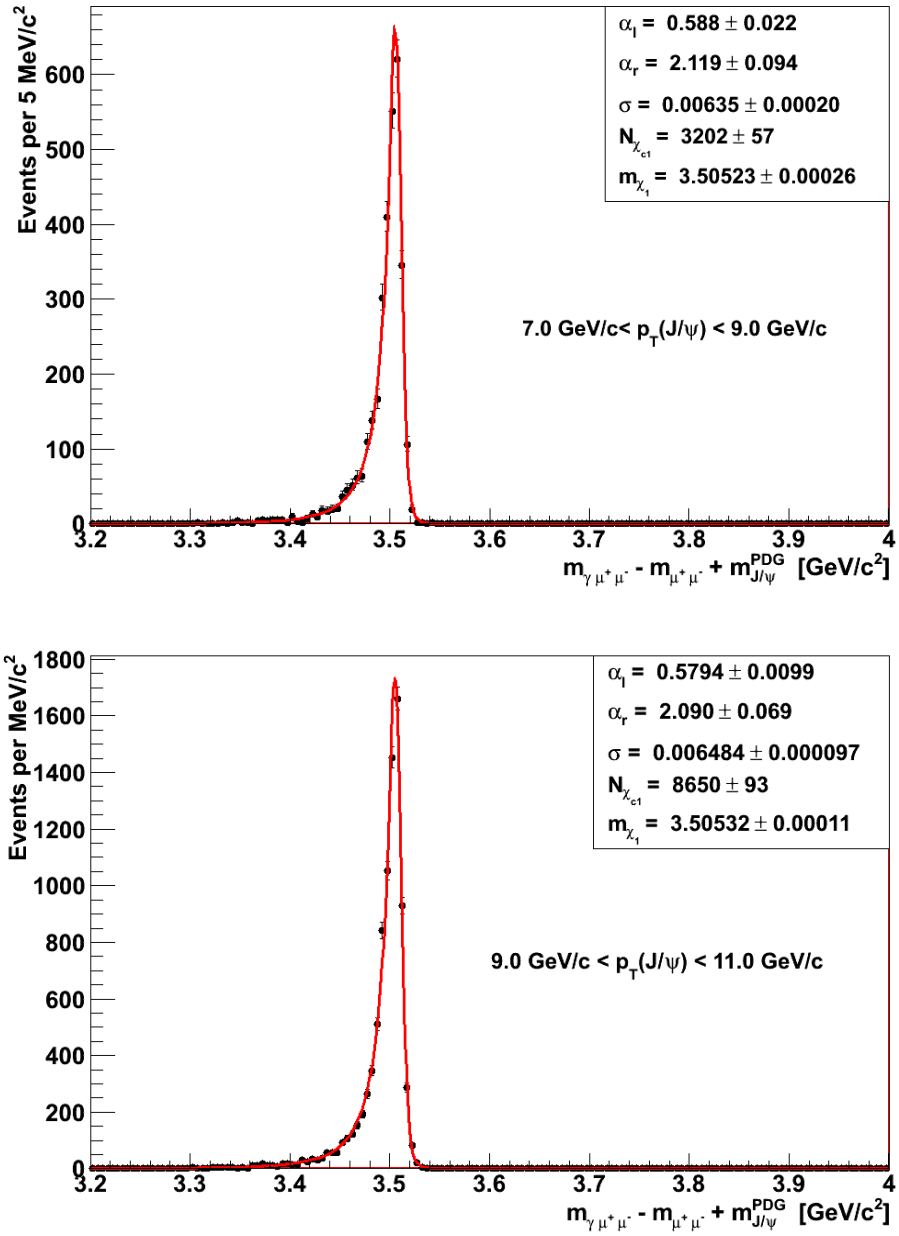

Figure A.1: Double-sided Crystal Ball fits to particle gun Monte Carlo for χ_{c1} candidates for $p_T(J/\psi)$ in [7.0-9.0] GeV/c (top) and [9.0-11.0] GeV/c (bottom).

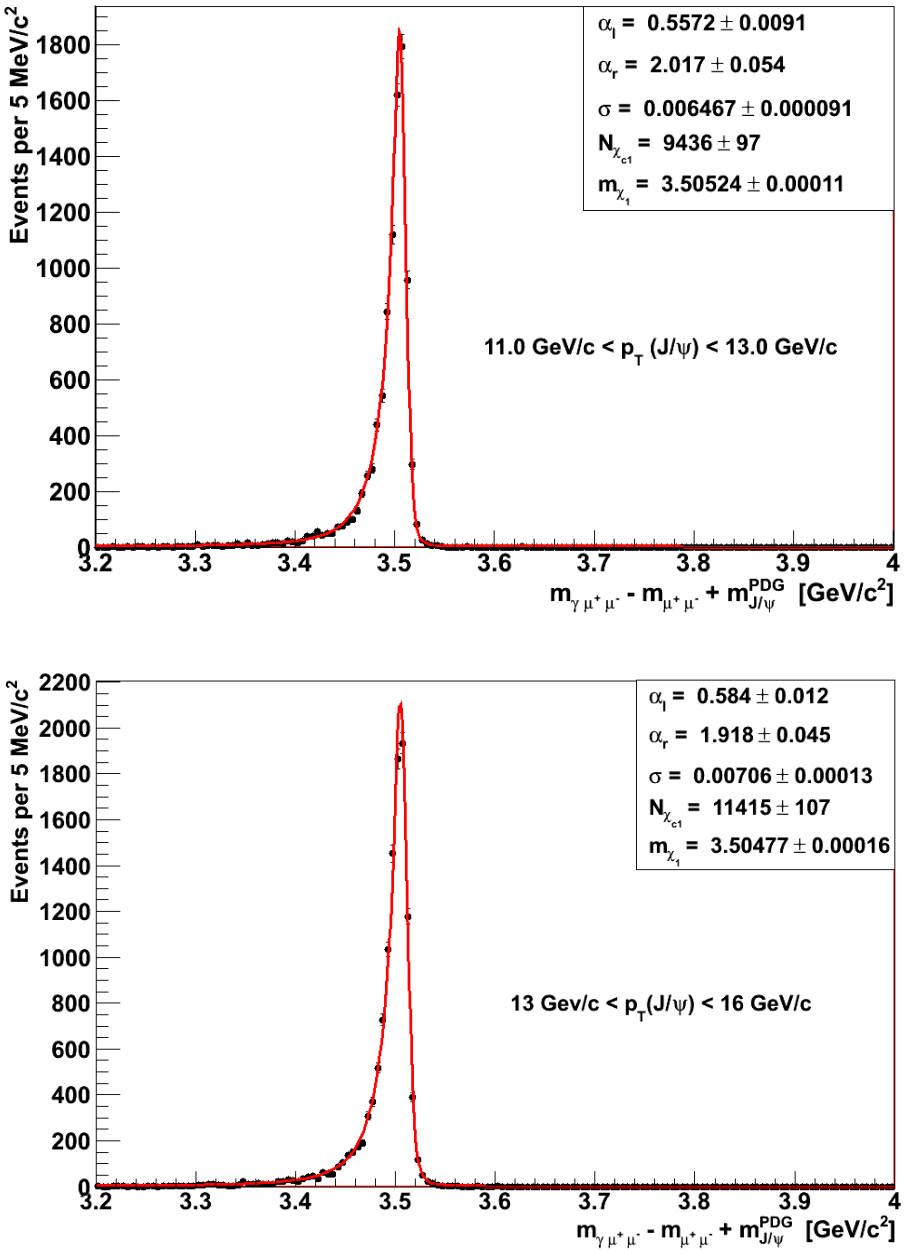

Figure A.2: Double-sided Crystal Ball fits to particle gun Monte Carlo for χ_{c1} candidates for $p_T(J/\psi)$ in [11.0-13.0] GeV/c (top) and [13.0-16.0] GeV/c (bottom).

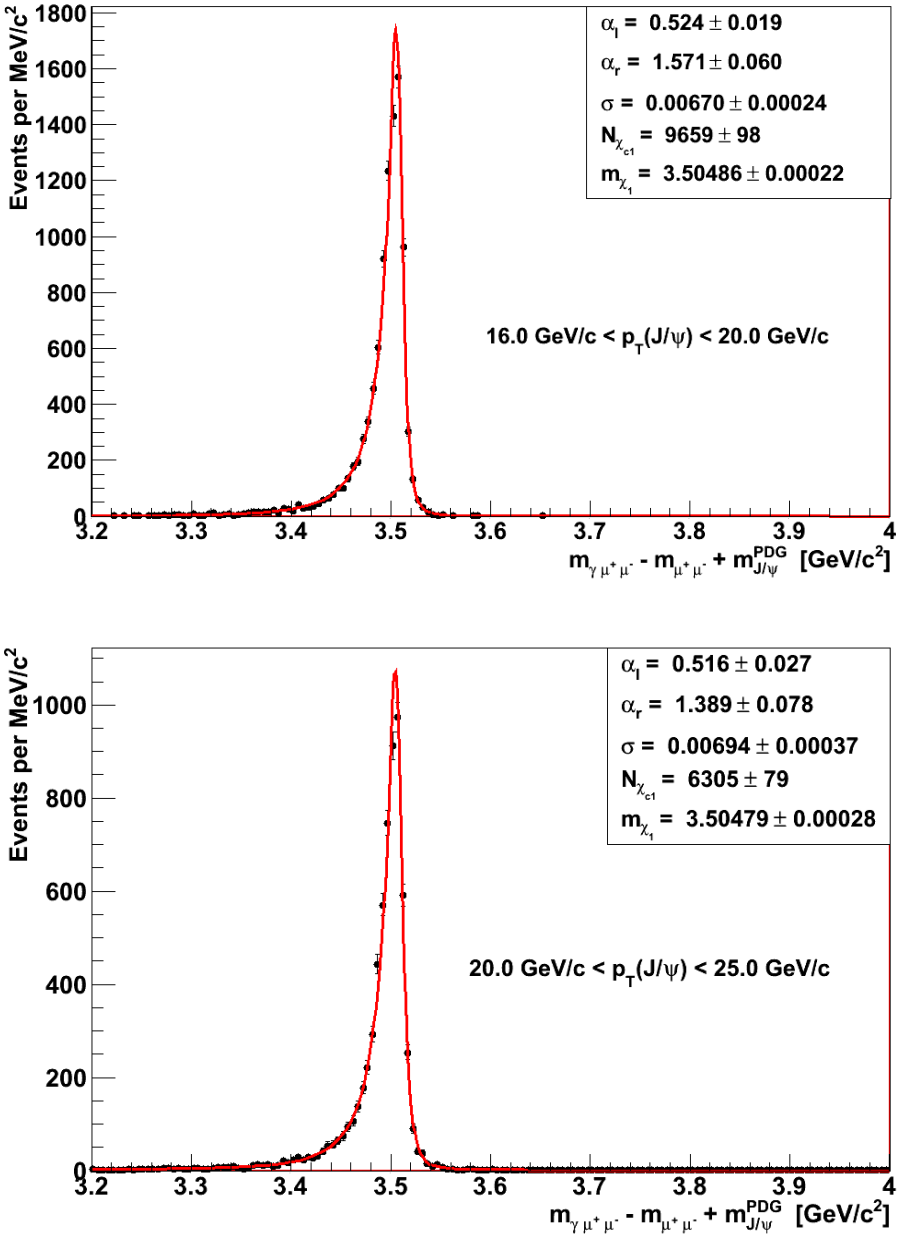

Figure A.3: Double-sided Crystal Ball fits to particle gun Monte Carlo for χ_{c1} candidates for $p_T(J/\psi)$ in [16.0-20.0] GeV/c (top) and [20.0-25.0] GeV/c (bottom).

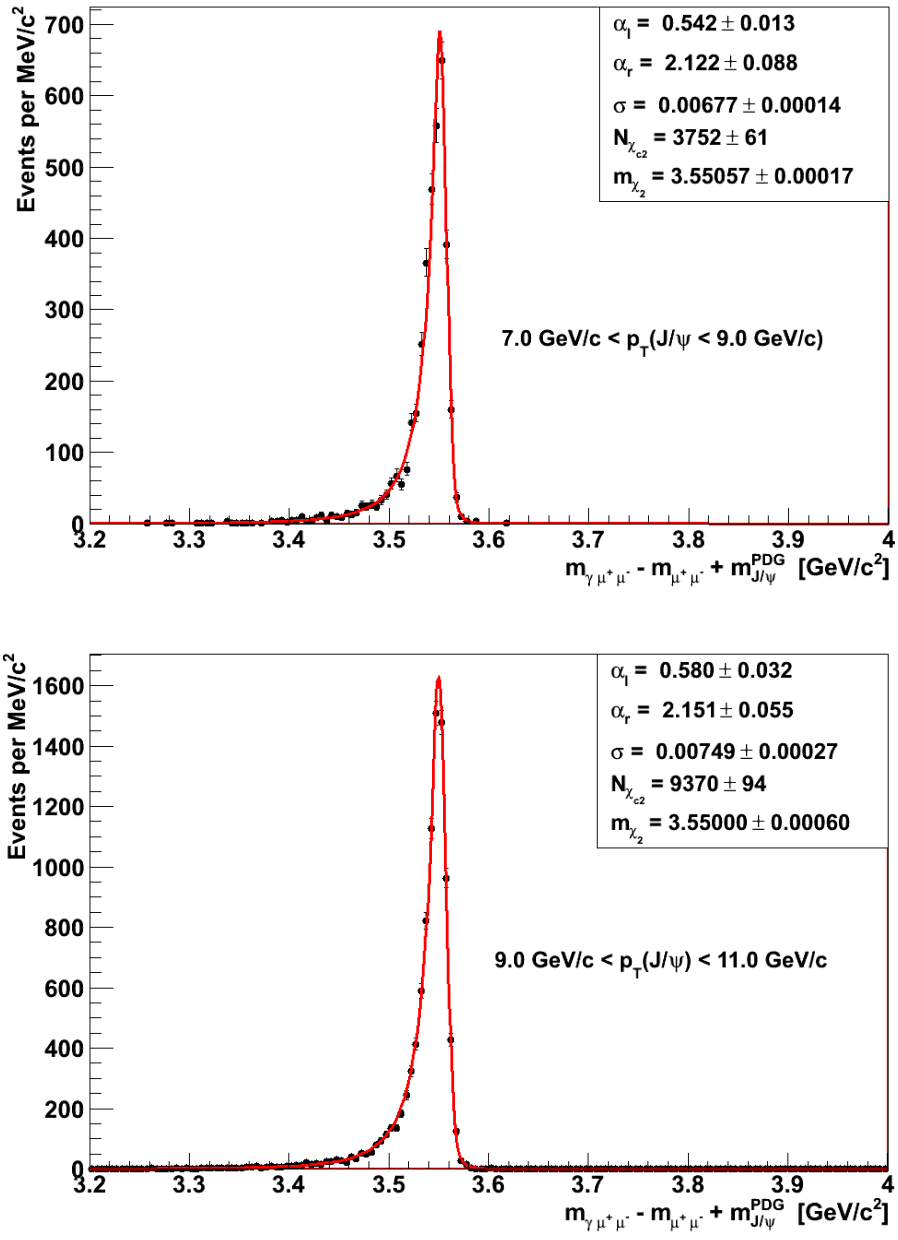

Figure A.4: Double-sided Crystal Ball fits to particle gun Monte Carlo for χ_{c2} candidates for $p_T(J/\psi)$ in [7.0-9.0] GeV/c (top) and [9.0-11.0] GeV/c (bottom).

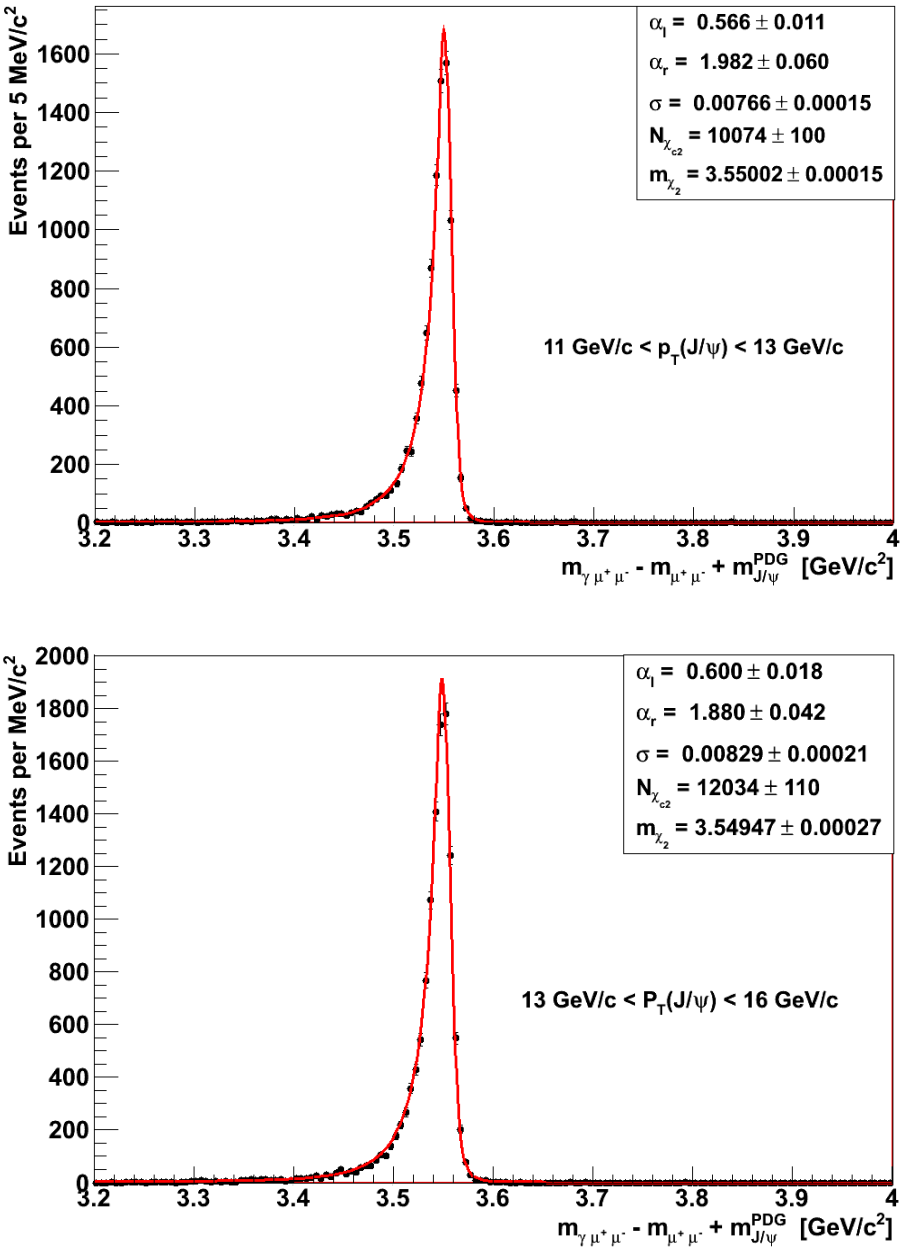

Figure A.5: Double-sided Crystal Ball fits to particle gun Monte Carlo for χ_{c2} candidates for $p_T(J/\psi)$ in [11.0-13.0] GeV/c (top) and [13.0-16.0] GeV/c (bottom).

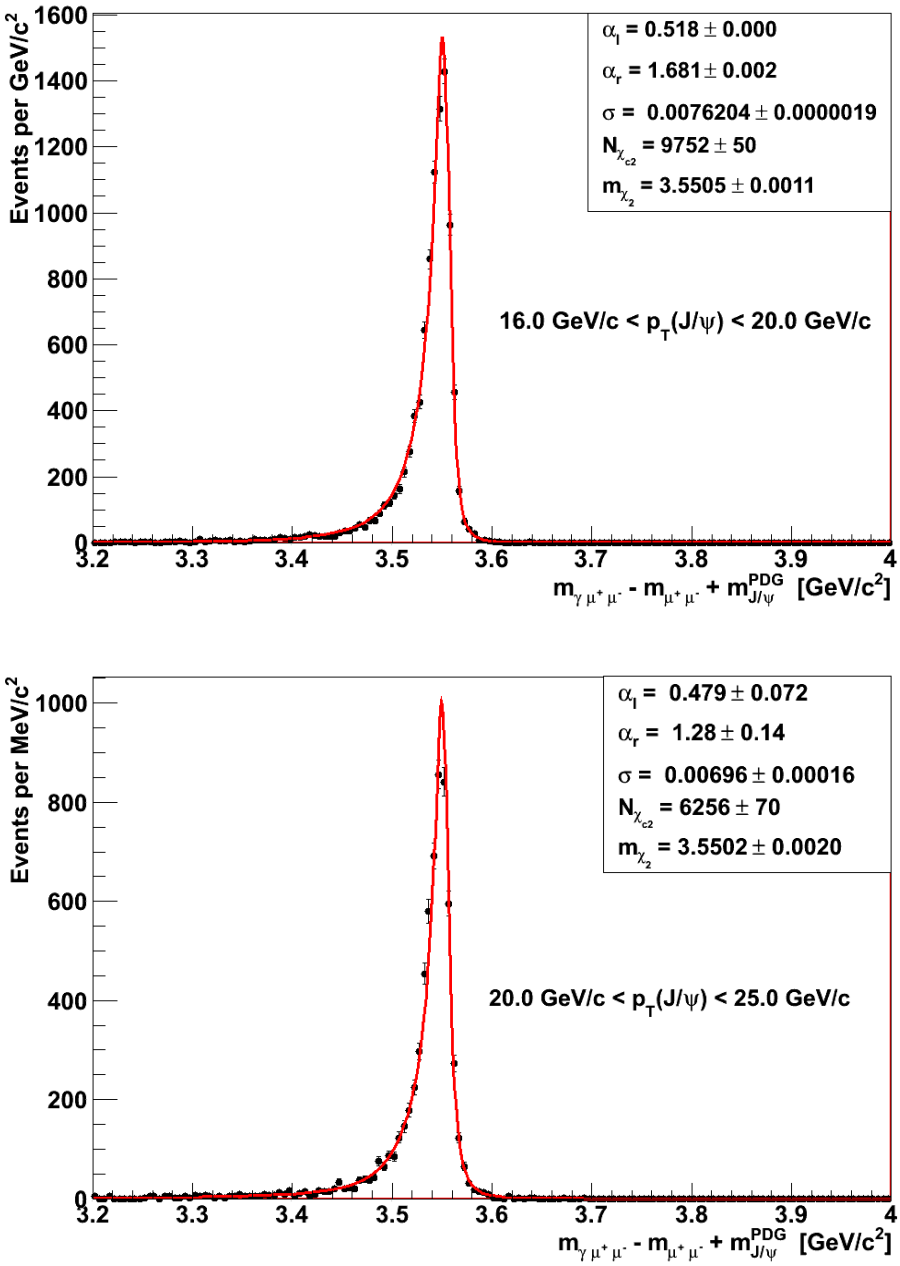

Figure A.6: Double-sided Crystal Ball fits to particle gun Monte Carlo for χ_{c2} candidates for $p_T(J/\psi)$ in [16.0-20.0] GeV/c (top) and [20.0-25.0] GeV/c (bottom).

Appendix B

Uncertainties from the signal model

Different cases in Table D.1 are formulated by varying signal parameters σ, α_l and α_r for χ_{c1} and χ_{c2} within their uncertainties, e:

1 - [2] variation of $\sigma(\chi_{c1})$

3 - [4] variation of $\sigma(\chi_{c2})$

5 - [6] variation of $\alpha_l(\chi_{c1})$

7 - [8] variation of $\alpha_r(\chi_{c1})$

9 - [10] variation of $\alpha_l(\chi_{c2})$

11 - [12] variation of $\alpha_r(\chi_{c2})$

13 - [14] variation of $\sigma(\chi_{c1})$ and $\sigma(\chi_{c2})$

15 - [16] variation of $\alpha_l(\chi_{c1})$ and $\alpha_r(\chi_{c1})$

case	7-9	9-11	11-13	13-16	16-20	20-25
default	0.510±0.049	0.469±0.027	0.451±0.025	0.482±0.027	0.384±0.028	0.368±0.040
1- $\sigma_{\chi_{c1}}$ + e	0.503±0.048	0.466±0.027	0.448±0.025	0.478±0.027	0.378±0.028	0.359±0.039
2- $\sigma_{\chi_{c1}}$ - e	0.517±0.049	0.472±0.027	0.453±0.025	0.486±0.027	0.390±0.029	0.379±0.041
3- $\sigma_{\chi_{c2}}$ +e	0.515±0.049	0.477±0.028	0.454±0.025	0.488±0.027	0.384±0.028	0.372±0.041
4- $\sigma_{\chi_{c2}}$ - e	0.504±0.048	0.461±0.027	0.446±0.025	0.476±0.027	0.384±0.028	0.364±0.042
5- $\alpha_l(\chi_{c1})$ + e	0.514±0.049	0.471±0.027	0.452±0.025	0.484±0.027	0.386±0.029	0.371±0.041
6- $\alpha_l(\chi_{c1})$ - e	0.506±0.048	0.468±0.027	0.449±0.025	0.480±0.027	0.382±0.028	0.366±0.040
7- $\alpha_r(\chi_{c1})$ + e	0.512±0.049	0.471±0.027	0.452±0.025	0.483±0.027	0.387±0.028	0.375±0.041
8- $\alpha_r(\chi_{c1})$ - e	0.508±0.049	0.468±0.027	0.449±0.025	0.480±0.027	0.380±0.028	0.361±0.040
9- $\alpha_l(\chi_{c2})$ + e	0.504±0.048	0.457±0.026	0.446±0.025	0.475±0.027	0.384±0.028	0.342±0.037
10- $\alpha_l(\chi_{c2})$ - e	0.516±0.049	0.483±0.028	0.455±0.025	0.489±0.028	0.384±0.028	0.403±0.044
11- $\alpha_r(\chi_{c2})$ + e	0.509±0.049	0.469±0.027	0.450±0.025	0.481±0.027	0.384±0.028	0.366±0.040
12- $\alpha_r(\chi_{c2})$ - e	0.511±0.049	0.470±0.027	0.451±0.025	0.482±0.027	0.384±0.028	0.371±0.040
13- $\sigma_{\chi_{c1}}$ + e and $\sigma_{\chi_{c2}}$ +e	0.509±0.049	0.474±0.027	0.452±0.025	0.484±0.027	0.378±0.028	0.363±0.040
14- $\sigma_{\chi_{c1}}$ - e and $\sigma_{\chi_{c2}}$ - e	0.511±0.049	0.464±0.027	0.449±0.025	0.480±0.027	0.390±0.029	0.374±0.041
15- $\alpha_l(\chi_{c1})$+e and $\alpha_r(\chi_{c1})$+e	0.516±0.049	0.472±0.027	0.453±0.025	0.485±0.027	0.389±0.029	0.377±0.041
16- $\alpha_l(\chi_{c1})$ - e and $\alpha_r(\chi_{c1})$ - e	0.504±0.048	0.466±0.027	0.448±0.011	0.478±0.027	0.378±0.028	0.359±0.039
diff	- 0.006/+0.007	- 0.014/+0.012	-0.004/+0.005	- 0.007/+0.007	- 0.006/+0.006	- 0.011/+0.026

Table B.1: Ratio of $N_{\chi_{c2}}/N_{\chi_{c1}}$ for different signal parameters varied within their uncertainties..